UNIVERSITÀ
DEGLI STUDI
DI PADOVA

PhD School in Civil and Environmental
Engineering Sciences, University of Padova

THE LATTICE DISCRETE PARTICLE MODEL (LDPM) FOR FRP CONFINED CONCRETE COLUMNS, EXPLORING THE PROPER ORTHOGONAL DECOMPOSITION (POD) TECHNIQUE

Ph.D. Candidate: Chiara Ceccato

Advisor: Prof. Carlo Pellegrino

Co-Advisor: Prof. Gianluca Cusatis

UNIVERSITÀ
DEGLI STUDI
DI PADOVA

Sede Amministrativa: Università degli Studi di Padova

Dipartimento: Ingegneria Civile Edile Ambientale (DICEA)

Scuola di Dottorato: Scienze dell'Ingegneria Civile e Ambientale

Indirizzo: Unico

Ciclo: XXVIII

THE LATTICE DISCRETE PARTICLE MODEL (LDPM) FOR FRP CONFINED CONCRETE COLUMNS, EXPLORING THE PROPER ORTHOGONAL DECOMPOSITION (POD) TECHNIQUE

Direttore della Scuola: Ch.mo Prof. Stefano Lanzoni

Supervisore: Ch.mo Prof. Carlo Pellegrino

Co-Supervisore: Ch.mo Prof. Gianluca Cusatis

Dottorando: Chiara Ceccato

Abstract

Fiber Reinforced Polymers (FRP) have been widely exploited in different civil engineering applications to enhance the performance of concrete structures through flexural, shear or compression strengthening. One of the most common and successful use of FRP sheets can be found in confinement of existing concrete vertical elements which need rehabilitation or increased capacity in terms of strength and ductility. The efficient design of FRP retrofitting requires full understanding of the concrete behavior under the complex triaxial stress state due to the passive confinement mechanisms and, for this reasons, realistic numerical models are commonly sought by the research community. In this study, experimental data gathered from the literature and relevant to the problem of FRP-confined columns subjected to uniaxial compression are simulated by the so called Lattice Discrete Particle Model (LDPM) which was recently developed to simulate concrete materials by modeling the meso-scale interaction of coarse aggregate particles. LDPM has been extensively calibrated and validated with comparison to a large variety to experimental data under both quasi-static and dynamic loading conditions but it has not been fully validated with reference to low confinement compressive stress states, relevant to the targeted application. This task is pursued in the present research. The results show that, with the improvement of the existing LDPM constitutive equations to account for low confinement effects, LDPM is able to predict the concrete material response under FRP-confinement and the developed model can capture the realistic behavior of FRP confined columns with different cross sections.
The present research also deals with the computational aspects of the simulations: the LDPM computational framework is implemented into a multi-purpose structural analysis program called MARS, which is based on an explicit dynamic algorithm scheme, advantageous in terms of convergence. However, decreasing the maximum stable time step with the highest natural frequency of the system, the computational time necessary to carry out simulations of quasi-static events, like the compression tests in the present study, might be highly demanding. In order to decrease the computational cost of the simulations, the Proper Orthogonal Decomposition (POD) as a model reduction technique has been explored for the application to the LDPM models of FRP confined columns and the relationship between efficiency gain and accuracy loss is discussed.

Sommario

I materiali fibrorinforzati a matrice polimerica (FRP) sono utilizzati in svariate applicazioni nel campo dell'ingegneria civile, per migliorare le prestazioni delle strutture in calcestruzzo, dal punto di vista della resistenza a flessione, a taglio, a compressione. Uno degli utilizzi più comuni e apprezzati di questi materiali è legato al confinamento di membrature verticali esistenti, che necessitano di recupero o di un'aumentata resistenza e/o duttilità. La progettazione efficace del rinforzo con FRP richiede piena comprensione del comportamento del calcestruzzo soggetto ai complessi stati tensionali dovuti al confinamento passivo e, per questa ragione, lo sviluppo di un modello numerico realistico è stato ed è tutt'ora uno degli obiettivi principali dei ricercatori. In questa sede, il cosiddetto Lattice Discrete Particle Model (LDPM), recentemente sviluppato per simulare il calcestruzzo attraverso l'interazione degli aggregati a livello di mesoscala, è stato applicato al problema della modellazione di colonne confinate con FRP e sottoposte a compressione, utilizzando come riferimento dati sperimentali di letteratura. LDPM era stato estesamente calibrato e validato sulla base di una larga varietà di condizioni di carico, sia quasi statiche che dinamiche, ma non in relazione a stati tensionali dovuti a compressione con bassi livelli di confinamento, che sono quelli rilevanti nella presente applicazione. Con il miglioramento proposto delle equazioni constitutive in compressione, LDPM è in grado di predire la risposta del calcestruzzo confinato con FRP e il modello sviluppato può simulare realisticamente il comportamento di colonne confinate con differenti sezioni.
La presente ricerca affronta, parallelamente, gli aspetti più computazionali delle simulazioni con LDPM: questo modello è implementato in un software chiamato MARS, che si basa su un algoritmo esplicito, vantaggioso in termini di convergenza. Tuttavia, per ragioni di stabilità, il costo computazionale richiesto per simulare eventi quasi statici, come i test di compressione di questo studio, può risultare molto sconveniente. Per ridurre i tempi di analisi, la tecnica della Proper Orthogonal Decomposition (POD) è stata esplorata in relazione all'applicazione di LDPM al caso delle colonne confinate con FRP sottoposte a compressione, valutando il rapporto tra guadagno computazionale e accuratezza dei risultati.

Acknowledgments

I would like to extend my sincere thanks to the many people who generously contributed to the work presented in my Ph.D Thesis.

The first mention goes to my supervisor, Prof. Carlo Pellegrino not only for his academic support but also for the unique opportunities he gave me during the past 3 years. I express profound gratitude to my co-advisor, Prof. Gianluca Cusatis, whose research group I joined at Northwestern University, Evanston (IL). He has been providing me guidance and motivation, with insightful discussions, patience and bright ideas. I have learned a lot from him and without his help I could not have finished my dissertation successfully.

Special thanks are also given to Dr. Daniele Pelessone, chief scientist at ES3 - Engineering and Software system Solutions, for the wonderful internship experience in his company and to Dr. Xinwei Zhou, for his continuous computational support.

I would like to acknowledge Prof. Massimiliano Ferronato, for his availability and his help with my numerical issues. I have also deeply appreciated the advice of Prof. Marco Salviato, who I was lucky enough to meet during my time at Northwestern University. Together with his wife, Dr. Rossella Rosa, they offered me not only scientific guidance, but also their beautiful and precious friendship. A special mention goes to Dr. Erol Lale, for sharing with me his knowledge, his opinions and his time.

Anyway, none of this would have been possible without the closeness and carefulness of people I love.

Contents

List of Tables

List of Figures

Introduction

General Background

During the last decades, many existing reinforced concrete (RC) constructions have needed intervention for structural enhancement, due to deterioration and durability issues, with consequent decrease in performance. Furthermore, the need of strength and ductility upgrade appears to be crucial for structural members under bending, shear and compression loads in terms of seismic design, assessment and retrofitting. Under these circumstances, fiber reinforced polymers (FRP) composites have proven to be an effective strengthening and repair technique which has gained increasing popularity thanks to the material excellent mechanical properties, high strength-to-weight ratio and corrosion resistance.
FRPs can be described as composite, anisotropic materials made of a polymer matrix reinforced with fibers in a preferred direction. The fibers - made of carbon, glass or aramid- supply for stiffness and strength, while the matrix - generally epoxy resin - properly bonds and envelopes the fibers protecting them from cuts and notches and allowing force transfer.
Their application in civil engineering is diffused in the renewal of buildings, bridges and other infrastructures, for example for shear strengthening and flexural strengthening of beams or slabs in needs of rehabilitation, where the direction of the fibers will be parallel to the stirrups, in case of shear, and to the longitudinal bars in case of bending.
One of the most common and successful use of FRP, though, can be found in the jacketing of existing RC vertical elements, where the composite material can work by restraining the lateral expansion of concrete in order to increase the ultimate strength and the ductility of the structural members, in particular when highest performances or seismic assessment works are required.
Externally bonded FRP sheets, with fibers in the hoop direction, are wrapped around bridge piers or column building, in order to provide for lack of transverse reinforcement, material degradation or performance deficiency. The FRP jacket can be formed by rolling from a prefabricated flat sheet or, more often, in a wet layup process, with a manual procedure. In this last case, a layer of polymeric primer is firstly applied to the concrete external surfaces, after being sanded and cleaned, in

(a) Layup process for the application of FRP sheets around columns

(b) Compression Test set-up for FRP-confined column

Figure 1: FRP-confined columns

order to fill air voids and provide high bond strength; then a layer of epoxy saturant is applied followed by a single ply fiber sheet and another layer of saturant. A plastic roller is generally used to remove the trapped air and allow a better impregnation. This procedure is repeated for every FRP layer.
Several studies have focused on fully understanding the behavior of FRP-confined concrete. In fact, in practical applications, the design of FRP jackets can be reliable only if the stress-strain relationship of FRP confined concrete is understood and correctly modeled [1]. The classical stress-strain model developed by Mander and coworkers in 1988 [2] for confined concrete has proved to be inappropriate because a constant confining pressure is assumed. While in the case of steel-confined concrete, this assumption is correct (after the yielding of the steel, the confining pressure provided is almost equivalent to the yield strength of the material), this is no longer true for FRP-confined concrete. In this case, the confining pressure provided by the external jacket increases continuously with the lateral strains of concrete, which in turn depend on the axial strains -being the composite material linear elastic till collapse.

Literature reviews show that, on one hand, several axial compression tests have been performed on concrete cylinders confined by FRP jackets and, on the other hand, diverse models have been formulated, aiming to predict the stress-strain response and the failure mechanisms during the loading history.

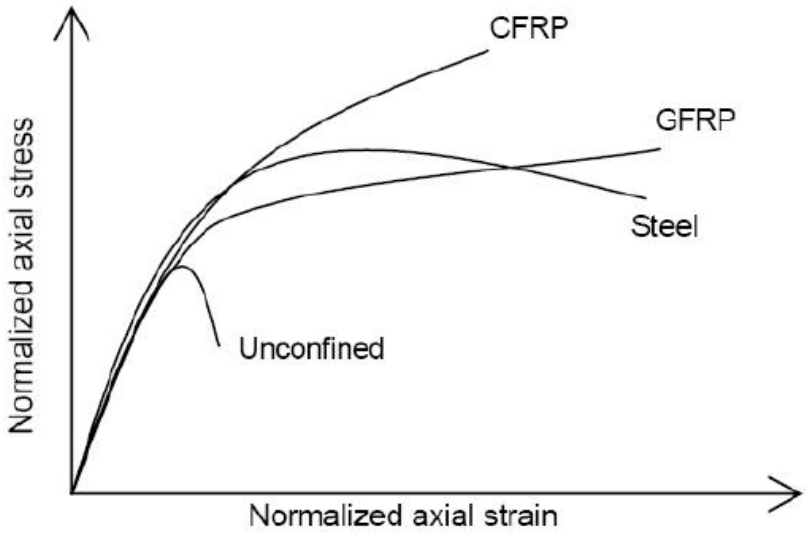

Figure 2: Axial stress - Axial strain responses for unconfined and confined concrete

Various analytical models have been proposed in terms of a stress-strain relationship, mostly for cylindrical columns characterized by uniformly-confined concrete [1], including design-oriented model, [3, 4, 5], in form of closed expressions deduced from test data on FRP-confined concrete specimens, and analysis-oriented models [6, 7, 8], in form of an incremental iterative formulation explicitly accounting for the concrete core-FRP interaction. The behavior of non uniformly confined concrete, typical of square and rectangular sections, can also be approximately taken into account [9, 10, 11] through aspect ratio factors or by later modifications of the original formulations, but the stress variations are complex to be captured and understood over the section [12]. In addiction, the finite element method has been used for advanced numerical models in order to capture the interaction mechanisms between FRP and concrete in further details. FEM simulations need a solid constitutive model for concrete, in order for the results to be accurate and many different formulations have been proposed to this scope. Several 3D FE implementations use plasticity models, mostly based on Drucker Prager Plasticity formulations, with different definitions of yield criterion, hardening rule, flow rule to take confinement effects into account (e.g. [13], [14], [15], [16]). Amongst them, the method developed by Yu et al. [12] makes use of a hardening/softening rule which is assumed to depend on the confining pressure and of a confinement-dependent non-associated flow rule. Other 3D formulations are based on plastic-damage models [17], to simulate reductions in elastic stiffness of concrete and capture non-uniformly stresses

and, more recently, on the microplane model [18], considered capable of realistically simulating behavior of concrete under dominant tension, compression and complex non-proportional loading histories elastic damage models. Simplified 1D models have also been proposed as quick numerical tools to simulate cycling loading, using for instance elastic-damage models [19] and using fibers models allowing non linearly distributed inelasticity [20].
Some models also include the steel stirrups and the longitudinal bars in the columns and the interaction with FRP is studied. One of the latest has been developed by J.G. Teng and coworkers in 2015 [21], where a 3D finite element approach for circular concrete has been presented, based on a plastic-damage model for concrete and where the confinement mechanisms of steel bar-confined RC columns is examined.
In general, however, while the mechanisms governing the behavior of uniformly confined concrete as in FRP confined circular concrete columns are well understood, the behavior of concrete columns under non-uniform confinement, such as FRP confined columns with non circular cross section, needs further investigation[22].

Research Significance and Objectives

Most of these FE macroscopic models present limitations due to the simplifications in the constitutive laws for the concrete softening response and often the good agreement between experimental data and numerical models are not general but oriented to specific applications and derived from limited empirical evidences, as often highlighted [12, 17, 18]. An interesting summary of the challenges faced by the research community on the development of a realistic constitutive relation for concrete, especially if subjected to complex stress states such the ones experienced with FRP confinement, is given by Yu-Fei Wu [23]: Wu highlights the lack of a general constitutive relationship or stress-strain model for concrete and, consequently, to overcome this difficulty, a large number of empirical models have been developed for different applications. Most of these models, though, are very local in their applicability, being mostly at the macroscopic scale and phenomenologically based. On the contrary, as Wu writes, mesoscale and miscroscale models can be able to describe the interaction between concrete particles or molecules and, so, can potentially provide a global solution. For instance, the precise and accurate material dilatation properties during the microcracking evolution and fracture propagation turned out to be crucial for capturing the post-peak response of FRP confined concrete [3]. The confining action of FRP jackets, in fact, develops progressively during the vertical member compression process, increasing gradually and continuously in response the lateral strain of concrete, which is, in turn, dependent on the axial strain. The mechanisms activated during the fracturing process of the material are complex and not easy to be captured in a simplified macroscopic model: for these reasons, a recently developed meso-scale model for concrete, called the Lattice Discrete Particle Model

(LDPM) developed by Cusatis and coworkers [24] has been explored with relation to the FRP confinement response. LDPM, modeling concrete materials through the meso-scale interaction of coarse aggregate particles, has been extensively calibrated and validated with comparison to a large variety to experimental data under both quasi-static and dynamic loading conditions and its unique capability of predicting stress-strain curve and failure modes for concrete and other quasi brittle material is due to the simulation of compressive failure through tensile and shearing softening at the meso-scale, without postulating the existence of softening in compression [25, 26, 27, 28, 29]. LDPM, though, has not been fully validated with reference to low confinement compressive stress states relevant to the targeted application and this is the first aim of the present research, mainly focused on the development of a general model able to describe the behavior of FRP confined concrete.
The LDPM computational framework is implemented into the MARS code [30], which is a multi-purpose structural analysis program based on a object-oriented architecture. MARS performs structural analysis by an explicit dynamic algorithm based on a central difference scheme and is very effective in the management of the various computational entities (nodes, finite elements, loads, etc.) making possible the numerical simulation of very large systems. In addition, the explicit character of the computational scheme implemented in MARS makes it advantageous because is not affected by the convergence problems that implicit schemes often have in handling softening behavior. Explicit algorithms, however, are not unconditionally stable and require an accurate evaluation of the numerical stability of the numerical simulations. Decreasing the maximum time step with the highest natural frequency of the computational system, a prohibitive number of increments may be required for problems governed by low frequencies and, consequently, application of explicit dynamics to quasi-static events, like the ones related to the present study, may become critical in terms of time analysis. The computational time necessary to carry out the simulations performed in this effort, in fact, turned out to be significantly demanding. As highlighted by de Frias et al. (2014) [31], though, time steps much larger than the critical one would be sufficient to accurately describe the low-dynamic overall response and, in literature, different solutions have been investigated to artificially increase the speed of the process in simulations (see, amongst others [32, 33, 34]). Mass scaling techniques, for instance, have been developed to increase the time step size by adjusting the mass of the most critical elements; significant errors, though, can originate if those elements where the mass scaling is applied have a significant contribution to the global system response. Another interesting and promising approach can be found in the Proper Orthogonal Decomposition as a Model Reduction technique, which has now found applications in different fields of engineering and physics (e.g.[35, 36, 37, 38, 39]). Dynamic systems can be projected onto subspaces containing the solution of the problem or a good approximation, so that a high-dimensional process is converted into a low-dimensional description of

it [40].

First of all, POD allows to achieve good results with a reduced number of operations, feature which is particularly profitable for implicit methods; furthermore, the stable time step for the simulation is likely to increase. In fact, the natural frequencies of the complete computational system are reasonably higher than the natural frequencies of the projected computational system, capturing only the dominant components of the response with a limited number of modes.
These considerations bring to the second aim of this research, which is to investigate if and how the Proper Orthogonal Decomposition can be efficiently applied to explicit methods, in particular for LDPM quasi-static dynamics systems. Focusing both on the *a posteriori* data reconstruction for validation purposes and on its possible prediction capability, this technique has been considered in relation to the current simulations.

Outline of the thesis

The present effort aims to study the response of FRP confined columns subjected to compressive loading with the Lattice Discrete Particle Model (LDPM), in order to explore its capabilities of simulating and capturing the behavior of concrete under complex loading conditions and, in particular, to use it as a more general constitutive relationship of concrete for applications in FRP confined concrete members.
The second objective has been to investigate the potential of the Proper Orthogonal Decomposition (POD) as a model reduction technique, taken in consideration to reduce the overall computational cost of LDPM simulations and hence making it practical for engineering applications.

In Chapter 1 the material models are described- in particular an overview of the Lattice Discrete Particle Model (LDPM) for concrete is presented, going through its geometry, kinematics, equilibrium and constitutive equations; also an overview of the Spectral Stiffness Microplane Model for composite laminates is given.

In Chapter 2 the proposed modification for the micro-scale constitutive law in compression is described in details - the new formulation was required in order to capture the behavior of concrete under low confinement pressures (up to 20 MPa), usually experienced by FRP-confined concrete;

In Chapter 3 the application of the numerical model for FRP confined concrete columns is shown in relation to an experimental campaign carried out by Wang and Wu (2007) [41] and results are discussed highlighting strengths and limitation of the proposed model;

In Chapter 4 the Proper Orthogonal Decomposition (POD) technique is introduced and applied to the dynamic equations of motions. Applications to 1D and 2D benchmark cases are carried out and finally POD has been applied to LDPM simulations; some tension and compression tests have been carried out and finally POD algotithm has been applied to the circular FRP confined concrete column.

In Chapter 5 the overall conclusions of this works are summarized and the goals of future research are set.

Chapter 1

Material Models for Concrete and FRP

1.1 The Lattice Discrete Particle Model (LDPM) for concrete and quasi-brittle materials

The Lattice Discrete Particle Model (LDPM) has been developed by Cusatis et coworkers ([24, 25]) in order to simulates concrete and quasi brittle-material mesostructure, by taking into account the mechanical interaction of the coarser aggregate particles. LDPM has been extensively calibrated and validated with comparison to a large variety to experimental data under both quasi-static and dynamic loading conditions: its unique capability of predicting stress-strain curve and failure modes for concrete and other quasi brittle material is due to the simulation of compressive failure through tensile and shearing softening at the meso-scale, without postulating the existence of softening in compression.

1.1.1 Geometrical characterization of the mesostructure

As accurately described in [24], the procedure defining the concrete mesostructure is based on the definition of the number and size of the aggregates pieces, their position, their interconnections and also the surfaces through which forces are transmitted between them. The following steps illustrate how the material internal structure is built:

1. The coarse aggregate pieces (particles), assumed to be spherical, are introduced into the concrete volume by a try-and-reject random procedure. The number and dimension of particles to be placed inside the specimen volume $V$are determined from a set of mix-design parameters, i.e. cement content c, water-to-cement ratio w/c, aggregate-to-cement ratio a/c, maximum ag-

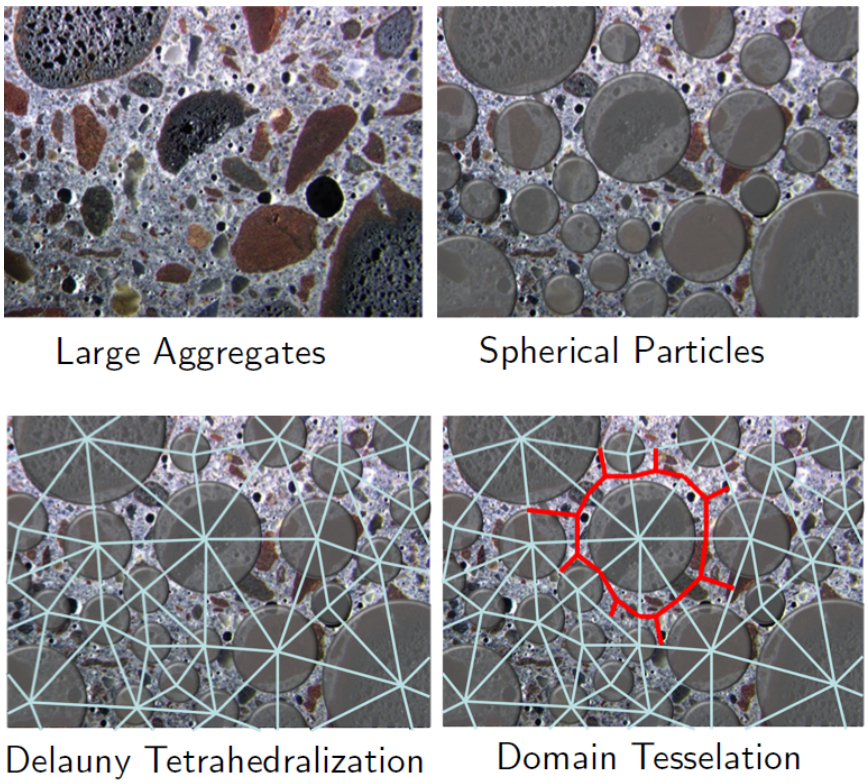

Figure 1.1: LDPM geometry in 2D

gregate size d_a, minimum aggregate size d_0 (governing the model resolution), Fuller coefficient f, to be given as input. The aggregate volume fraction is then computed and a consistent granulometric distribution of particles size, spanning from d_a to d_0, randomly generated according to the Fuller curve.

2. Over the external surfaces, zero-radius aggregate pieces (nodes) are distributed so that the surface discretization resolution is comparable to the one inside the specimen, firstly placing the vertex nodes, then the edge and surface nodes. The particles are finally located inside the specimen in order to create a statistically isotropic random mesostructure, using the procedure described in (vedi citazioni). The straight lines connecting the particle centers define the lattice system.

3. A three-dimensional domain tessellation, based on the Delaunay tetrahedralization of the generated aggregate centers, creates a system of cells interacting through triangular facets, which can be represented, in a two-dimensional setting, by straight line segments as shown in Figure. The tessellation of a tetrahedron, whose vertices particles govern the mechanical interactions, is shown

in figure 1.2: in general, it can be obtained by a set of triangles, defined by a point on the tetrahedron edge (edge-points), a point on the tetrahedron face (face-points) and a point inside the tetrahedron (tet-point). A polyhedral cell containing the particle is created by the collection of facets associated with each particle. The definition of the these surfaces where the interaction forces are exchanged, corresponds to damage localization zones, consistently with the fracture initiating and propagating in the mortar paste.

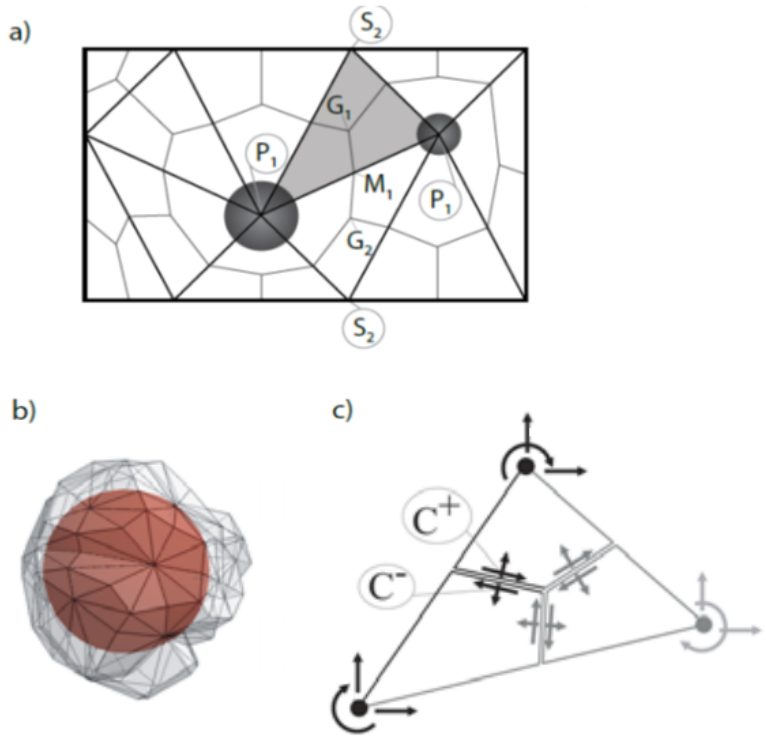

Figure 1.2: a) Mesostructure tessellation b) Three dimensional discrete cells c) Definition of nodal degrees of freedom and contact facets in two-dimensions.

1.1.2 Compatibility and Equilibrium: governing equations

The governing equations are derived from the basic unit of the model, which is the four-particle tetrahedron shown in Fig.1.3a, to be subdivided into four subdomains, each associated to one particle, the portion of the three tetrahedron edged attached to the node and the six triangular tessellation facets attached to those edges (Fig.1.3b). Then, the displacement field is defined according to the rigid-body kinematics for every subdomain:

$$\boldsymbol{u}(\boldsymbol{x}) = \boldsymbol{u_i} + \boldsymbol{\theta_i} \times (\boldsymbol{x} - \boldsymbol{x_i}) \tag{1.1}$$

where $\boldsymbol{x} = [x_1, x_2, x_3]^T \in V_i$, $\boldsymbol{x_i}$ defines the node i position, $\boldsymbol{u_i}$ its translational degrees of freedom and $\boldsymbol{\theta_i}$ its rotational degrees of freedom.
Consequently, a displacement jump can be defined at the centroid C of each tetrahedron facet

$$[\![\boldsymbol{u}_{Ck}]\!] = \boldsymbol{u}_{Cj} - \boldsymbol{u}_{Ci} \tag{1.2}$$

where i and j are nodes adjacent to the k facet and $\boldsymbol{u}_{Cj} = \boldsymbol{u}(\boldsymbol{x}^+_{Ck})$, $\boldsymbol{x}^+_{Ck} \in V_j$ and $\boldsymbol{u}_{Ci} = \boldsymbol{u}(\boldsymbol{x}^-_{Ck})$, $\boldsymbol{x}^-_{Ck} \in V_i$. The facet strain vector can be defined as the displacement jump at the contact point divided by the inter-particle distance $[\![\boldsymbol{u}_{Ck}]\!]/\ell_e$. The strain vector $[\![\boldsymbol{u}_{Ck}]\!]/\ell_e$ is decomposed into its normal ans shear components: the projections are used instead of the facets themselves for the decomposition, in order to ensure that the shear interaction between adjacent particles does not depend on the shear orientation. The components of the strain vector in a local system of reference in the plane of the projected facets, characterized by the unit vectors n, l, and m, are the normal and shear strains. Through their definition, the discrete compatibility equations for the LDPM formulation are given:

$$\varepsilon_{Nk} = \frac{\boldsymbol{n}_k^T[\![\boldsymbol{u}_{Ck}]\!]}{\ell_e}; \qquad \varepsilon_{Mk} = \frac{\boldsymbol{m}_k^T[\![\boldsymbol{u}_{Ck}]\!]}{\ell_e}; \qquad \varepsilon_{Lk} = \frac{\boldsymbol{l}_k^T[\![\boldsymbol{u}_{Ck}]\!]}{\ell_e}. \tag{1.3}$$

The corresponding normal and shear stress are calculated through the meso-scale constitutive laws. In general, $\boldsymbol{\sigma}_k = \boldsymbol{F}(\boldsymbol{\varepsilon}_k, \boldsymbol{\zeta}_k)$, where $\boldsymbol{\sigma}_k$, $\boldsymbol{\varepsilon}_k$, $\boldsymbol{\zeta}_k$ collect the facet stresses, the facet strains and internal variable respectively.
The equilibrium is finally imposed through the Principle of Virtual Works (PVW). The internal work associated with a generic facet is expressed as

$$\delta W_k = \ell_e A_k \boldsymbol{\sigma_k^T} \delta \boldsymbol{\varepsilon_k} = \ell_e A_k (\sigma_N k \delta \varepsilon_{Nk} + \sigma_M k \delta \varepsilon_{Mk} + \sigma_L k \delta \varepsilon_{Lk}) \tag{1.4}$$

where A_k is the projected facet area. Replacing the strain components definition (Eq.1.3) the nodal forces at node i and j associated with facet k. Summing up the contributions of all the facets and equating the total internal work with the total external work, the discrete equilibrium equations of the LDPM formulation can be obtained. It can be shown that the equilibrium equations obtained through the PVW correspond exactly to the translational and rotational equilibrium of each polyhedral LDPM cell.

1.1.3 Analogies between LDPM and Microplane Models

LDPM can be interpreted as a discrete version of the Microplane Models, firstly introduced by Bažant and Oh in 1984 ([42]). In fact, as explicitly stated in [43], the constitutive relations defined on the microplanes, lumped into a single material point in the microplane models, can also be used in an explicitly mesoscale model on planes of various orientations separating the neighboring aggregates embedded in

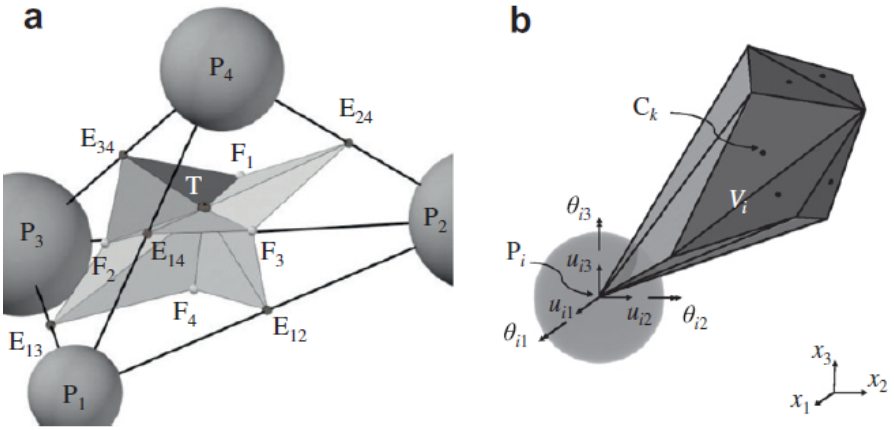

Figure 1.3: a) tessellation of a LDPM tetrahedron connecting four particles b) Portion of a tetrahedron associated to one particle.

a cement mortar matrix, which are the LDPM facets. The microplanes models have been introduced to simulate softening damage in quasi-brittle materials as concrete and rocks and they can in fact capture the inelastic phenomena characterizing the concrete microstructure.
The constitutive relations characterizing the microstructural behavior are formulated not with a traditional tensorial constitutive model of the macroscopic continuum but in terms of the stress vector and strain vectors acting on planes of all possible orientations at a given point of the continuum (microplanes) [44]; the microplane vectors are then related to the continuum tensors through a variation principle.
Accoriding to [42] and [43], the strain vector on the microplane $\boldsymbol{\varepsilon}_N$ is the projection of $\boldsymbol{\varepsilon}$: $\varepsilon_{N_i} = \varepsilon_{ij} n_j$, being n_i, $i = 1, 2, 3$ the components of the unit normal vector $\boldsymbol{n}$ of the microplane in global cartesian coordinates. The orthogonal unit coordinate vectors laying within the microplane are $\boldsymbol{l}$ and $\boldsymbol{m}$. Projecting the strain vector, one can define the normal and shear components:

$$\varepsilon_N = N_{ij}\varepsilon ij, \quad \varepsilon_L = L_{ij}\varepsilon ij, \quad \varepsilon_M = M_{ij}\varepsilon ij; (\quad \varepsilon_T = \sqrt{\varepsilon_L^2 + \varepsilon_{M_)}^2} \tag{1.5}$$

where

$$N_{ij} = n_i n_j \quad L_{ij} = (l_i n_j + l_j n_i)/2; \quad M_{ij} = (m_i n_j + m_j n_i)/2 \tag{1.6}$$

The deviatoric and volumetric strain are also defined:

$$\varepsilon_D = \varepsilon_N - \varepsilon_V, \quad \varepsilon_V = \varepsilon_{kk}/3 \tag{1.7}$$

The static equivalence between stress vectors on all the microplanes and the stress tensor is superimposed through the principle of virtual works:

$$\frac{2\pi}{3}\sigma_{ij}\delta\varepsilon_{ij} = \int_{\Omega}(\sigma_N\delta\varepsilon_N + \sigma_L\delta\varepsilon_L + \sigma_M\delta\varepsilon_M)d\Omega \tag{1.8}$$

where Ω is the surface of a unit hemisphere centered at the material point and $\frac{2\pi}{3}$ its volume. The virtual work of continuum stresses within a unit sphere must be equal to the virtual work of the microplane stress components. The following basic equilibrium equation can be written, combining eq.(1.5) and eq. (1.8) and considering that it mush hold for any virtual work:

$$\sigma_{ij} = \frac{3}{2\pi} = \int_{\Omega}(\sigma_N N_{ij} + \sigma_L L_{ij} + \sigma_M M_{ij})d\Omega \tag{1.9}$$

1.1.4 Constitutive laws

Elastic Behavior

As described in details in [24], the elastic behavior for LDPM is formulated assuming that stresses and corresponding strains are proportional to each other:

$$\sigma_N = E_N\varepsilon_N; \quad \sigma_M = E_T\varepsilon_L; \quad \sigma_L = E_T\varepsilon_L; \tag{1.10}$$

where $E_N = E_0$ (E_0: effective normal modulus), $E_T = \alpha E_0$ (α shear-normal coupling parameter). E_0 and α are considered as elastic material properties to be identified from experimental tests. The relationship between the meso-scale LDPM parameters, α and $\mathbf{E}_0$ and the traditional macroscopic parameters E (Young Modulus) and ν (Poisson ratio) can be obtained considering an infinite number of facets surrounding the aggregate piece (see for example Bažant and Pratt [45], Carol and Bažant [46]):

$$E_0 = \frac{1}{1-2\nu}E \Leftrightarrow E = \frac{2+3\alpha}{4+\alpha}E_0 \tag{1.11}$$

and

$$\alpha = \frac{1-4\nu}{1+\nu} \Leftrightarrow \nu = \frac{1-\nu}{4+\nu} \tag{1.12}$$

According to Cusatis et al. [24], Eqs. (1.11) and (1.12) and (16) can be confidently used to estimate the LDPM elastic parameters from macroscopic experimental measurements of Young's modulus and Poisson's ratio.
Negative values of α and, consequently, of shear stiffness are associated with $\nu > 0.25$, so the entire range of thermodynamically acceptable Poissons ratios are not covered but this limitation doesn't affect concrete modeling, being its Poisson's ratio less or equal to 0.2.

Fracturing Behavior

The fracturing behavior, characterized by tensile normal strains $\varepsilon_N > 0$, can be formulated with a relationship between the effective strain ($\sigma = \sqrt{\sigma_N^2 + (\sigma_L^2 + \sigma_M^2)/\alpha}$) and the effective stress ($\varepsilon = \sqrt{\varepsilon_N^2 + \alpha(\varepsilon_L^2 + \varepsilon_M^2)}$). The effective stress is assumed to be incrementally elastic $\dot{\sigma} = E_0\dot{\varepsilon}$ and its values can span from 0 to a limit strain dependent boundary $\sigma_{bt}(\varepsilon, \omega)$ where

$$\sigma_{bt}(\varepsilon, \omega) = \sigma_0(\omega) exp\left[-H_0(\omega)\frac{\langle \varepsilon_{max} - \varepsilon_0\omega \rangle}{\sigma_0(\omega)}\right] \tag{1.13}$$

The variable ω represents the degree of interaction between shear and normal stress: $\tan\omega = \dfrac{\varepsilon_N}{\sqrt{\alpha}\varepsilon_T} = \dfrac{\sigma_N\sqrt{\alpha}}{\sigma_T}$ (where ε_T in the total shear strain and σ_T the total shear stress).
The function $\sigma_0(\omega)$, strenght limit for the effective stress, it is defined as:

$$\sigma_0(\omega) = \sigma_t \frac{-\sin\omega + \sqrt{\sin^2\omega + 4\alpha\cos^2\omega(\sigma_t^2/\sigma_s^2)}}{2\alpha\cos^2\omega(\sigma_t^2/\sigma_s^2)} \tag{1.14}$$

being σ_t the tensile stress and σ_s the shear stress.
When the maximum elastic strain reaches the elastic limit, the boundary σ_{bt} starts to decay. The softening modulus, governing the decay rate, is defined as:

$$H_0(\omega) = H_t\left(\frac{2\omega}{\pi}\right)^{n_t} = \frac{2E_0}{\ell_t/\ell - 1}\left(\frac{2\omega}{\pi}\right)^{n_t} \tag{1.15}$$

where $\ell_t = 2E_0G_t/\sigma_t^2$, G_t is the meso-scale fracture energy and ℓ is the length of the tetrahedron edge associated with the current facet. For further details, one can see [24].

Compressive Behavior

LDPM constitutive law is compression, in order to simulate pore collapse and material compaction, is based on a strain-dependent normal boundary σ_{bc} limiting the compressive normal stress component at the facet level. It is assumed to be a function of the volumetric strain $\varepsilon_V = (V - V_0)/V_0$, being V and V_0 the current and initial volume of the tetrahedron, and deviatoric strain $\varepsilon_D = \varepsilon_N - \varepsilon_D$, $\sigma_{bc}(\varepsilon_D, \varepsilon_V)$.
For a constant deviatoric-to-volumetirc strain ratio $r_{DV} = \varepsilon_D/\varepsilon_V$, the compressive boundary can be written:

$$\sigma_{bc}(\varepsilon_D, \varepsilon_V) = \begin{cases} \sigma_{c0}, & \text{for } -\varepsilon_{DV} \leq 0 \\ \sigma_{c0} + \langle -\varepsilon_{DV} - \varepsilon_{c0} \rangle H_c(r_{DV}), & \text{for } 0 \leq -\varepsilon_{DV} \leq \varepsilon_{c1} \\ \sigma_{c1}(r_{DV})\mathsf{exp}[(-\varepsilon_{DV} - \varepsilon_{c1})H_c(r_{DV})/\sigma_{c1}(r_{DV})], & \text{otherwise} \end{cases} \tag{1.16}$$

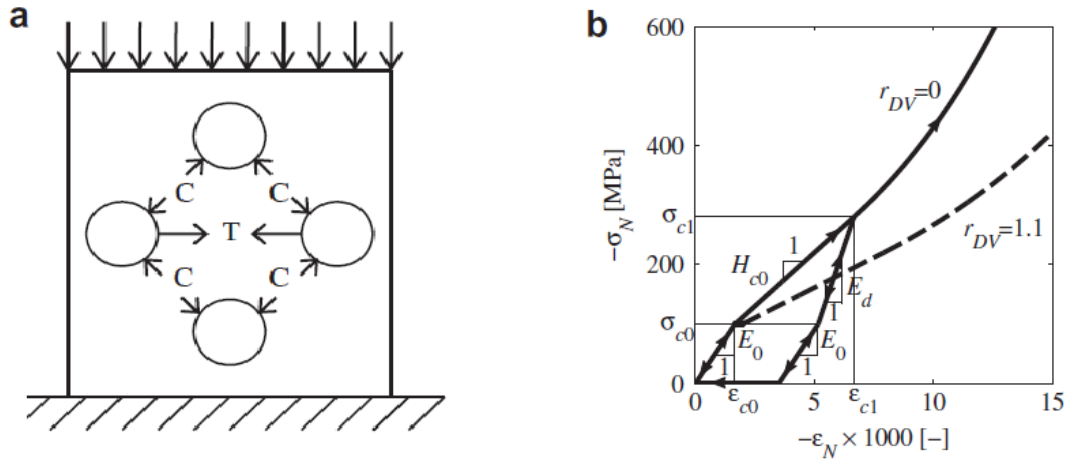

Figure 1.4: a) Idealized effect of compression on heterogeneous materials. b) Typical normal stress versus normal strain curves in compression.

where $\varepsilon_{DV} = \varepsilon_V + \beta\varepsilon_D$ (β is a material parameter), $\varepsilon_{c0} = \sigma_{c0}/E_0$ is the compaction strain at the beginning of the pore collapse, $H_c(r_{DV})$ the initial hardening modulus, $\varepsilon_{c1} = \kappa_{c0}\varepsilon_{c0}$ the compaction strain at which rehardening begins, κ_{c0} the material parameter governing the rehardening and $\sigma_{c1}(r_{DV}) = \sigma_{c0} + (\varepsilon_{c1} - \varepsilon_{c0})H_c(r_{DV})$.

The slope of the initial hardening modulus tends to zero for increasing values of r_{DV} and this feature is achieved setting:

$$H_c(r_{DV}) = \frac{H_{c0}}{1 + \kappa_{c2}\langle r_{DV} - \kappa_{c1}\rangle} \tag{1.17}$$

where H_{c0} κ_{c1} κ_{c2} are assumed to be material parameters. For further details, one can see [24].

Frictional Behavior

In case of compression, the shear strenght of concrete increases because of frictional effects. They have been simulated through incremental plasticity: incremental stresses are defined as $\dot{\sigma_M} = E_T(\dot{\varepsilon_M} - \dot{\varepsilon_M^p})$ $\dot{\sigma_L} = E_T(\dot{\varepsilon_L} - \dot{\varepsilon_L^p})$. The plastic potential can be expressed as $\varphi = \sqrt{\varepsilon_M^2 + \varepsilon_L^2} - \sigma_{bs}(\sigma_N)$, where

$$\sigma_{bs} = \sigma_s + (\mu_0 - \mu_\infty)\sigma_{N0} - \mu_\infty\sigma_N - (\mu_0 - \mu_\infty)\sigma_{N0} \cdot \exp\sigma_N/\sigma_{N0} \tag{1.18}$$

being σ_s the cohesion, μ_0 and μ_∞ the initial and final friction coefficients, σ_{N0} is the normal stress at which the friction coefficient translation occurs.
The plastic strain increments are assumed to obey the normality rule.

1.1.5 Calibration and Validation

As already introduced earlier and described in details in [25],the LDPM response depends on two sets of parameters to be calibrated.

Geometrical Parameters

The first set of parameters to be calibrated is relevant to the geometrical definition of the concrete internal structure:

1. Cement Content (c)
2. Water-to-Cement Ratio (w/c)
3. Aggregate-to-Cement Ratio (a/c)
4. Maximum Aggregate Size (d_a)
5. Fuller Coefficient (n_F)
6. Minimum Aggregate Size

The first four parameters can be obtained directly from the mix design, the Fuller coefficient from the best fitting of the experimental particle-size distribution (sieve curve), the minimum aggregate size d_0 governs the resolution of the problem and it is generally chosen to be as small as possible while keeping the computational cost reasonable.

Constitutive Parameters

The second set of parameters to be calibrated is relevant to the meso-scale mechanical behavior, governing the facet constitutive laws The calibration of these parameters can be achieved through the best fitting of the complete load-displacements curves relevant to the following experimental tests: hydrostatic compression, unconfined compression, fracture test, triaxial compression at low-confinement, triaxial compression at high-confinement.

Sometimes, all the experimental curves needed for the calibration are not available, so the relevant LDPM parameters should be estimated on the basis of experimental data available in the literature and relevant to concrete mixes similar to the one being simulated.

These parameters and their effect in the response are accurately describes by Cusatis and co-workers, in [25]:

1. Normal Elastic Modulus E_0 and Shear-Normal Coupling Parameter α govern LDPM response in the elastic regime.

2. Tensile Strength σ_T and Characteristic Length ℓ_t govern the softening tensile fracturing behavior of LDPM facets and, consequently, all macroscopic behaviors featuring softening.

3. Softening Exponent n_t governs the interaction between shear and tensile behavior during softening at the facet level. At the macroscopic level, it governs the post-peak ductility observed during tensile and compressive failure simulations.

4. Shear Strength σ_s is the facet strength for pure shear and affects mostly the macroscopic behavior in compression.

5. Yielding Compressive Stress σ_{c0}, Initial Hardening Modulus H_{c0}, Transitional Strain Ratio κ_{c0} and Densified Normal Modulus E_d, define the behavior of the facet normal component under compression and affect the macroscopic behavior in compression.

6. Initial Internal Friction Coefficient μ_0, Internal Asymptotic Friction Coefficient μ_∞ and Transitional Stress σ_{N0}, contribute to LDPM response in compression, with basically no effect on tensile behavior.

7. Parameters κ_{c1} and κ_{c2} govern the nonlinear evolution of the normal facet stress in compression. κ_{c1} is the Deviatoric-to-Volumetric Strain Ratio at which rehardening after pore collapse is prevented by deviatoric strain induced damage, κ_{c2} determines the extent of this deviatoric effect on rehardening behavior

The excellent modeling capability of LDPM has been fully demonstrated, as shown in [25]. Fig. 1.5 gives some examples of numerical results achieved with LDPM simulations: not only the stress-strain curves can be accurately captured for various loading conditions but also the cracking patterns and the fractures mechanisms can be realistically simulated.

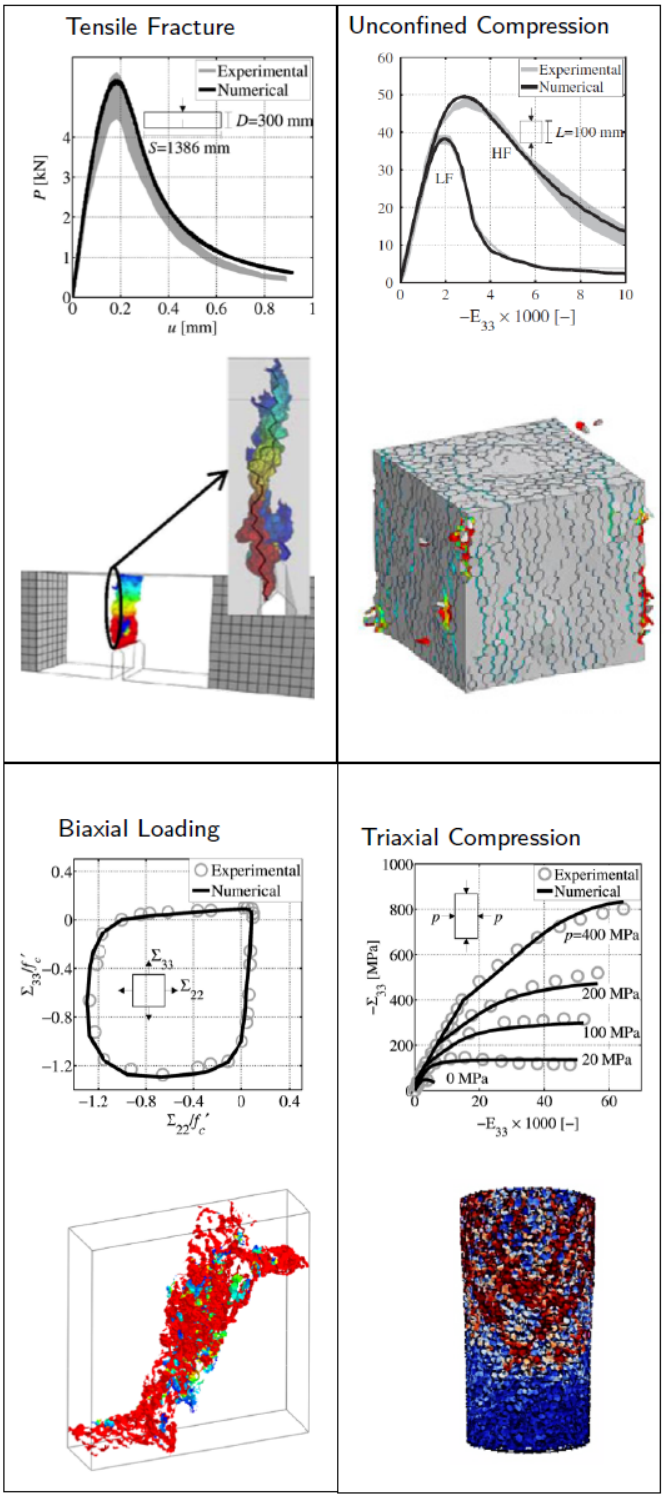

Figure 1.5: Examples of LDPM simulations results for different loading conditions

1.2 Spectral Stiffness Microplane Model for composite laminates

For the simulation of the columns wrapping, FRP jacketing has been modeled following the Spectral Stiffness Microplane Model [47], which is a general constitutive model for unidirectional and textile composite laminates able to simulate orthotropic stiffness, pre-peak nonlinearity, failure envelopes, and the post-peak softening and fracture.

1.2.1 Theoretical background on Microplane Model and Spectral Stiffness Theorem

The Spectral Stiffness Microplane Model is based on the framework of the original kinetically constrained microplane model [42] which rests on two basic ideas: (1) the constitutive relations describe microstructural phenomena not in terms of stress and strain tensors, but in terms of the stress vector and strain vector acting on planes of all possible orientations at a given point of the continuum; and (2) a variational principle is used to relate the microplane vectors to the continuum tensors.
According to [47], the Spectral Stiffness Decomposition theorem [48, 49, 50, 51] is used to extend the microplane framework to account for material anisotropy. The stiffness matrix of the composite $\mathbf{C}$ is decomposed as follows:

$$\mathbf{C} = \sum_{I} \lambda^{(I)} \mathbf{C}^{(I)} \tag{1.19}$$

where $I = 1, 2...6$, $\lambda^{(I)}$ are the eigenvalues of the stiffness matrix and $\mathbf{C}^{(I)} = \sum_n \mathbf{\Phi}_{In} \mathbf{\Phi}_{In}^T$ are a set of second-order tensors constructed from the elastic eigenvectors $\mathbf{\Phi}_I$. The I-th eigenvector $\mathbf{\Phi}_I$ has multiplicity n and is normalized such that $\mathbf{\Phi}_I^T \mathbf{C}^{(I)} \mathbf{\Phi}_I = \lambda^{(I)}$.
An important characteristic of the elastic eigenmatrices $\mathbf{C}^{(I)}$ is that they provide a way to decompose the stress and strain tensors into energetically orthogonal modes. These are called here *eigenstresses* and *eigenstrains* and are defined as:

$$\sigma_I = \mathbf{C}^{(I)} \sigma \quad \text{and} \quad \varepsilon_I = \mathbf{C}^{(I)} \varepsilon \tag{1.20}$$

It is easy to show that $\sigma = \sum_I \sigma_I$ and $\varepsilon = \sum_I \varepsilon_I$ whereas the relation between eigenstresses and eigenstrains can be found introducing the related elastic eigenvalues: $\sigma_I = \lambda^{(I)} \varepsilon_I$. By the spectral decomposition of the strain tensor and a separate projection of each eigenstrain, each microplane vector can be decomposed into mi-

croplane eigenstrain vectors as:

$$\varepsilon_P = \sum_I^N \varepsilon_P^{(I)} \qquad \text{where} \begin{cases} \varepsilon_P^{(I)} = \mathbf{P}\varepsilon^{(I)} = \mathbf{P}^{(I)}\varepsilon \\ \mathbf{P}^{(I)} = \mathbf{P}\mathbf{C}^{(I)} \end{cases} \tag{1.21}$$

where N = number of independent eigenmodes and:

$$\mathbf{P} = \begin{bmatrix} N_{11} & N_{22} & N_{33} & \sqrt{2}N_{23} & \sqrt{2}N_{13} & \sqrt{2}N_{12} \\ M_{11} & M_{22} & M_{33} & \sqrt{2}M_{23} & \sqrt{2}M_{13} & \sqrt{2}M_{12} \\ L_{11} & L_{22} & L_{33} & \sqrt{2}L_{23} & \sqrt{2}L_{13} & \sqrt{2}L_{12} \end{bmatrix} \tag{1.22}$$

is a 3×6 matrix relating the macroscopic strain tensor to the microplane strain as a function of the plane orientation. In facts, $N_{ij} = n_i n_j$, $M_{ij} = (m_i n_j + m_j n_i)/2$ and $L_{ij} = (l_i n_j + l_j n_i)/2$, where n_i, m_i and l_i are local Cartesian coordinate vectors on the generic microplane with n_i being the i-*th* component of the normal (Fig. 1.6a). With reference to the spherical coordinate system represented in Fig. (1.6b), the foregoing components can be expressed as a function of the spherical angles θ and φ: $n_1 = \sin\theta\cos\varphi$, $n_2 = \sin\theta\sin\varphi$, $n_3 = \cos\theta$ while one can choose $m_1 = \cos\theta\cos\varphi$, $m_2 = \cos\theta\sin\varphi$, $m_3 = -\sin\theta$ which gives, for orthogonality, $l_1 = -\sin\varphi$, $l_2 = \cos\varphi$ and $l_3 = 0$. In this way, different constitutive laws describing the material behavior at the microplane level can be related to each eigenmode, allowing not only the description of the material anisotropy but also to address the different damaging mechanisms related to different loading conditions. Accordingly, from the microplane eigenstrains, the microplane eigenstresses $\boldsymbol{\sigma}_P^{(I)}$ can be defined through specific constitutive laws: $\sigma_P^{(I)} = f\left(\varepsilon_{P1}, \varepsilon_{P2}...\right)\varepsilon_P^{(I)}$ and the macroscopic stress tensor can be computed in a variational sense through the principle of virtual work [47]:

$$\sigma = \frac{3}{2\pi}\int_\Omega \mathbf{P}^T \sum_I^N \sigma_P^{(I)} \mathrm{d}\Omega \tag{1.23}$$

where Ω is the surface of a unit sphere representing all the possible microplane orientations.

1.2.2 Constitutive laws

Elastic Behavior

The elastic behavior is formulated by assuming that normal and shear eigenstresses on the microplanes are proportional to the corresponding eigenstrains:

$$\sigma_N^{(I)} = \lambda^{(I)}\varepsilon_N^{(I)}, \quad \sigma_M^{(I)} = \lambda^{(I)}\varepsilon_M^{(I)}, \quad \sigma_L^{(I)} = \lambda^{(I)}\varepsilon_L^{(I)} \tag{1.24}$$

where $\lambda^{(I)} = I$-th elastic eigenvalue.

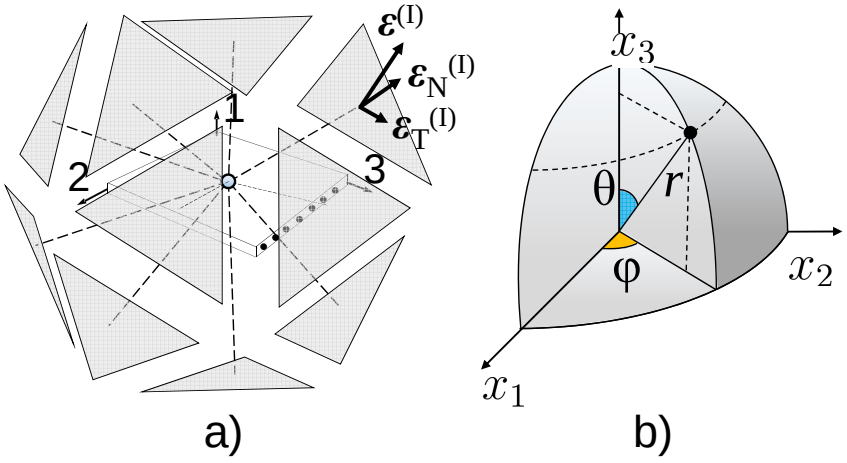

Figure 1.6: a) Mesostructure tessellation b) Three dimensional discrete cells c) Definition of nodal degrees of freedom and contact facets in two-dimensions.

Constitutive laws: inelastic behavior

Similar to Cusatis *et al.* [52, 24],the inelastic constitutive laws for each eigenmode are expressed introducing an *effective eigenstrain* defined as: $\varepsilon^{(I)} = \sqrt{(\varepsilon_N^{(I)})^2 + (\varepsilon_T^{(I)})^2}$ where $\varepsilon_T^{(I)} = \sqrt{(\varepsilon_M^{(I)})^2 + (\varepsilon_L^{(I)})^2}$= total shear strain component of I-th microplane eigenstrain.The relation between the stress and strain microplane components can be found introducing an *effective eigenstress*, $\sigma^{(I)}$ and imposing the consistency of the virtual work:

$$\delta\mathcal{W}_I = \sigma^{(I)}\delta\varepsilon^{(I)} = \frac{\sigma^{(I)}}{\varepsilon^{(I)}}\left(\varepsilon_N\delta\varepsilon_N + \varepsilon_M\delta\varepsilon_M + \varepsilon_L\delta\varepsilon_L\right)^{(I)} = (\sigma_N\delta\varepsilon_N)^{(I)} + (\sigma_M\delta\varepsilon_M)^{(I)} + (\sigma_L\delta\varepsilon_L)^{(I)} \tag{1.25}$$

By means of Eq. (1.25), the relationship between normal and shear stresses versus normal and shear strains can be formulated through damage-type constitutive equations:

$$\sigma_N^{(I)} = \left(\sigma\frac{\varepsilon_N}{\varepsilon}\right)^{(I)}, \quad \sigma_M^{(I)} = \left(\sigma\frac{\varepsilon_M}{\varepsilon}\right)^{(I)}, \quad \sigma_L^{(I)} = \left(\sigma\frac{\varepsilon_L}{\varepsilon}\right)^{(I)} \tag{1.26}$$

The effective stress $\sigma^{(I)}$ is assumed to be incrementally elastic, i.e. $\dot{\sigma}^{(I)} = \lambda^{(I)}\dot{\varepsilon}^{(I)}$ and it is formulated such that $0 \leq \sigma^{(I)} \leq \sigma_{bi}^{(I)}(\varepsilon^{(1)}, \varepsilon^{(2)}..., \theta, \varphi)$ where $\sigma_{bi}^{(I)}(\varepsilon^{(1)}, \varepsilon^{(2)}..., \theta, \varphi)$

with subscript i =t for tension and i =c for compression is a limiting boundary enforced through a vertical (at constant strain) return algorithm. It is worth mentioning here that, in general, $\sigma_{bi}^{(I)}$ is a function of the microplane orientation and of the equivalent strains pertaining to other modes. This allows to inherently embed in the formulation the effects of damage anisotropy and the interaction between damaging mechanisms.

Inelastic behavior in the fiber direction

It was shown in [47] that the stiffness tensor for a UD composite, treated as transversely isotropic, can be decomposed into 4 energetically orthogonal eigenmodes, each being associated to a particular type of deformation. Mode 1 is related to the normal and shear deformation in out-of-plane direction, mode 2 is related to a macroscopic normal deformation in the direction of the fibers, mode 3 is associated to an in-plane normal deformation orthogonal to the fibers and mode 4 is related to in-plane shear deformation. In this work, it is assumed that failure of the composites happens mainly by fiber failure and pullout. Accordingly, a strain dependent nonlinear constitutive law is defined for mode 2 whereas elastic behavior is assumed for all the other modes. This assumption is largely supported by the experimental analysis of the fracture surfaces of the failed composite jackets. The strain dependent boundary in tension, $\varepsilon_N^{(2)} \geq 0$, can be expressed by the following equations:

$$\sigma_{bt}^{(2)} = s^{(2)}(\theta,\varphi) \exp\left[- \left(\frac{\left\langle \varepsilon_{\max}^{(2-t)} - \varepsilon_{0t}^{(2)} \right\rangle}{k_{bt}^{(2)}} \right)^{a_{t2}} \right] \tag{1.27}$$

where $s^{(2)}(\theta,\varphi) = s_0^{(2)} \cos^2(\theta)$ with $s_0^{(2)}$ = mode 2 microplane tensile strength. The boundary $\sigma_{bt}^{(2)}$ evolves exponentially as a function of the maximum effective strain, which is a history-dependent variable defined as $\varepsilon_{\max}^{(2-t)}(t) = \max_{\tau \leq t}[\varepsilon^{(2)}(t)]$. The exponential decay of the boundary σ_{bt}^2 starts when the maximum effective strain reaches its elastic limit $\varepsilon_{0t}^{(2)}(\theta,\varphi) = s^{(2)}/\lambda^{(2)}$. For the sake of simplicity, the behavior of the composite has been assumed linear elastic in compression, failure always occurring in tension for the cases under study. The total number of required parameters to describe mode 2 in tension is 3 and they should be calibrated according to the experimental behavior.

Chapter 2

New constitutive law for concrete in compression

Preliminary simulations revealed that the constitutive law in compression governs the post-peak response of FRP-reinforced concrete. The original LDPM formulation, described in chapter 1 and with more details in [24], has been conceived for describing the strain hardening plasticity under high compressive hydrostatic deformations, with micro and meso-scale pore collapse under load followed by a densification due to the contact between completely collapsed pores. In fact, its aim was to capture concrete re-hardening behavior after yielding due to compaction under high confinement pressures.

The aforementioned constitutive law, though, has shown its limits when applied to the low confinement stress states, which are typical of the FRP confinement problems: the Hardening Modulus Function H_c, defined in Eq.1.17 revealed to be not suitable for the negative deviatoric-to-volumetric strain ratios, generally experienced by the material in these cases. In fact, when transitioning from negative to positive volumetric strains, the original formulation provides for a discontinuity in the definition of H_c (figure 2.1a) such that the material appears to gain strength during the dilatation process, because of the sudden increase in value of H_c itself. This response is unrealistic and in contrast with the well known phenomenon of hardening in compression due to the material densification, which is correctly described for the positive deviatoric-to-volumetric strain ratios: the Hardening Function increases during the process of volume contraction, allowing to accurately model the improvement in strength experienced by highly confined materials. The same formulation, though, cannot be properly used in case the material volumetric deformations transition from positive to negative values, which is typical of low confined concrete and, in particular, FRP confined concrete. This happens because of the sudden drop in the Hardening function, implying in turn a sudden drop in the material strength.

Figure 2.2 illustrates the typical deformative behavior of FRP confined concrete

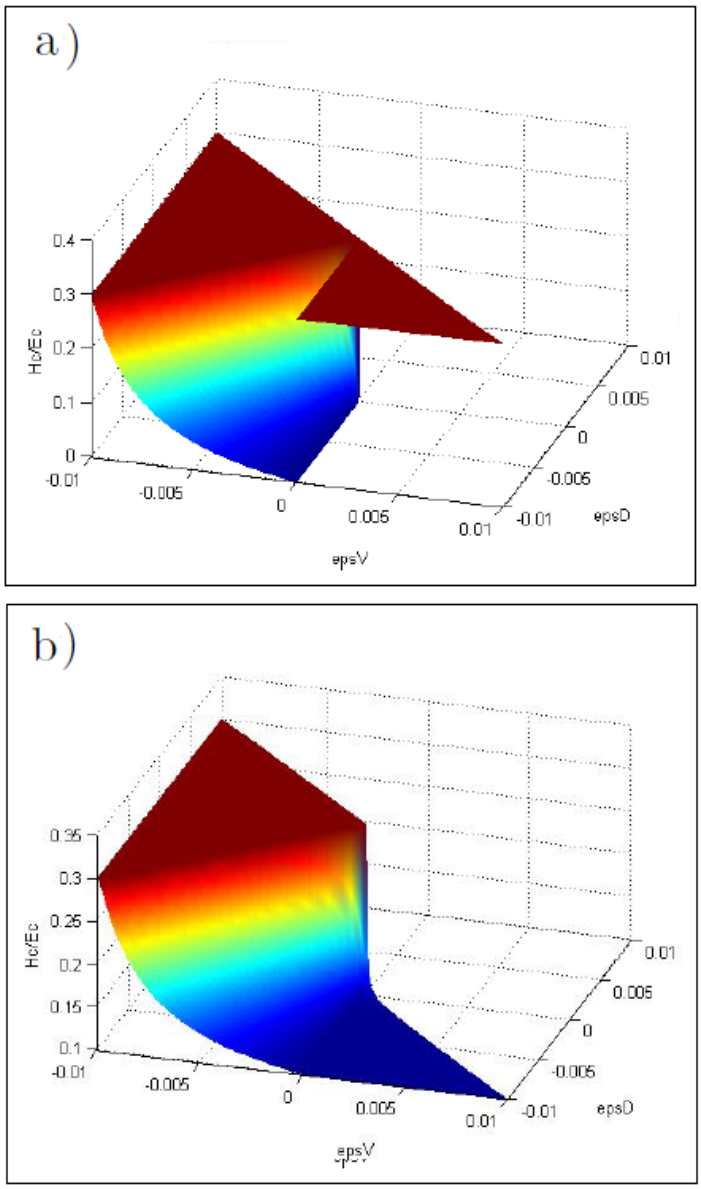

Figure 2.1: 3D plot of the Hardening Modulus Function (Hc) a) before the modification and b) after the modification

columns compared to unconfined concrete columns, from experimental data by [41]. The deviatoric strain - axial strain curves, where strains are computed as defined in chapter1, are regularly increasing for both confined and unconfined concrete specimens, while the volumetric strain - axial strain curves show a different tendency: after an initial compaction, the material expands as long as the external confine-

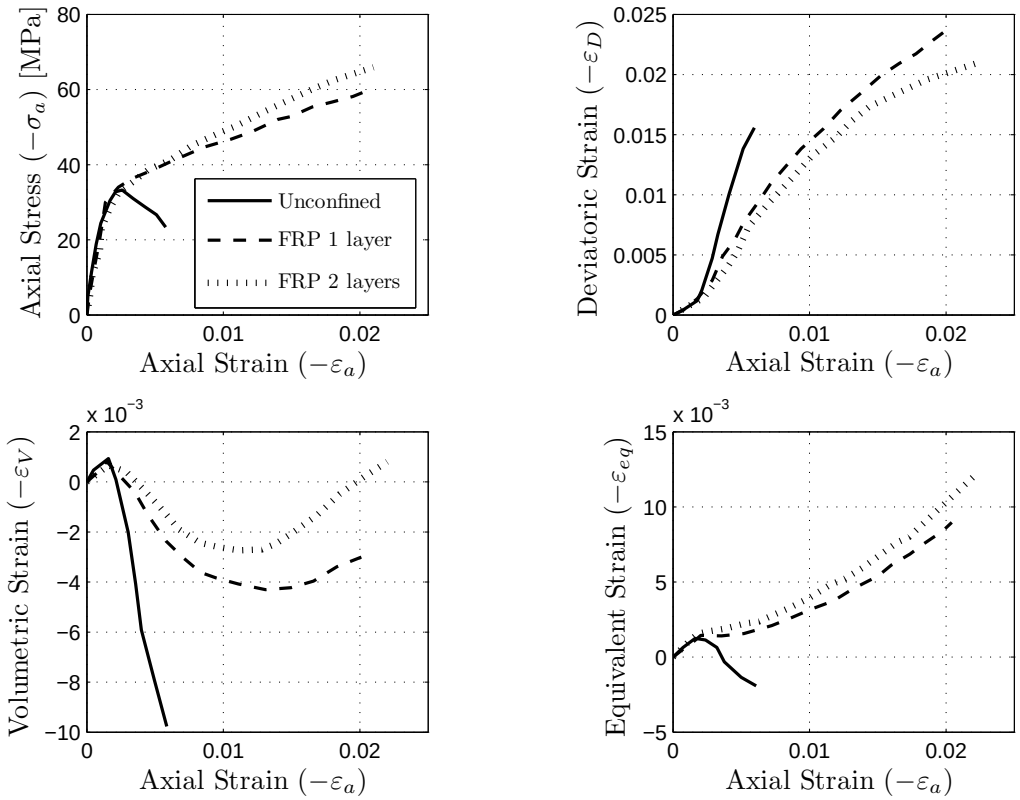

Figure 2.2: Stress-strain responses of FRP confined concrete

ment is able to contrast it by constraining the lateral deformations. The stiffer the wrapping, the sooner the material can reverse the dilation trend and experience re-compaction. If the confining stress is high, the material do not experience dilation at all.

The same behavior is shown in figure 2.3, where the axial stress is plotted against the volumetric strain for both actively and passively confined concrete specimens. As detailed described in [1], for active confinement, the change from compaction to dilation occurs at different stress levels depending on the confining pressure, and thereafter the dilation tendency remains until failure. For passive confinement, instead, the dilatation can be taken over again by compaction, therefore the accurate description of the Hardening Function around the zero volumetric strains is particularly crucial in this case. A new definition for the Hardening Module is proposed in this work with (2.1), to overcome the jump in the H_c function and allow a continuous hardening with compaction:

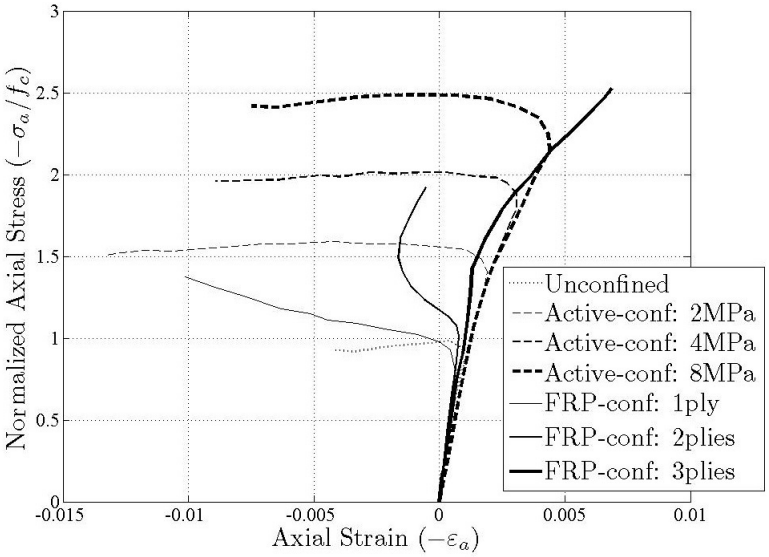

Figure 2.3: Stress-Volumetric strain responses of confined concrete

$$H_c = \begin{cases} \dfrac{H_{c0} - H_{c1}}{1 + \kappa_{c2} \langle r_{DV1} - \kappa_{c1} \rangle} + H_{c1} & \text{for } \varepsilon_V \leq 0 \\ \dfrac{H_{c0} - H_{c1}}{1 + \kappa_{c2} \langle r_{DV2} - \kappa_{c1} \rangle} + H_{c1}, & \text{for } \varepsilon_V > 0 \end{cases} \tag{2.1a}$$

$$r_{DV1} = -\frac{|\varepsilon_D|}{\varepsilon_V - \varepsilon_{V0}}; \qquad r_{DV2} = \frac{|\varepsilon_D|}{\varepsilon_V} \tag{2.1b}$$

with $\varepsilon_{V0} = \kappa_{c3}\varepsilon_0 = 0.1 \cdot \varepsilon_0$ and H_{c1} to be calibrated.
This new function permits a smooth and coherent transition from contraction to expansion and vice versa: the Hardening Modulus decreases for increasing volumetric strain and increases for increasing deviatoric strains.

Chapter 3

Numerical Analysis of FRP confined concrete columns

3.1 Summary of the experimental tests

The experimental tests performed by Wang and Wu [41] have been taken as a reference for the present numerical study, where concrete specimens (width/height = 150 mm/300 mm) with different corner radii (see figure 3.1), unconfined and wrapped by 1 or 2 CFRP plies (equivalent thickness per layer s = 0.165 mm), are subjected to uniaxial compression. The C30 series has been considered and the elastic properties of the materials are summarized in table 3.1. For the CFRP, the manufacturer values are reported. In particular, parameters shown in table 3.2 are

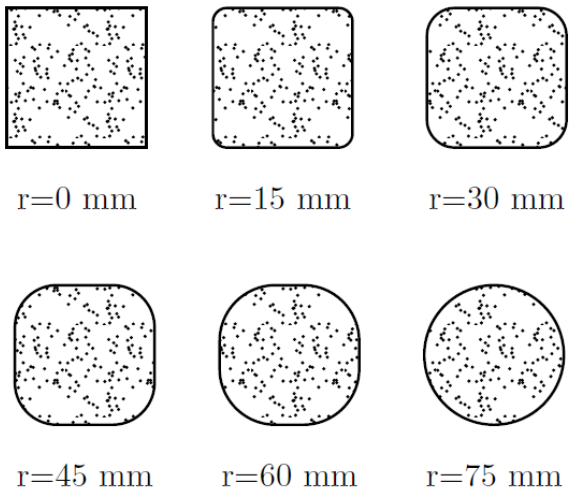

Figure 3.1: Corner radius variations of the column section

Table 3.1: Elastic Properties of Materials

Mechanical Constant	Concrete	FRP: fibres
Modulus of Elasticity (MPa)	30000	230000
Poisson's ratio	0.2	-
Compressive strenght (MPa)	32	-
Tensile strenght (MPa)	3	3482

considered a good summary of the mix design characteristics for concrete.
After sanding and cleaning the specimen surface, the FRP was wrapped around it by the manual lay-up procedure, orienting the fibers in the hoop direction and forming one or two layers. Strain gauges were mounted prior to the testing at multiple points at the mid-height of the specimens to measure the strains at different locations of the CFRP laminate. Three identical specimens had been manufactured for each geometry and the average response was taken into account.

Table 3.2: Concrete Mix Design Parameters

Mix Design Parameters		
c	280 kg/m^3	*estimated*
w/c	0.77	*from [41]*
a/c	7.5	*estimated*
d_a	10 mm	*from [41]*
n_F	0.5	*estimated*

3.2 Model Generation

Firstly, the geometry of the concrete meso-structure is computationally generated, defining the coarse aggregate particles and their interconnections from a first set of parameters taken form the mix design shown in table 3.2, through the procedure described in chapter 1. The last parameter (minimim aggregate size, d_0= 5 mm) governs the resolution of the model.

A second set of parameters is required for the definition of the facet constitutive law [24, 25] and their calibration is supposed to be obtained through the best fitting of the complete load-displacement curves relevant to different experimental tests, in particular hydrostatic compression, unconfined compression, fracture test, triaxial compression at low-confinement, triaxial compression at high-confinement are needed for a direct and complete calibration. In the present study, all the needed experimental curves were not available from Wang and Wu [41], consequently some of the parameters have been estimated from other available experimental data con-

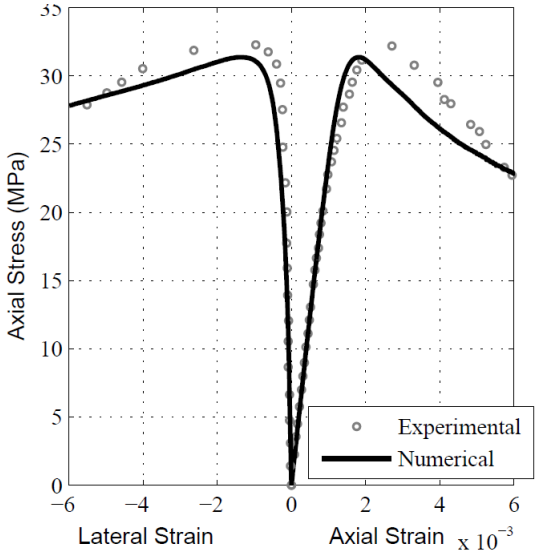

Figure 3.2: Fitting of the experimental curves for the cylindrical column during the calibration process and cracking patterns of the plain concrete column during the loading history .

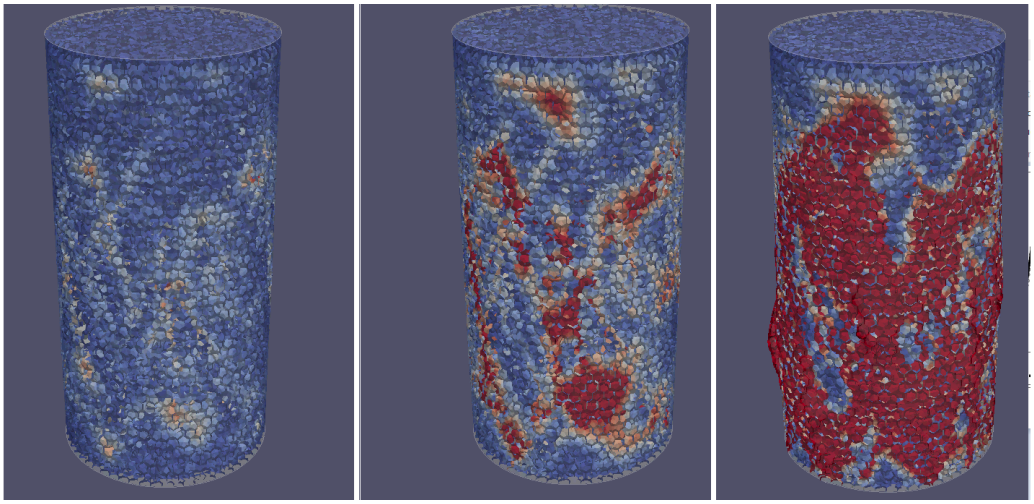

Figure 3.3: Cracking patterns development of the plain concrete column during the compressive loading history.

sidered relevant to the simulated concrete mix. The experimental axial stress- axial strain curve and the axial stress-lateral strain were fitted for unconfined concrete (cylindrical column) using the following parameters: $E_0 = 40000$ MPa, $\alpha = 0.25$, $\sigma_t = 3.65$ MPa, $l_t = 200$ mm, $\sigma_s/\sigma_t = 2.5$, $n_t = 0.2$, $\sigma_{c0} = 45$ MPa, $H_{c0}/E_0 = 0.3$, $\kappa_{c0} = 4$, $\kappa_{c1} = 1$, $\kappa_{c2} = 5$, $\kappa_{c3} = 0.1$, $\mu_0 = 0.2$, $\mu_\infty = 0$, $\sigma_{NO} = 600$ MPa, $E_d/E_0 = 1$.

The load is applied as an imposed velocity of 10 mm/s through steel platens,

modeled as rigid bodies, directly in contact with the specimens ends to simulate high friction conditions. Specifically, the constraint forces the set of top and bottom nodes of the specimen to move over the platen surface with a master-slave formulation for the direction perpendicular to the surface and with a stick-slip friction model for the resistance to sliding within the plane. The friction factor μ is computed as a function of the contact slippage s $\mu(s) = \mu_d + (\mu_s - \mu_d)s_0/(s_0 + s)$ with the friction parameters optimized for high friction ($\mu_s = 0.13$, $\mu_d = 0.015$, $s_0 = 1.3$ mm) according to Cusatis and coworkers [25]. Figure 3.7 shows an example of the geometry representation of the LDPM structures with facets and the rigid plates for the boundary conditions.
The FRP jackets are modeled as quadrilateral shell elements with physical hourglass stabilization and they are given the orthotropic behavior through the described spectral stiffness microplane model, which allows to orient the fibers in the hoop direction. The shell integration scheme has been intended for composite shells consisting of multiple layers and employs a full tensorial material formulation, with internal degrees of freedom across the thickness, so that the transversal strains can properly be characterized. Four Gauss integration points are used. The mechanical properties of the CFRP laminates are assigned according to the manufacturer data (Elastic Modulus in the matrix directions: $E_1 = E_2 = 3000$ MPa, Elastic Modulus in the fiber direction: $E_3 = 230000$ MPa, Poisson Ratio in plane: $\nu_{31} = \nu_{32} = 0.25$) [41, 18] or estimated from literature (Shear Modulus out of plane: $G_{12} = 1300$ MPa, Shear Modulus in plane: $G_{13} = G_{23} = 4000$ MPa). The interaction between the concrete column and the FRP plies is modeled through a master-slave formulation where the FRP nodes are forced to lay on the external lateral surface of the concrete column, without constraining rotations.

3.3 Results with linear elastic FRP

At first, in order to evaluate the new constitutive law for concrete in compression and check the overall model, the simulations have been carried out considering the FRP as a linear elastic material, not activating the boundaries controlling inelasticity in the fibers direction.
The uniaxial stress vs strain curves are reported in figures 3.5 and 3.6, where each graph shows the experimental and numerical response for unconfined specimen compared to 1 FRP ply and 2 FRP plies confined specimens. Similarly to the experiments, the axial stress shown is obtained by dividing the global axial force over the concrete section area, the axial strain is obtained by dividing the global axial displacement over the specimen height and the lateral strain as an average of the radial displacements over the undeformed radial length, measured at the middle of each side face and at the center of each corner, in the middle height of the specimen. The comparison between numerical and experimental results proves that, after the

calibration of the LDPM parameters for the unconfined concrete curve, the developed model can capture the general trend of the FRP-confined columns in compression. As well-known from the majority of existing experimental tests, the axial stress axial strain curves of CFRP-confined concrete are characterized by a monotonically ascending bilinear shape (the turning point is always around the onset of the unconfined concrete strength) in contrast with the softening branch typical of actively confined concrete. In fact, as the axial stress increases, the confining pressure provided by the jacket also increases instead of remaining constant and if the stiffness of FRP exceeds a certain threshold value, this confining pressure increases fast enough to ensure that the stress strain curve is monotonically ascending. Naturally, the higher the FRP stiffness, the higher the slope of the second branch. This typical evolution of stress-strain can be captured for different number of FRP layers with the current model, as shown in figure 3.5. The corner radius effect is also captured: the post peak behavior after the onset of the unconfined concrete strength is related to the section shape and the post peak stiffness is higher for columns with a larger corner radius, as the experiments already showed. The model can reproduce efficiently not only the uniform but also the non uniform confinement effects and simulate the reduction of confinement efficiency with the decreasing of the corner radius.

The behavior of sections with more rounded corners (radius from $r = 75$ mm to

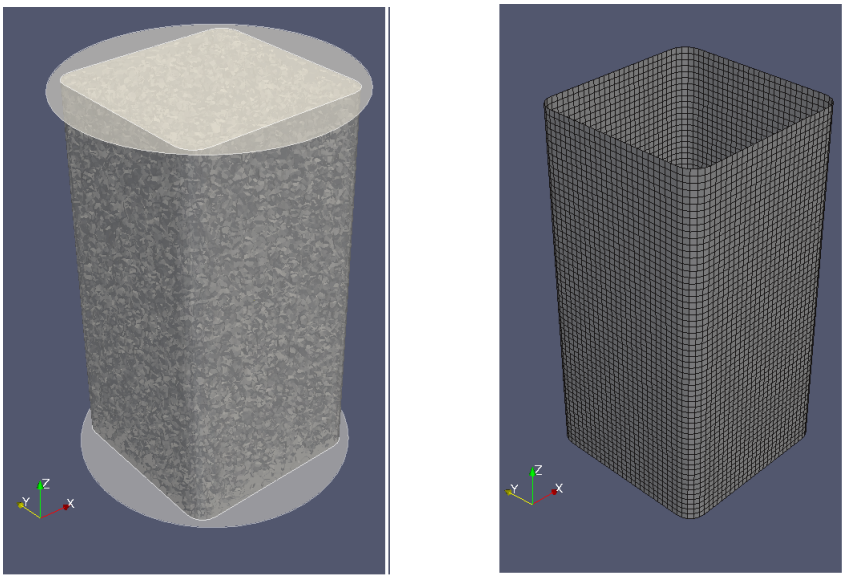

(a) Concrete Column with loading plates

(b) FRP jacketing

Figure 3.4: Model example of column (r=15 mm)

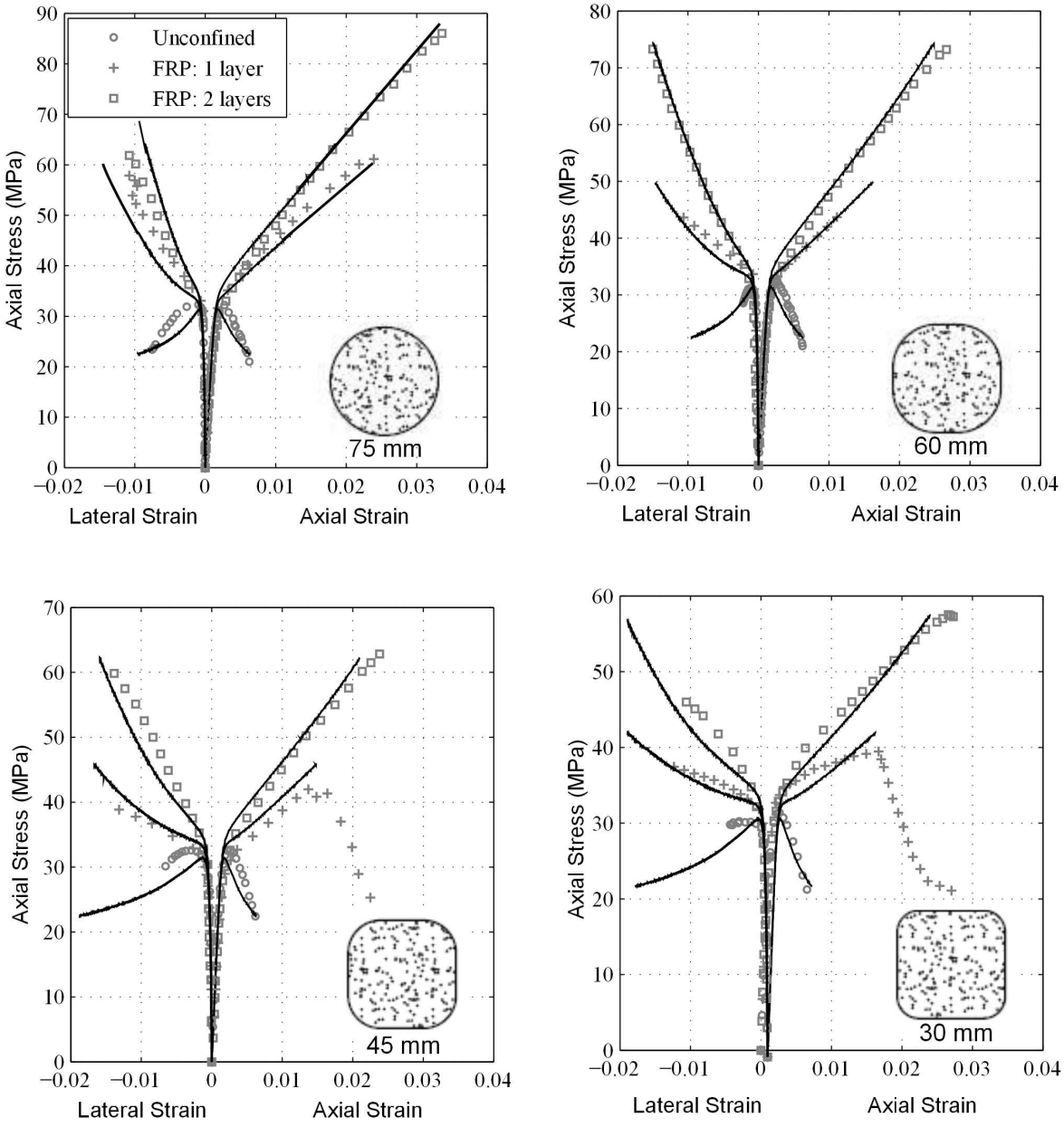

Figure 3.5: Typical stressstrain curves measured in the experiments and predicted by the analysis with elastic FRP. Rounded Corners Set.

$r = 30$ mm) is almost perfectly captured, while this is not longer true for sections with smaller corner radii ($r = 15$ mm and $r = 0$ mm), where the FRP fracture mechanisms seem to become essential for the overall column response to be captured. In fact, the FRP plies can experience high stress concentrations around the

corners, leading to progressive rupture of the material and, consequently, a softening behavior of the FRP confined square sections. However, the numerical simulations can catch some interesting aspect; for instance, being the confining effect given by the wrapping highly non uniform and less effective in case of square sections, it can happen that, initially in the loading history, the increase in confinement pressure is not fast enough to ensure that the stress-strain curve is monotonically ascending and then, after softening, a further increase in stress occurs due to the later increase of lateral deformation. This phenomenon has been observed and described in literature (e.g. [6]) and it is well captured by the model as shown in figure 3.6. In the experimental tests, though, these aspects interact with the FRP rupture, lacking so far in the model.

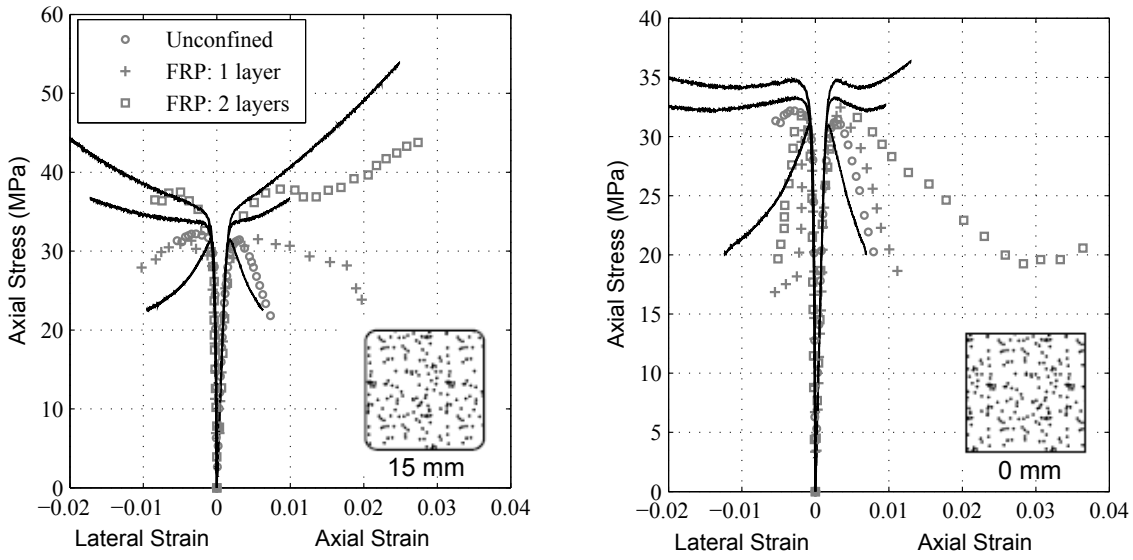

Figure 3.6: Typical stressstrain curves measured in the experiments and predicted by the analysis with elastic FRP. Square Corners Set.

3.4 About FRP ultimate condition

3.4.1 Experimental observations

The eventual failure of FRP-confined column is due to the rupture of the FRP jacket, so the ultimate tensile strain or tensile strength of the confining FRP jacket in the hoop direction [1]. Although in many existing theoretical or numerical models [53, 54] the tensile rupture of FRP is assumed when the hoop stress reaches the tensile strength given from material tests such as coupon tests, different experimental results have shown that the hoop rupture strains of FRP measured in FRP-confined columns are on average significantly lower (e.g. [55, 56, 57, 58]). Also Wang and Wu [41] report that the FRP ultimate strain of many tested specimens is at least 25% below that of the coupon test and the reduction is more significant in the corners and in case of multiple layers. Several potential causes for the variability in the empirical strain efficiencies are suggested in the literature, however, no rational model is currently available to account for these observations. and, as reported by Chen and coworkers (2013) [59] there is little consensus on this issue in the literature. A systematic analysis of the factors influencing the ultimate condition of FRP-wrapped concrete columns is given in [59], where different contributory causes have been highlighted to affect the composite rupture; the material does not allow any stress redistribuition because of its elastic brittle nature so the identification of the highest tensile strain is decisive to understand the column collapse mechanisms. In particular, the following factors have been considered potentially important:

1. geometrical factors: geometrical discontinuities, FRP overlap region, geometrical imperfections and curvature of the FRP jacket;

2. FRP material factors: unintentional fiber orientation, misalignment and uneven tension of fibers, damage of fibers, triaxial stress state in the FRP;

3. concrete material factors: nonuniform deformation and strain localization in concrete;

4. adhesive material and geometry factors: mechanical properties an geometrical details of the adhesive;

5. loading factors: eccentric or non uniform loading, stressing attributable to thermal deformation and creep.

The numerical model developed in the present paper is able to account for the concrete material factors, being LDPM a mesoscale model. The non uniform local deformations on concrete leads to a non uniform strain deformation in the FRP, in both the circumferential and axial direction, which in fact can be captured as well as the FRP strain localization resulting from concrete cracking. By contrast, the

FRP jacket is modeled using shell elements with respect to the nominal thickness of fibers, so the numerical simulation cannot be sensitive to any FRP material or geometrical factor related to the fibers or adhesive. In order to take these phenomena into account, a stochastic model has been used for the composite strength.
Infact, it has been seen from experiments that FRP failure initiation occurs without extensive inelastic strain redistribution. In this case, the process of failure is strongly affected by the random distribution of the strength and fracture properties of the material and this aspect has been addressed in this contribution assigning a statistical distribution of strength to each shell element used to model the composite material. Conveniently calibrating the probabilistic function, all the factors governing the premature failure can be included in the form of uncertainty.

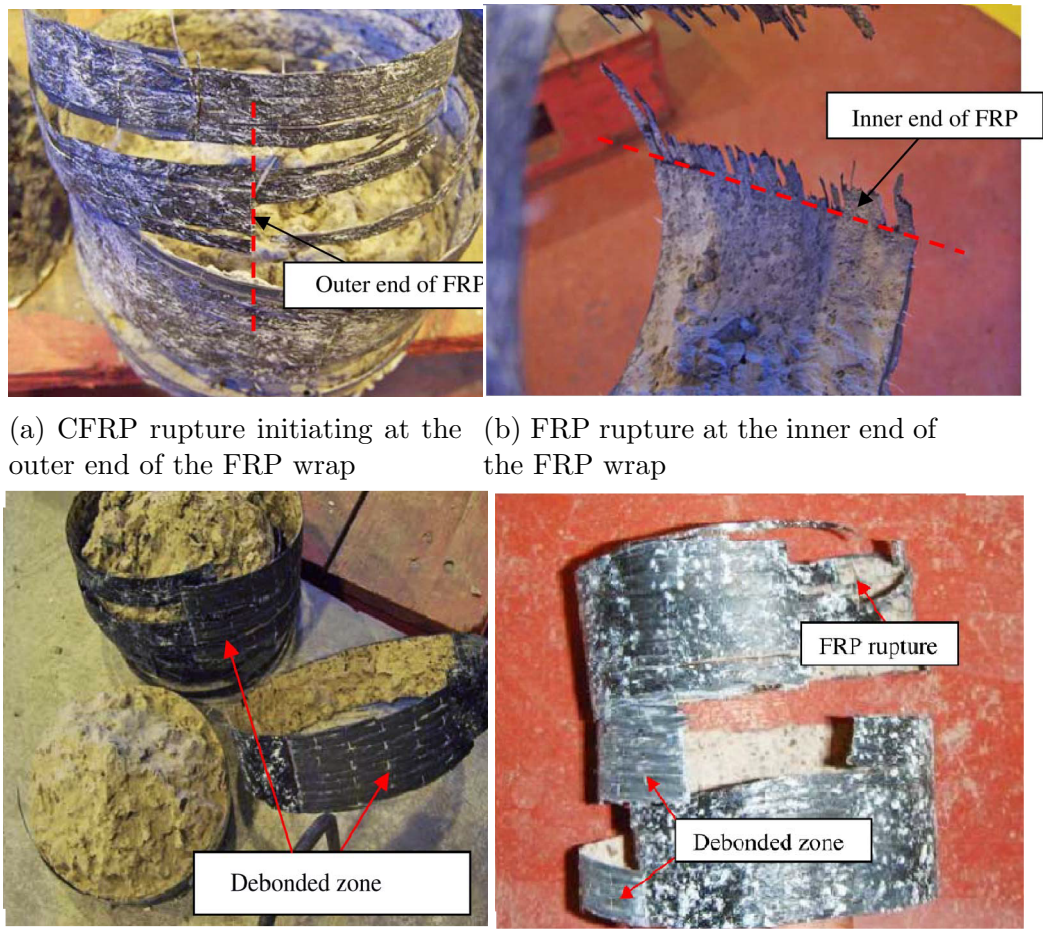

(a) CFRP rupture initiating at the outer end of the FRP wrap

(b) FRP rupture at the inner end of the FRP wrap

(c) Debonding failure of FRP

(d) Mixed FRP debonding and fracture failure

Figure 3.7: Example of FRP failure modes, from [59]

3.4.2 Stochastic model for composite strength

Recent studies by Bažant and co-workers [60, 61] have shown that the strength of one Representative Volume Element (RVE) of a quasibrittle material follows a Gaussian distribution grafted to a power law in the tail of probability within the range of 10^{-5} to 10^{-3}:

$$\begin{array}{lcll} P_1(\sigma) & = & 1-\exp(-\langle\sigma\rangle^m/b_0^m) & \text{for} \quad \sigma < \sigma_{gr} \\ P_1(\sigma) & = & P_{gr} + \frac{r_f}{\sqrt{2\pi}\delta_G}\int_{\sigma_{gr}}^{\sigma} e^{-(\sigma'-\mu_G)^2/2\delta_G^2} d\sigma' & \text{for} \quad \sigma \geq \sigma_{gr} \end{array} \tag{3.1}$$

where $\langle x\rangle = \max(x,0)$ = Macaulay brackets, μ_G and δ_G are the mean and standard deviation of the Gaussian core if considered extended to $-\infty$, b_0 and m are the scale and shape parameters of the Weibull tail, r_f is a scaling parameter required to normalize the grafted cdf such that $P_1(\infty) = 1$, P_{gr} = grafting probability $= 1 - \exp[-\sigma_{gr}^m/b_0^m]$. The continuity of the probability density function at the grafting stress requires that: $(\mathrm{d}P_1/\mathrm{d}\sigma)|_{\sigma_{gr}^+} = (\mathrm{d}P_1/\mathrm{d}\sigma)|_{\sigma_{gr}^-}$ where P_1 denotes the failure probability of one RVE. The foregoing distribution has been used in this

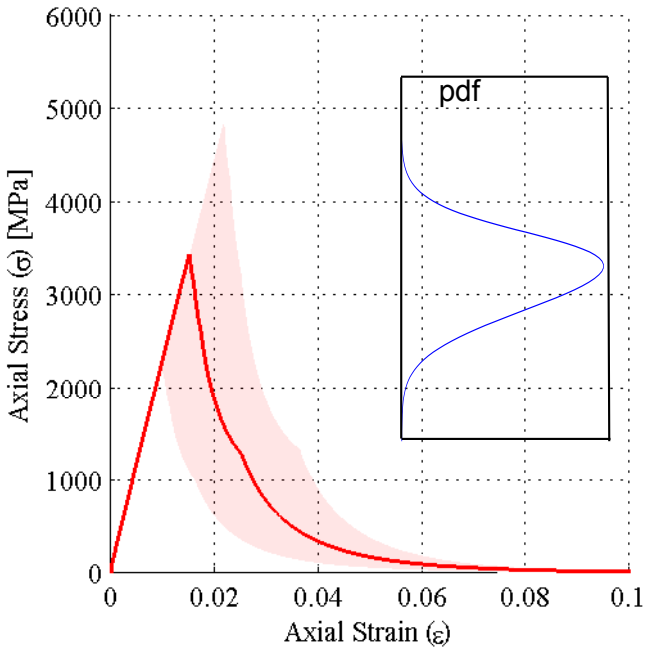

Figure 3.8: Stress-Strain Curve in the Fibers direction with associated pdf

work for the assignation of random strength. Strength autocorrelation has not been considered, the adopted element size being much larger than the expected autocorrelation length (which, for UD composites, is expected to be no larger than 2-3 mm

[62, 63]). This rather simplified the process of random strength assignation to the N elements describing the FRP. This process consisted of two steps: 1) generation of N independent standard Gaussian variables by Latin Hypercube Sampling using the mean value of each subinterval and reordering their values to minimize spurious correlation [64]; 2) computation of random strength according to Gauss-Weibull distribution by isoprobabilistic transformation: $\sigma(\boldsymbol{x}) = P_1^{-1}(\Phi_G(\boldsymbol{x}))$ where $\Phi_G(\boldsymbol{x}) =$ standard Gaussian cdf.
The parameters of the Spectral Stiffness Microplane Model governing the inelastic behavior of the fibers have been calibrated according to given ultimate stress and strain values fracture energy ($G_f = 260$ N/mm). Spurious mesh sensitivity due to train localization was avoided by means of the crack band model. For a 5 mm $\times$5 mm shell element the calibrated parameters for the microplane model definition are the following: $s_0^{(2)} = 3482$ MPa, $k_{bt}^{(2)} = 0.04$. The parameters governing the stochastic formulation, estimated according to [62, 63] are the following: $m = 56$, $b_0 = s_0^{(2)}$, $P_{gr} = 10^{-5}$, $\mu_G = 1.05 \times b_0$, $\delta_G = 0.1 \times \mu_G$, then $r_f = (1 - P_{gr})/[1 - \Phi_G(\sigma_{gr}, \mu_G, \delta_G)]$ where Φ_G is the Gaussian cdf with average μ_G and S.D. δ_G.

3.5 Results

3.5.1 Results for columns with largest corner radius

The model with the previously described non-linear constitutive features for the FRP sheets allows to capture accurately enough the ultimate condition of the tested FRP confined columns with larger corner radius. In particular, figure 3.9 shows the comparison between the experimental and numerical results for the set of columns with rounded corners: one can observe that non only the typical stress-strain loading curves are well captured for the different shapes and thickness of the FRP wrapping, as already mentioned, but also the ultimate strength of the columns together with the ultimate strain are caught with a very good approximation, which is unique in terms of numerical models for FRP confined concrete columns.

Figures 3.10,3.11,3.12,3.13 show snapshots of the stress distribution pattern in the FRP jacket at the ultimate condition with the fracture location and the corresponding cracking pattern in the FRP column. The fracture mechanisms are well captured by the model, which is the reason for such accurate fitting of the experimental loading curves and it is interesting noticing that the FRP jacket breaks exactly where the shape of the cross section changes from the rounded corner to the flat side part, where it has been experimentally demonstrated the fracture more often occurs and starts developing.

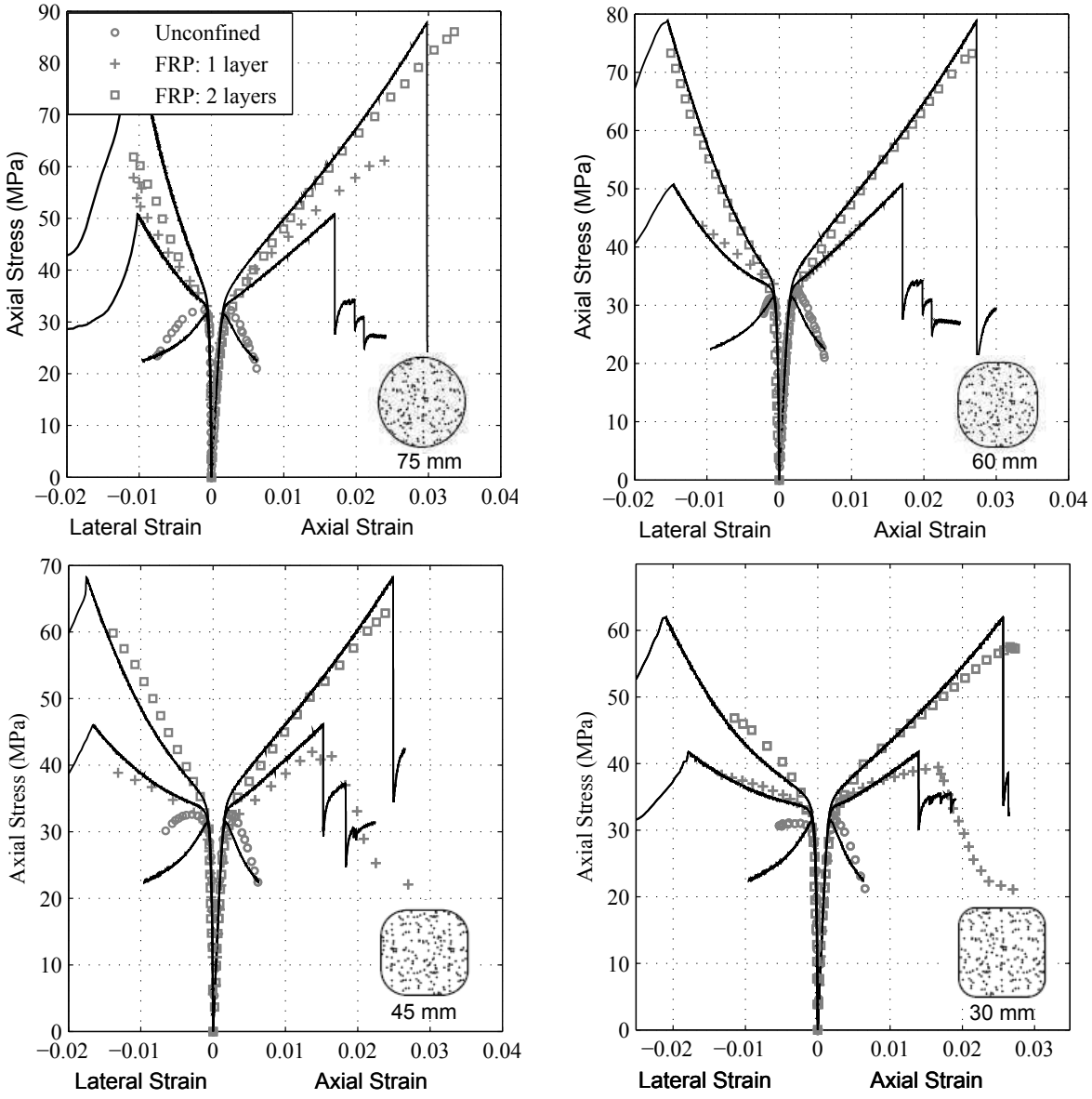

Figure 3.9: Typical stressstrain curves measured in the experiments and predicted by the analysis with non-linear FRP. Rounded Corners Set.

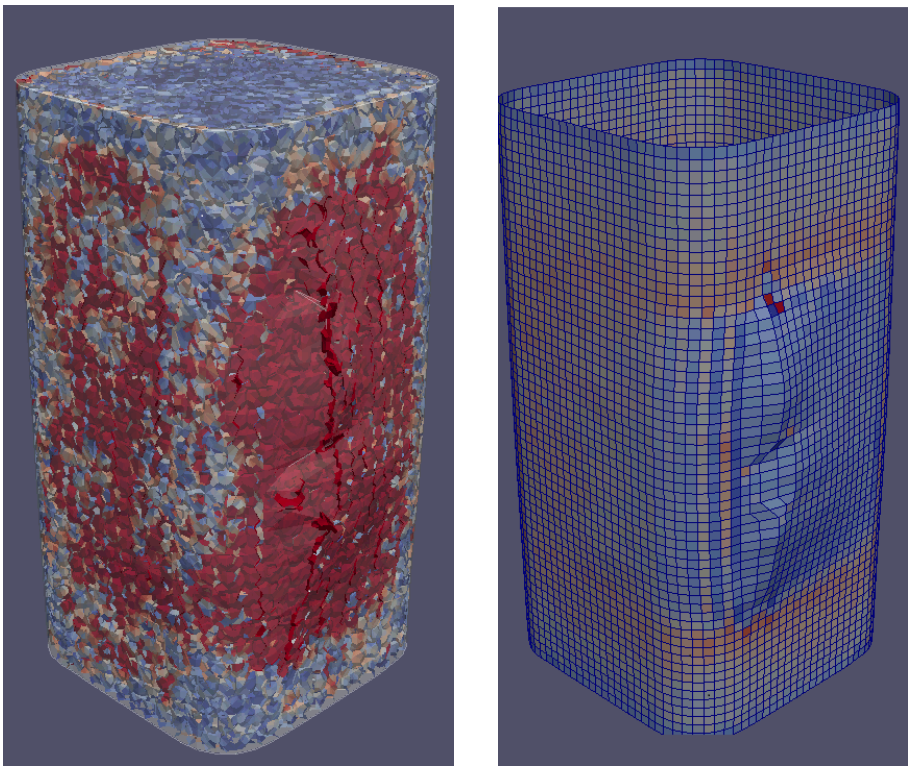

(a) Cracking Patterns in the Concrete Column

(b) Fracture in the FRP jacketing

Figure 3.10: Example of ultimate Condition for FRP confined column (r=30 mm)

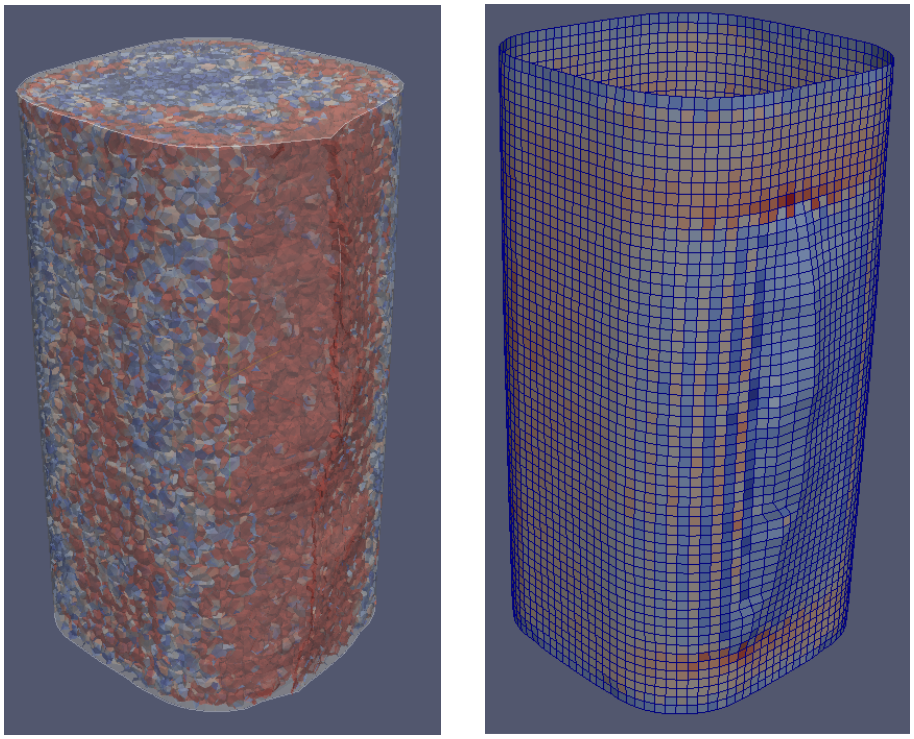

(a) Cracking Patterns in the Concrete Column

(b) Fracture in the FRP jacketing

Figure 3.11: Example of ultimate Condition for FRP confined column (r=45 mm)

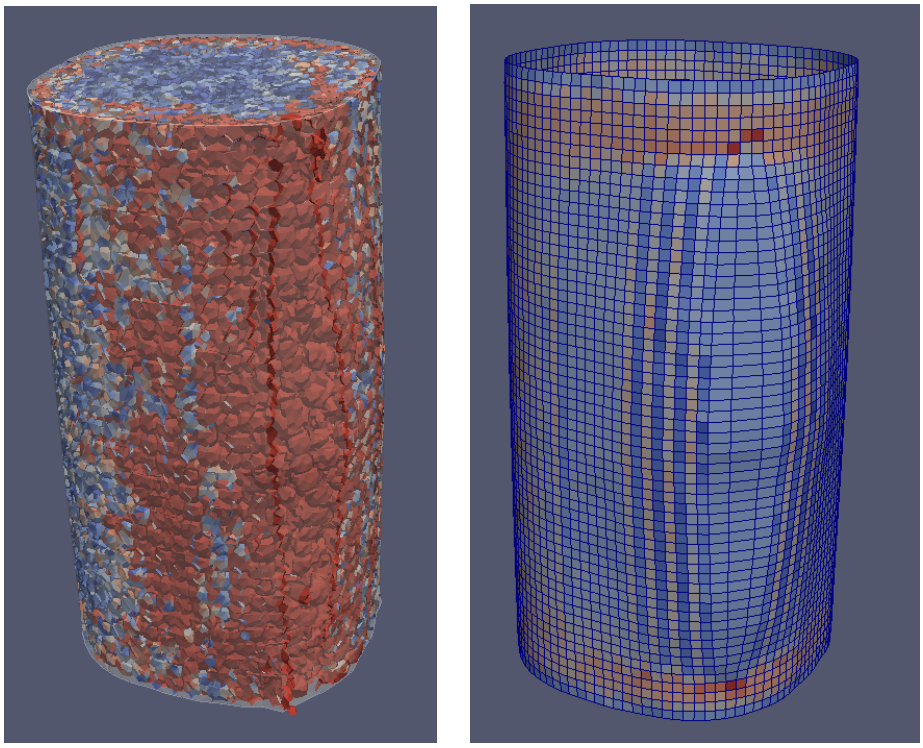

(a) Cracking Patterns in the Concrete Column

(b) Fracture in the FRP jacketing

Figure 3.12: Example of ultimate Condition for FRP confined column (r=60 mm)

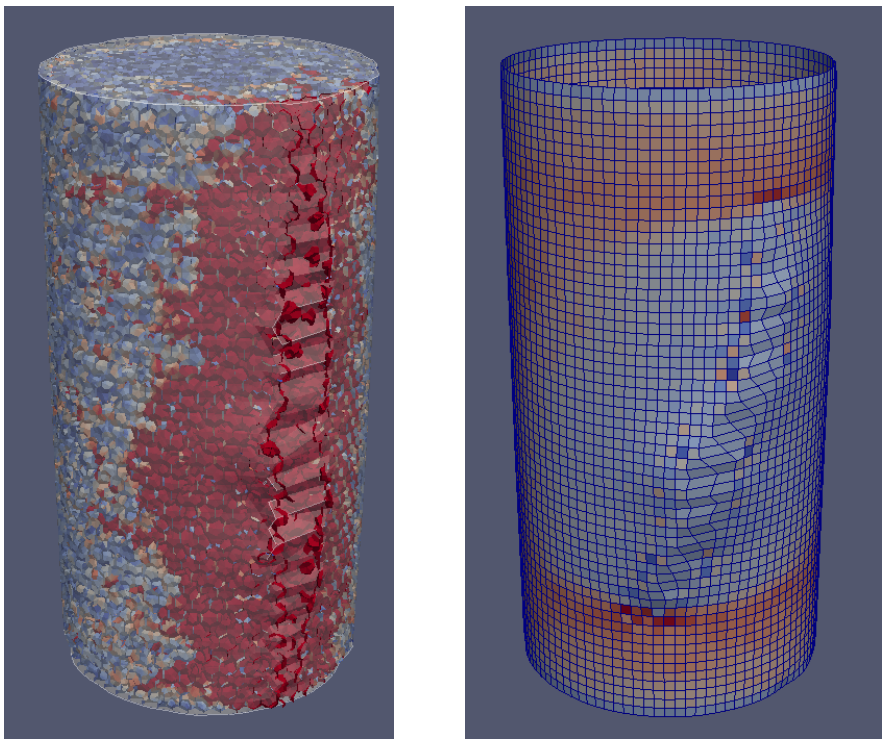

(a) Cracking Patterns in the Concrete Column

(b) Fracture in the FRP jacketing

Figure 3.13: Example of ultimate Condition for FRP confined column (r=75 mm)

3.5.2 Results for columns with smallest corner radius

While the non-uniform confinement pressure and the reduction of confinement effect with the decreasing of the corner radius can be properly simulated, the overall behavior of the columns with the smallest corner radius ($r = 15$ mm and $r = 0$ mm) cannot be well captured still, as shown in figure 3.14, even if the ultimate strength of the FRP material has been taken into account with a stochastic model.

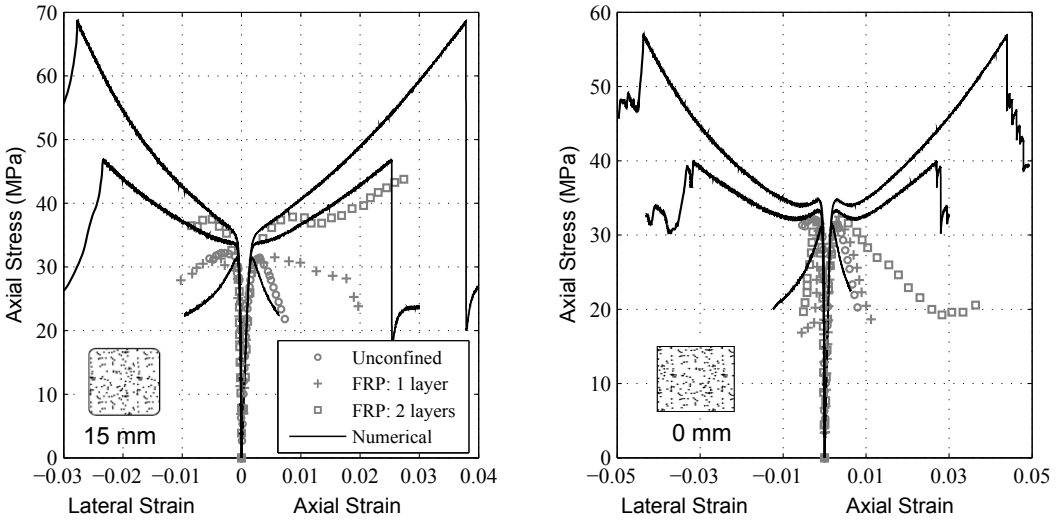

Figure 3.14: Typical stressstrain curves measured in the experiments and predicted by the analysis with non-linear FRP. Squared Corners Set. Full contact

The reasons for the discrepancy between numerical and experimental behavior in case of columns with sharp corners are related to the limitations of the current model and are discussed in this paragraph. Firstly, as previously mentioned in section 3.4, the model cannot take into account the FRP material or geometrical factors related to the fibers or adhesive that lead to the rupture of the composite and, consequently, to the column collapse. In fact, the jacket is modeled with orthotropic shell elements of equivalent thickness $s = 0.165$ mm/layer, which also prevents the capability of capturing any flexural behavior. These aspects become more important with the decreasing of the corner radius and cannot be neglected when the cross section is right-angled, mainly because of the high local stress concentrations and the following local damage accumulation; it should be observed that, in contrast to the standard behavior of FRP confined concrete columns, the experimental stress-strain curves of the FRP confined square-shaped columns are not bilinear but, instead, have a softening tendency after the peak due to the progressive rupture of the jacketing, able to provide, at this point, only ductility and not longer strength. The stochastic approach for the composite strength is not enough to deal with the complexity of

the FRP response.

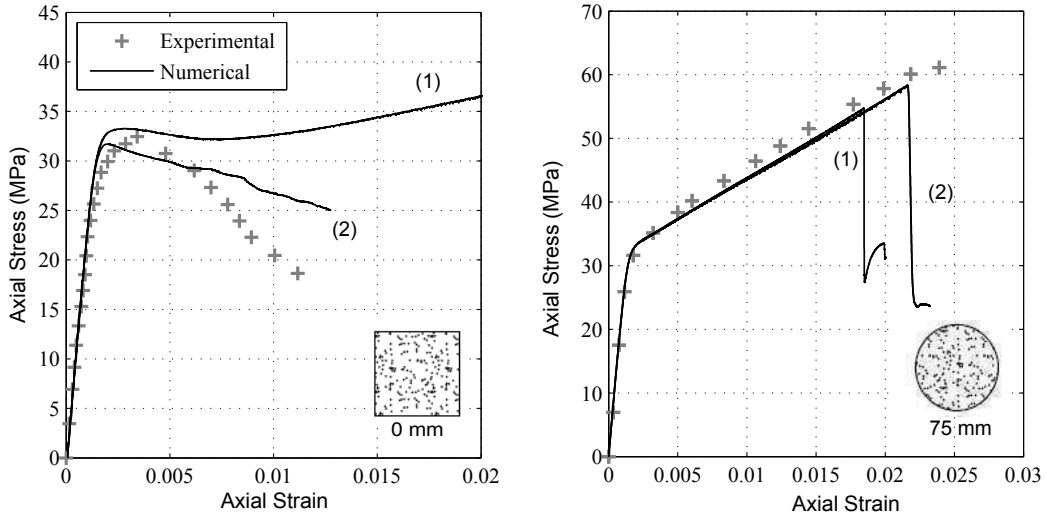

Figure 3.15: Comparison between experimental and numerical stress-strain curves for the square column ($r = 0$ mm) and the circular column ($r = 75$ mm) with 1 FRP ply. (1): normal and tangential contact; (2): normal contact only

Furthermore, another reason for the poor prediction is thought to be related to the modeling of the interaction between FRP and concrete, currently obtained through a master-slave formulation which cannot take into account the debonding processes occurring at the interface. Such failures may significantly decrease the effectiveness of the strengthening [65], especially if the delamination interacts with the local rupture of the composite. Figure 3.15 compares the behavior in terms of axial stress-axial strain response for both the square shaped and the circular shaped specimen with different contact models, as an example. It can be noticed that, in case of $r = 0$ mm, the confinement effect decreases substantially when the tangential interaction between the surfaces is neglected: the numerical curve (2) can be considered a good approximation of the experimental response, being the maximum stress and the ultimate strain correctly predicted; on the contrary, in case of $r = 75$ mm, the response does not change significantly whether the tangential component is taken into account or not, leading to the assumption that the tangential effects become more important with the decreasing of the corner radius. These observations bring to the conclusion that the development of a proper contact algorithm could considerably improve the simulations of sharp corner shaped specimens and this will be the focus of the future research. 3.16 further proves these considerations: the numerical curves obtained with the Full contact algorithm generally overestimate

both the confining effect and the failure of the FRP, while these two features are underestimated when the Normal contact algorithm is adopted. Therefore, to confirm what has been preliminary noticed, a more sophisticated formulation of the FRP-concrete bond is required for sharp cornered columns, to be able to get the delamination mechanisms occurring at the interface.

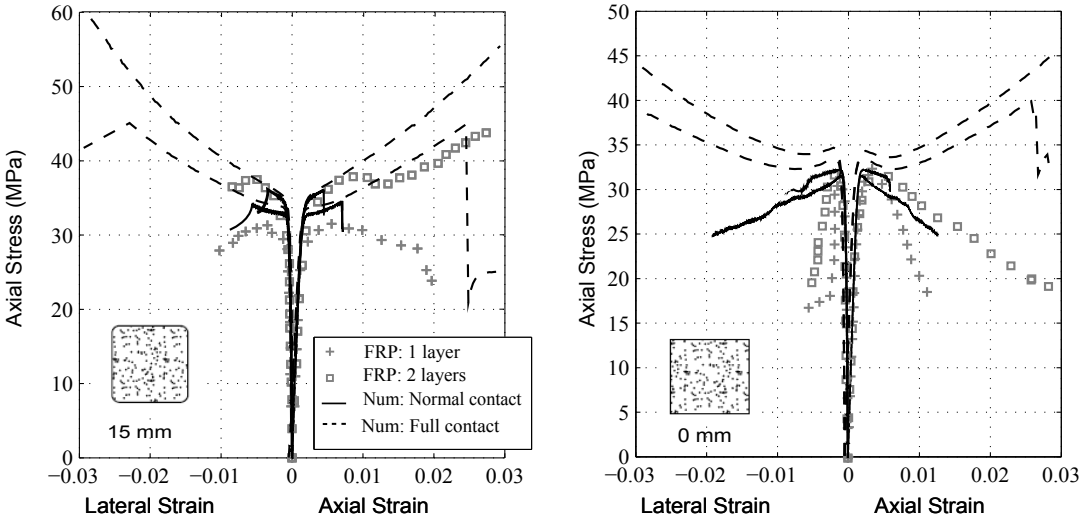

Figure 3.16: Typical stressstrain curves measured in the experiments and predicted by the analysis with non-linear FRP. Squared Corners Set. Normal Contact and Full contact compared

Chapter 4

Proper Orthogonal Decomposition Approach for the Explicit Solution of Large Discrete Systems

4.1 Explicit Integration of the Dynamics Equations of Discrete Systems

As anticipated in Chapter 1, the simulations presented in this research have been performed using the software MARS, which is a powerful and robust object-oriented solver developed for simulating the mechanical response of structural systems subjected to short duration events and it employs an explicit time integration scheme for solving the equation of motion of large systems. For quasi-static events, like the compression tests described in Chapter 3, the application of explicit dynamics may become inconvenient in terms of time analysis, although extremely beneficial as far as convergence is concerned, especially when highly non linear phenomena are involved. In this section, the algorithmic framework for the solution of the Dynamics Equation through a reduced order method is discussed.
Discrete Systems are of particular concern in this study, being focused on the applicability of model reduction techniques to Lattice Discrete Particle Models [24]; more generally, though, the presented algorithm can be applied to any discrete dynamic equilibrium problem solved through explicit integrators such as Discrete Elements Methods (DEM) and Discrete Particle Models (DPM).

4.1.1 Full-Order Integration Algorithm

Let consider the motion governing equation in $\mathbb{R}^n$, a domain which has already been discretized in space:

$$\begin{cases} \mathbf{M}\ddot{\mathbf{u}} + (\mathbf{G}\dot{\mathbf{u}}) + \mathbf{f_{int}}(\mathbf{u}) = \mathbf{f_{ext}} \\ \mathbf{u}(t_0) = \mathbf{u}^\star, \quad \dot{\mathbf{u}}(t_0) = \dot{\mathbf{u}}^\star \end{cases} \tag{4.1}$$

defined $\forall t \in [t_0, t_f]$ and where $\mathbf{M}$ is the mass matrix, $\mathbf{u}$ is the nodal displacements vector, $\mathbf{f_{int}}$ is the internal forces vector, $\mathbf{f_{ext}}$ is the external forces vector; $\mathbf{u}^\star$ and $\dot{\mathbf{u}}^\star$ denote the initial displacements and velocities; Neumann Boundary Conditions are applied in the space domain in the form $\dot{u_i} = \mathbf{v_{0,i}}\ \forall x_i \in \mathcal{B} \subset \mathbb{R}^n$.
The system 4.1 can be discretized in time to be solved numerically; the middle point rule is applied as a time integrator (explicit algorithm):

$$\begin{cases} \ddot{\mathbf{u}}^m = \mathbf{M^{-1}}\left({\mathbf{f_{ext}}}^m - \mathbf{f_{int}}(\mathbf{u}^m)\right) \\ \dot{\mathbf{u}}^{m+1/2} = \dot{\mathbf{u}}^{m-1/2} + \ddot{\mathbf{u}}^m \Delta t \\ \left(\mathbf{u}^{m+1} = \mathbf{u}^m + \dot{\mathbf{u}}^{m+1/2}\Delta t\right) \end{cases} \tag{4.2}$$

being Δt the time step and $m \in [1, n_{steps}]$, $\quad n_{steps} \in \mathbb{N}^*$ the number of the current time step. In elastic regime, the time step Δt must be subjected, because of stability conditions, to the constraint $\Delta t < t_{cr} = 2/\omega_{max}$ where ω_{max} represents the highest natural frequency of the computational system [66]. Belytschko at al. (2000) [67] showed that $\omega_{max} < max(\omega_i)$, where $max(\omega_i)$ are the natural frequencies of each element belonging to the mesh, so the stable time step can be computed solving the eigenvalue problem given by $\det(\mathbf{K} - \omega^2\mathbf{M}) = 0$, where $\mathbf{K}$ is the Stiffness Matrix and $\mathbf{M}$ the Mass Matrix.

4.1.2 Reduced Order Explicit Dynamics through the Proper Orthogonal Decomposition

With the application of Model Reduction Techniques as POD, a low dimensional approximation for the full high dimensional dynamical system, can reproduce the characteristic dynamics of the system itself, reducing the computational costs and storage requirements.

General introduction to POD

As detailed explained by Lianget al. (2001) [68] and many others, the main idea of POD is to find a projection of a vector space $\mathcal{V} \subset \mathbb{R}^n$, where vectors of interest take their values, onto a subspace $\mathcal{S} \subset \mathbb{R}^k$ of fixed dimension $k < n$, containing the best approximation of those vectors. The method, thus, seeks a set of n ordered

orthonormal basis vectors for $\mathcal{V}$ such that the selected first $k < n$ basis vectors generate the optimal orthogonal projection $\mathcal{S} \subset \mathbb{R}^k$ of defined rank k.
The optimal problem can be stated as follows.
Assume that $u \in \mathcal{V} \subset \mathbb{R}^n$ is a random vector and $\{\phi_i\}_{i=1}^n$ is a set of arbitrary orthonormal basis vectors spanning $\mathcal{V}$. Then u can be expressed as a linear combination of these basis vectors through the coefficients d_i, as:

$$u = \sum_{i=1}^{n} d_i \phi_i = \phi d \tag{4.3}$$

where $d = (d_1, d_2, \ldots, d_n)$ and $\Phi = [\phi_1, \phi_2, \ldots, \phi_n]$.

The objective of the POD is to find the set of basis vectors that can span a vector subspace of order k containing the most accurate approximation $\hat{u}(k)$ of the vector u. The following extreme value problem is to be satisfied, using the mean square error as a measure of the optimal problem:

$$\underset{\Phi_i}{min}\, \varepsilon^2(k) = E\left\{\|u - \hat{u}(k)\|^2\right\} \tag{4.4}$$

such that $\phi_i^T \phi_j = \delta_{ij} \qquad i, j = 1, 2, \ldots, n$, where $\hat{u}(k) = \sum_{i=1}^{k} d_i \phi_i \quad (k \leq n)$. These special, orthonormal, basis vectors are called the proper orthogonal modes for u and $\hat{u}(k)$ can be called the POD of u.

Application of POD in a finite dimensional case

As an emerging tool in dynamic analysis, POD is intended as a means of extracting spatial information from a set of time-series data available on a domain. Considering a system of n state variables and capturing, at m instants of time, a set of n simultaneous measurements of these n state variables, data can be arranged in an $n \times m$ matrix U, such that element U_{ij} is the measurement of the i-th state variable taken at the j-th time instant [69]. The final result of the data collection is assumed here to be the $n \times m$ matrix U.

$$\mathbf{U} = \begin{pmatrix} u_1(t_1) & \cdots & u_1(t_m) \\ \vdots & \ddots & \vdots \\ u_n(t_1) & \cdots & u_n(t_m) \end{pmatrix}$$

The Schmidt-Eckart-Young-Mirsky Theorem ([70]) shows the following statement:

- Let define the n-by-n real symmetric matrix $\mathbf{C} = \mathbf{U}\mathbf{U}^{\mathbf{T}}$;
- Let denote by $\hat{\lambda}_1 \geq \hat{\lambda}_2 \cdots \geq \hat{\lambda}_n \geq 0$ the eigenvalues of $\mathbf{C}$ and $\hat{\phi}_i \in \mathbb{R}^n, \quad i = 1, \ldots, n$ their associated eigenvectors such that $\mathbf{C}\hat{\phi}_i = \hat{\lambda}_i \hat{\phi}_i \quad i = 1, \ldots, n$;

- Let assume $\hat{\lambda}_k \geq \hat{\lambda}_{k+1}$.

The subspace optimizing the orthogonal projection of fixed rank k is the invariant subspace of $\mathbf{C}$ associated with the eigenvalues $\hat{\lambda}_1 \dots \hat{\lambda}_k$.
Computationally, the calculation can be carried out computing eigenvalues and eigenvectors directly from the matrix $\mathbf{C} = UU^T$. If $n > m$, though, it is more efficient to compute the eigenvalues and eigenvectors of interest from the matrix $\hat{\mathbf{C}} = U^{\mathrm{T}}U$, being the non-zero eigenvalues of the matrix $\hat{\mathbf{C}} = U^{\mathrm{T}}U \in \mathbb{R}^{m \times m}$ equal to the ones of $\mathbf{C} = UU^{\mathrm{T}} \in \mathbb{R}^{n \times n}$ and standing the following relationship between eigenvectors:

$$\phi_i = \frac{1}{\sqrt{\lambda_i}} U\psi_i, \quad 1, \dots, r = rank(\hat{\mathbf{C}}), \tag{4.5}$$

where $\psi_i \quad 1, \dots, r$ are the eigenvectors of $\hat{\mathbf{C}}$ and $\phi_i \quad 1, \dots, r$ are the eigenvectors of $\mathbf{C}$ ([70]).
In general, however, in numerical applications, the direct computation of the matrix $\mathbf{C}$ as well as $\hat{\mathbf{C}}$ are not directly evaluated but the Singular Value Decomposition is applied ([69]). Being the matrix $\mathbf{U} \in \mathbb{R}^{n \times m}$, the singular value decomposition allows it to be rewritten as:

$$\mathbf{U} = \mathbf{B}\mathbf{\Sigma}\mathbf{V}^T \tag{4.6}$$

where the matrix $\mathbf{B} \in \mathbb{R}^{n \times n}$ is an orthogonal matrix $\mathbf{B}^{\mathrm{T}}\mathbf{B} = \mathbf{I_n}$ and its columns are called left singular vectors of $\mathbf{U}$; the matrix $\mathbf{\Sigma} \in \mathbb{R}^{n \times m}$ has diagonal entries $\mathbf{\Sigma}_{ii} = \sigma_i$ satisfying $\sigma_1 \geq \sigma_2 \geq \cdots \geq \sigma_{min(m,n)} \geq 0$ and zero entries elsewhere; the matrix $\mathbf{V} \in \mathbb{R}^{m \times m}$ is an orthogonal matrix $\mathbf{V}^T\mathbf{V} = \mathbf{I_m}$ and its columns are called right singular vectors of $\mathbf{U}$. In particular, $\{\sigma_i^2\}_{i=1}^{min(m,n)}$ are the eigenvalues of the symmetric matrices $\mathbf{U}\mathbf{U}^{\mathrm{T}}$ and $\mathbf{U}^{\mathrm{T}}\mathbf{U}$ and the columns of $\mathbf{B}$ are the associated eigenvectors of $\mathbf{U}\mathbf{U}^{\mathrm{T}}$

$$\Phi_i = B_i\lambda_i = \sigma_i \tag{4.7}$$

The distribution of the state variables of interest is sampled from the full model for each node and various time. These samples are called snapshots of the full model and are used in an interpolation scheme to approximate the full model. The act of interpolating, in fact, is equivalent to considering only a subspace of the vector space where the full-model solution resides. This subspace is evaluated so that it captures the majority of the variation in the model solution. The entire model is then projected onto this subspace and solved, resulting in a fast approximate solution to the original model.

Reduced Order Integration Algorithm

The Proper Orthogonal Decomposition technique, as described in 4.1.2 can be applied to the full-order integration algorithm described in (4.2).

Let consider, a n-by-N_{snap} matrix U, such that each element u_{ij} is the value of displacement in the i-th node taken at the j-th time snapshot and define the n-by-n real symmetric matrix $\mathbf{C} = \mathbf{U}\mathbf{U}^{\mathbf{T}}$.
The first $k < n$ eigenvalues $\mathbf{B_k} = [\phi_1 \dots \phi_k]$ and the corresponding eigenvectors $\lambda = [\lambda_1 \dots \lambda_k]$ of the matrix $\mathbf{C}$ can be computed. $\mathbf{B_k}$ is the projection matrix, such that $\mathbf{B_k}^{\mathrm{T}}\mathbf{B_k} = I$.

If the selected snapshots are representative enough, the following equivalence holds:

$$\mathbf{u} \approx \sum_{i=1}^{k} d_i \phi_i = \mathbf{B_k}\mathbf{d}; \tag{4.8}$$

therefore, (4.1) can be projected onto $\mathbb{R}^k$ through $\mathbf{B_k}$.
The equation of motion (4.1) can be re-written as a function of d_i, through (4.8):

$$\mathbf{M}\mathbf{B_k}\ddot{\mathbf{d}} + \mathbf{G}\mathbf{B_k}\dot{\mathbf{d}} + \mathbf{f_{int}}\left(\mathbf{B_k}\mathbf{d}\right) = \mathbf{f_{ext}} \tag{4.9}$$

Premultiplying both equation members by $\mathbf{B_k}^{\mathrm{T}}$ the following equation holds, which is the projection of eq.(4.1) onto the subspace generated by $\mathbf{B_k}$:

$$\mathbf{B_k}^{\mathrm{T}}\mathbf{M}\mathbf{B_k}\ddot{\mathbf{d}} + \left(\mathbf{B_k}^{\mathrm{T}}\mathbf{G}\mathbf{B_k}\dot{\mathbf{d}}\right) + \mathbf{B_k}^{\mathrm{T}}\mathbf{f_{int}} = \mathbf{B_k}^{\mathrm{T}}\mathbf{f_{ext}}. \tag{4.10}$$

The equation can be integrated numerically with the middle point rule in the reduced subspace $\mathbb{R}^k$ through the following algorithm:

$$\begin{cases} \ddot{\mathbf{d}}^m = \left(\mathbf{B}^{\mathrm{T}}\mathbf{M}\mathbf{B}\right)^{-1}\left(\mathbf{f_{ext}}^m - \mathbf{f_{int}}\right) \\ \dot{\mathbf{d}}^{m+1/2} = \dot{\mathbf{d}}^{m-1/2} + \ddot{\mathbf{d}}^m \Delta t_r \\ \mathbf{d}^{m+1} = \mathbf{d}^{m-1} + \dot{\mathbf{d}}^{m+1/2}\Delta t_r \end{cases} \tag{4.11}$$

The unknowns are the coefficients d_i with $i = 1, k$, guaranteeing that the linear combination with the $\mathbf{B_k}$ columns is as closer as possible to the real, sought, solution. In each time step, though, the full dimensional displacement $\mathbf{u}$ and the corresponding velocity $\dot{\mathbf{u}}$ are evaluated,from the associated projected values, because the internal forces and the residual forces are computed in the full original domain. The main reason for this choice is to keep the reduced system algorithm as close as possible to the original one, preserving all the explicit algorithm features and allowing an easy transition from one to the other in the snapshot collecting process. In a fully explicit integration algorithm, in fact, the stiffness matrix is not assembled.

The new time step Δt_r must be subjected to a different constrain, $\Delta t_r < t_{r_{cr}} = 2/\omega_{kmax}$, leading to the following eigenvalue problem:

$$\det\left(\mathbf{B_k}^{\mathrm{T}}\mathbf{K}\mathbf{B_k} - \omega_k^2 \mathbf{B_k}^{\mathrm{T}}\mathbf{M}\mathbf{B_k}\right) = 0. \tag{4.12}$$

$\mathbf{B_k}^{\mathrm{T}}\mathbf{K}\mathbf{B_k}$ is the Projection of the Stiffness Matrix in $\mathcal{S} = span\left(\mathbf{B_k}\right) \subset \mathbb{R}^k$ and $\mathbf{B_k}^{\mathrm{T}}\mathbf{K}\mathbf{B_k}$ the Projection of Mass Matrix.

4.1.3 Essential and Natural Boundary Conditions

The Proper Orthogonal Modes, through which the reduced system is computed, will automatically satisfy any fixed boundary conditions in terms of displacements (or velocities) for construction. In fact, the **U** matrix has a 'zero' row corresponding to any fixed degrees of freedom and this information will be transferred to the Proper Orthogonal Modes themselves and, consequently, to any object in the subspace they span.
The non-zero BCs, though, need to be re-applied in the reduced system, these data not being preserved by the Proper Orthogonal Modes. It is not easy however, to apply the BCs directly to the projected degrees of freedom in the reduced subspace, because this would lead to a overdetermined system. To elude the obstacle, the BCs are applied indirectly as equivalent external forces through the penalty method:

$$f_{ext} = K_p \cdot (u_p - u) \tag{4.13}$$

where f_{ext} is the external force equivalent to the BC, K_p is the Penalty coefficient, set around $10^3 - 10^4$ times the stiffness of the elements, u_p is the penalty displacement, whose value comes from the BC (if given in terms of displacement) or from its integration in time (if given in terms of velocities) and u is the current displacement of the node of interest. The Penalty enforcement of the boundary conditions in the reduced order model has been previously explored by Kalashnikova and Barone (2012), [71].
Due to instability issues, the node mass M_{ii} where the penalty constrain is applied is artificially increased (mass scaling) by adding a quantity which is proportional to the penalty coefficient K_p and to the square time step dt :

$$M_{ii} := M_{ii} + 1.1 \cdot Kp \cdot dt^2. \tag{4.14}$$

When the Penalty Method is applied, the computation of the stable time step in the projected system should take into account the increased stiffness due to the penalty constrain.

4.1.4 Mode updating

The snapshots can be computed *a posteriori*, after the end of the regular analysis. This method allows the definition of the reduced system for model validation purposes and the snapshot collection can be the most efficient possible, since the real solution is already known. Aiming to a predictive tool, though, the snapshots should be collected during the analysis itself, *in itinere*, alternating the integration in the complete system, for the snapshots collection, with the integration in the reduced system, until the snapshots previously collected are enough representative of the response. When dealing with quasi static problems, the complete system can

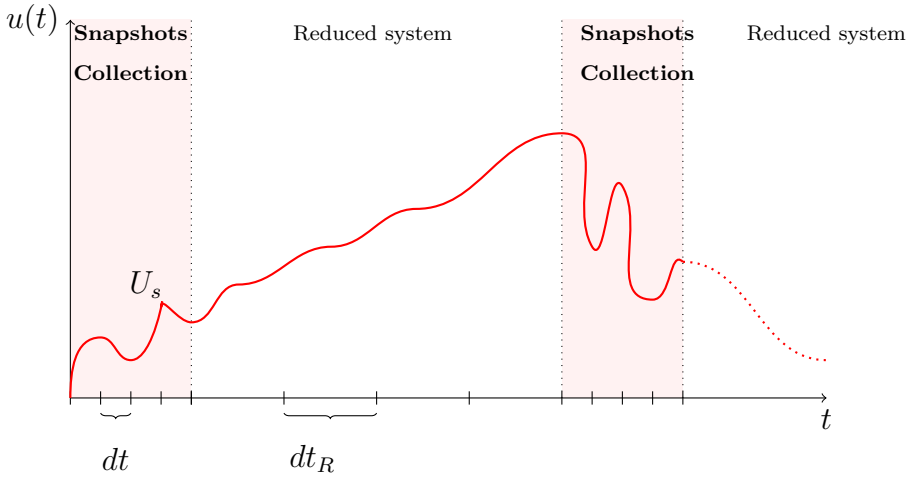

Figure 4.1: Time Step Scheme

be integrated only for a small initial time interval ΔT, just to capture an adequate number of snapshots, which sufficiently describe the system behavior. The corresponding reduced system can, then, be computed from the first k Proper Orthogonal Modes and the analysis carried out in the reduced system with a greater time step. Obviously, the snapshots may need to be updated to take account of any variation of the external (for instance in case of changes in applied forces, displacements, velocities) or internal conditions (for instance changes due to the constitutive law). So, after a time interval ΔT_{R}, when the old snapshots are not any more representative, the analysis could be carried out back through the complete system to recompute a new group of snapshots... and so on. The amplitude of ΔT and ΔT_{R} can be fixed and different ratios of them have been related to the accuracy of results.
Once the first snapshots have been collected and the corresponding reduced space defined, the integration in the reduced system can start, using as initial condition for the integration the following values, where $\dot{\mathbf{u}}$ and $\mathbf{u}$ are the values of velocity and displacement given by the last time step integration in the complete system:

$$\dot{\mathbf{d}} = \mathbf{B}^{\mathrm{T}}\dot{\mathbf{u}}; \qquad \mathbf{d} = \mathbf{B}^{\mathrm{T}}\mathbf{u}. \tag{4.15}$$

As already explained, the stable time step in the reduced system is higher than the one in the complete system $dtR > dt$. To allow a proper translation from one integration scheme (4.2) to the other (4.11), an appropriate time step definition is set for the first and the last time step in the reduced system: in the velocities integration, the time step results as $dtV = \frac{1}{2}(dtR + dt)$ in both the very first and very last time step of the reduced space integration, while in the displacements integration $dtD = dtR$ for the first time step and $dtD = dt$ for the last one before the updating process.

In particular, when the integration shifts from the fully explicit method to the reduced space method, the velocities and the corresponding displacement in the full order space are computed as shown in equation:

$$\dot{\mathbf{u}}_k = \frac{1}{dtD}\left(\mathbf{B}\mathbf{d}_k - \mathbf{u}_{k-1}\right); \qquad \mathbf{u}_k = \cdot\mathbf{u}_k dtD \tag{4.16}$$

Note that the term $\mathbf{u}_{k-1}$ comes from the fully explicit integration.
A possible improvement of the method could be the development of an adaptive algorithm, able to automatically update the POD modes and consequently the subspace of the reduced system.

4.2 One-Dimensional Implementation and Analysis

4.2.1 System Description

In order to explore the potential applicability of the POD to dynamical problems and to understand how this technique may be used to extract qualitative and quantitative information about the spatial structure of large mechanical systems, a simple one-dimensional benchmark example, made of trusses elements, has been tested. As shown in figure 4.2, it can be considered as a simple discrete system, in which a number n of masses $m_i = \rho A_i l$ are connected to each others (and to a wall at one end) by linear springs of assigned stiffness $k_i = EA_i/l$. An imposed constant velocity v_0 is applied to the last node.

For the benchmark study, the geometrical and mechanical parameters are the following: $L = \sum_i l_i = 10$ cm, $A = 5$ cm^2, $E = 30000$ MPa, $\rho = 2500\ Kg/m^3$. The values are chosen according to the concrete material characteristics and the typical concrete specimens dimensions.

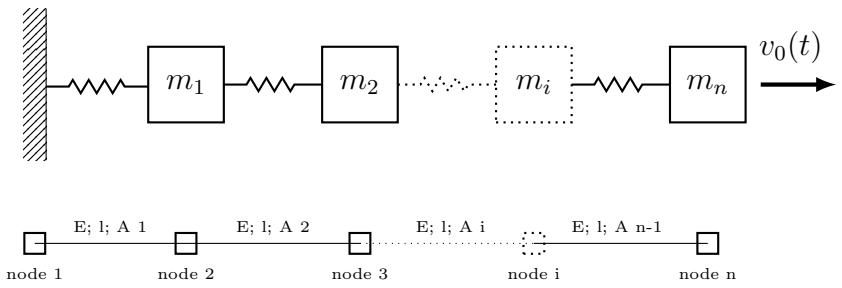

Figure 4.2: Simple model of a dynamic system of trusses

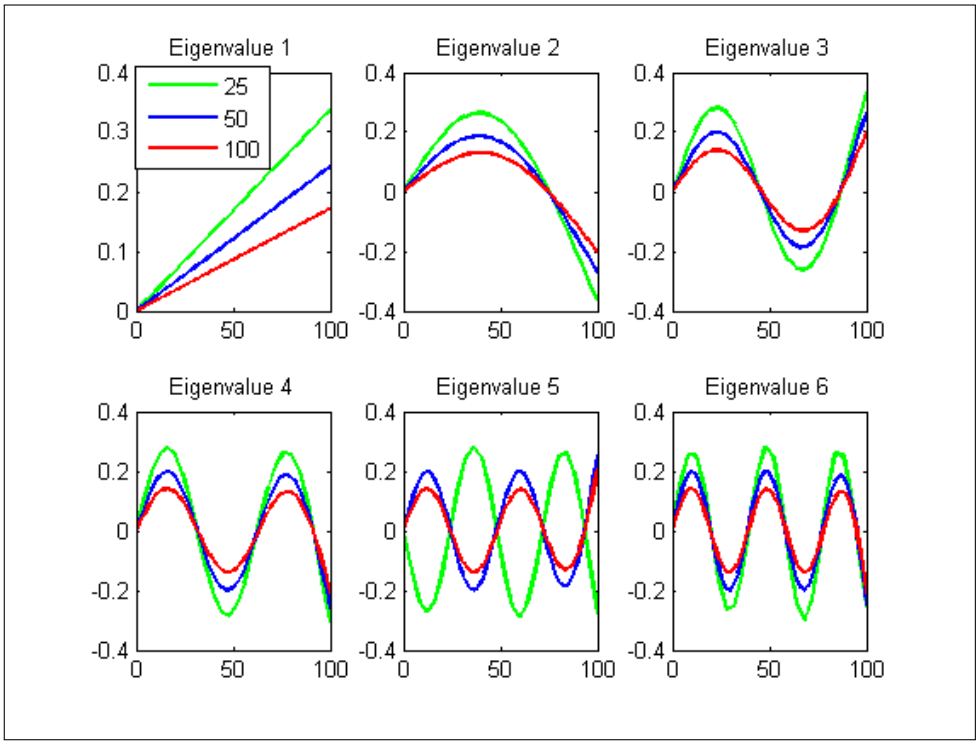

Figure 4.3: Shape of the first Proper Orthogonal Modes

4.2.2 Linear Elastic Material

Initially, the analysis has been focused on the system represented in figure (4.2), assuming a linear elastic material (and consequently a linear elastic response). The simplest case, in fact, provides the first overview of the technique operation and allows a general comprehension of the problem.
Different numbers of elements have been considered for the same problem, to evaluate how the efficiency of the Proper Orthogonal Decomposition, in terms of computational gain, varies with the number of degrees of freedom. Understanding how the dimension of the projected system affects the goodness of the approximation and the minimum time step required for the stability are the main goals of this section.

To begin, a 25 elements system has been considered and then more tests have been carried out for a 50 elements system, a 100 elements system and, finally, a 200 elements system; for each of them, the algorithm described in 4.2 (fully explicit solution) has been used, referring to a total time $t_{\text{tot}} = 0.01s$. The velocity applied to the last node has been imposed equal to $v_0 = 10mm/s$. Then, the Proper Orthogonal Decomposition Technique has been applied , as following:

1. The fully explicit algorithm (4.2) runs, with dt time step for a time interval of

about $2 \cdot 10^{-4}$ s, which is 2% of the total time analysis;

2. 20 Equally Spaced Snapshots of the solution are collected from that time interval, ;

3. The subspace of k dimension is computed;

4. The reduced-space algorithm (4.11) runs until the end of the analysis, with a $dt_R > dt$ time step.

4.2.3 About the Subspace Dimension

The fully explicit algorithm runs for a number of time steps high enough to allow a representative snapshots collection from the displacements of the real solution, through which the projected subspace is computed with the Proper Orthogonal Modes. As already explained in par. 4.1.2, the Proper Orthogonal Modes are the eigenvectors associated with the eigenvalues of the matrix $C = U \cdot U^{\mathrm{T}}$: the higher the eigenvalue, the more representative of the response the associated eigenvector, the smaller the Projected Subspace Dimension, the more advantageous the Proper Orthogonal Decomposition Application, since only few modes would be representative enough. Figure 4.3 shows the course of the first 6 eigenvectors along the beam lenght and evidences that the shape of the Proper Orthogonal Modes is independent from the number of degrees of freedom, deriving from the geometry of the problem.

As far as the Linear Elastic Material is concerned, the analysis shows that the first mode itself can be enough to represent the response of the system in terms of displacements, forces and energy: it accounts for more than 99.9% of the total sum of all eigenvalues, independently of the number of degrees of freedom of the original problem. The first Proper Orthogonal Mode is in the form of a straight line, which can be considered as the static response of the system, while the following modes take account for the vibrations due to the dynamical effects.

There is no necessity to collect the snapshots every time step. In fact, it can be shown that the shape of the first eigenvector of the 50 element truss does not change whether the snapshots are being collected every time step or at different time intervals. In addition, in the linear elastic case study, the snapshots do not need to be updated during the analysis because the system response does not change.

For that reason, only 20 snapshots are collected once from the global analysis. The stable time step in the reduced system dtR increases with the number of degrees of freedom and so the so called PIF, performance improvement factor [31]. PIF is defined as the ratio between the total CPU time of a fully explicit algorithm with the critical time step (T_{cd}) and the total CPU time of the POD algorithm, including the snapshots collection and the SVD computation. It should be noticed that the stable time step during the reduced integration dtR is also a function of the chosen

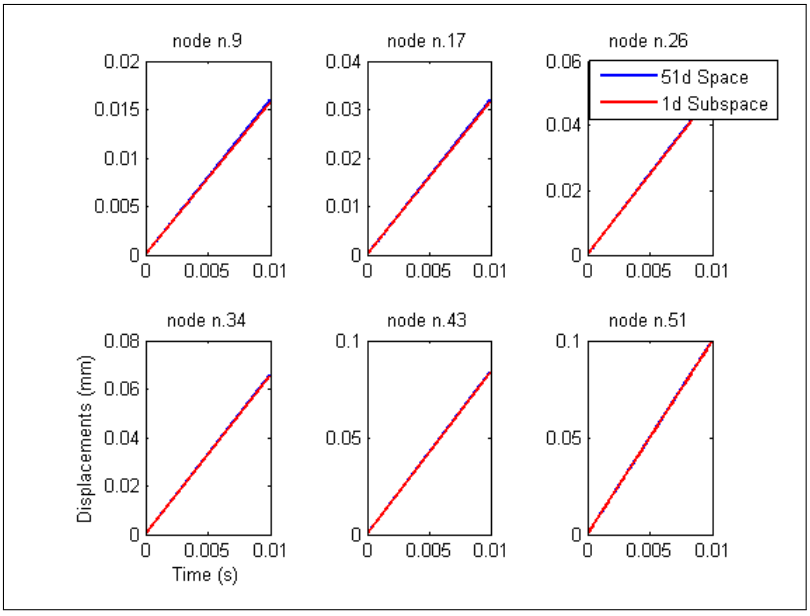

Figure 4.4: Displacements in time for selected nodes (50 elements)

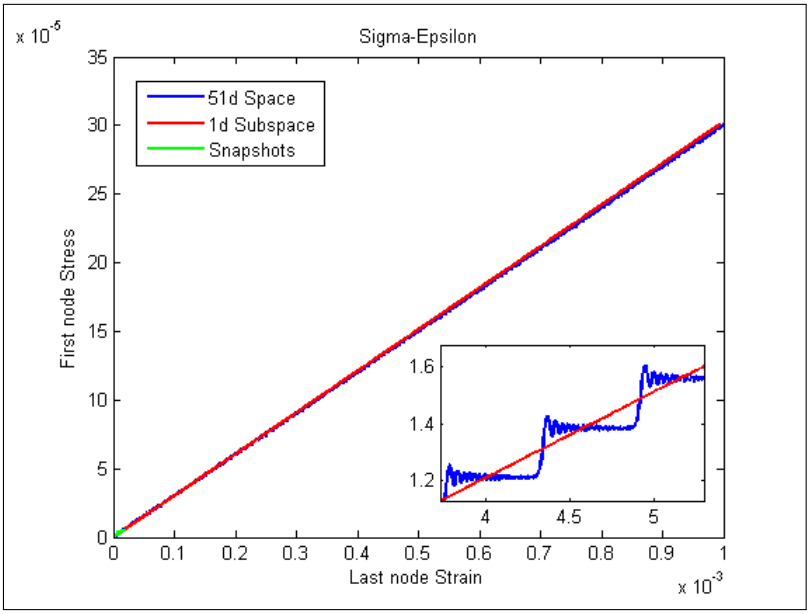

Figure 4.5: First Node Stress - Last Node Strain (50 elements)

DoF	dtR/dt	PIF	$\mathbf{e_n}$
25	2.4	3.2	1.6%
50	4.5	7.5	0.2%
100	11.6	15.5	0.9%
200	32.4	34.6	2.0%

Table 4.1: POD results for Linear Elastic Material

penalty stiffness K_p, when the penalty method is applied: the higher the coefficient, the smaller the stable time step (and so the performance index factor) but the more accurate the results. With $K_p = 10^4$, results are showed in table 4.1.

$$PIF = \frac{T_{\text{cd}}}{T_{\text{ms}}} \tag{4.17}$$

The error between the fully explicit algorithm and the POD application is evaluated as the global error in Energy at the end of the analysis. The error $\mathbf{e_n}$ is evaluated as:

$$E_n = E_{n-1} + \left(\frac{fe_{1,n} - fe_{1,n-1}}{2} + fe_{1,n} \right) \cdot (u_{N,n} - u_{N,n-1}) \tag{4.18}$$

$$E_n^* = E_{n-1}^* + \left(\frac{fe_{1,n}^* - fe_{1,n-1}^*}{2} + fe_{1,n}^* \right) \cdot \left(u_{N,n}^* - u_{N,n-1}^* \right) \tag{4.19}$$

$$e_n = \sqrt{\frac{\left(E_n^* - E_n\right)^2}{{E_n}^2}} \tag{4.20}$$

where E_n and E_{n-1} are the Energy at time t_n and time t_{n-1} for the fully explicit algorithm while E_n^* and E_{n-1}^* are Energy at time t_n and time t_{n-1} for the POD algorithm; $fe_{1,n}$ and $fe_{1,n-1}$ are the internal forces in the first element at time t_n and time t_{n-1} for the fully explicit algorithm while $fe_{1,n}^*$ and $fe_{1,n-1}^*$ are the internal forces in the first element at time t_n and time t_{n-1} for the POD algorithm; $u_{N,n}$ and $u_{N,n-1}$ are the last node displacements at time t_n and time t_{n-1} for the fully explicit algorithm while $u_{N,n}^*$ $u_{N,n-1}^*$ are the last node displacements at time t_n and time t_{n-1} for the POD algorithm.

The results show that the first mode is enough to represent the response of the system independently from the number of degrees of freedom of the system and the gain in terms of increased time step is increasing as the dimension of the elements decreases and the number of degrees of freedom increases. For each node, during the whole time history, the displacements are perfectly caught by the POD algorithm (as shown in fig (4.4)).

Figure 4.5 demonstrates, with a comparison between the fully explicit algorithm results and the POD algorithm results, the agreement in terms of stress-strain curve.

The first node stress is plotted against the last node displacement: the curves are essentially overlapped.

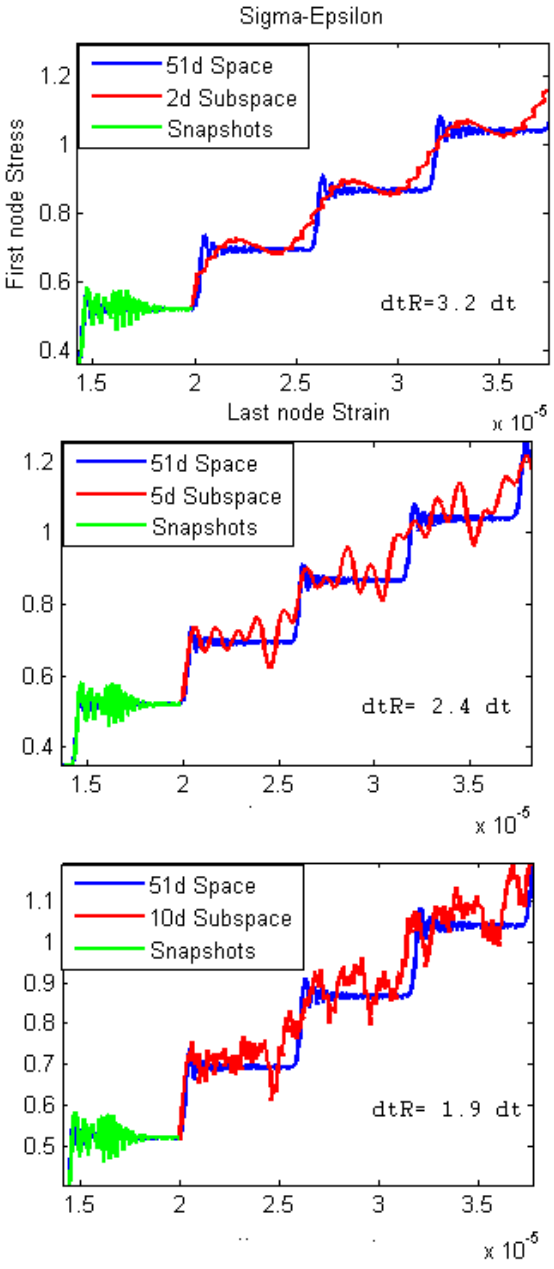

Figure 4.6: Reduced System Responses with different numbers of Modes.

It is of interest to notice that the 1st Mode describes the system behavior in average, through the shape of the eigenvector itself (a straight line) filtering all the small vibrations. Obviously, the higher number of modes considered by POD, the greater the subspace where the integration takes place and, thereby, the closer the projected subspace to the full space containing the real solution. So, as more modes are included in the Subspace definition, the POD system is capable of represent a higher number of details.

On the other hand, though, the stable time step of the analysis becomes smaller because the POD subspace is enlarging and getting closer to the full space. Figure 4.6 illustrates this behavior, referring to the 50 elements system: by adding the second mode, the solution is able to represent some vibrations in the response and the following modes allow the approximate solution to include some vibrations, until the numbers of modes is equal to the numbers of degrees of freedom of the problem so the POD solution and the real solution coincide. The counterpart is the rapid decreasing of the stable time step. The goal of the POD application for quasi static problems is to obtain an approximate solution capable of representing the macro behavior, filtering the particles' vibrations, with the highest time step possible. The Proper Orthogonal Modes can be interpreted as shape functions with global support: if the eigenvectors are properly normalized, imposing them to be equal to zero in correspondence to an

assigned node, then the coefficients of the linear combination, been used for the integration of the reduced system, can be considered the displacement portion associated to that Mode.

4.2.4 Softening Material

The studies and results related to Linear Elastic Materials have to be intended as a preliminary step towards the application of the Proper Orthogonal Decomposition technique to nonlinear problems, in which localized deformations occur, aiming in fact to a relevant tool for concrete and quasi brittle materials.
The same geometry, material parameters and BCs described in section 4.2 are considered, except that a fracturing behavior has been introduced when a limiting stress boundary is reached: the concrete material constitutive equations are reproduced, following the formulation proposed by Cusatis et al.(2011) [24]. In order for the fracture process to be realistically activated, one element (the central one) has been considered weaker than the others, assigning a smaller tensile strength ($\sigma_T = 3$MPa for a regular element, $\sigma_T = 2.5$ MPa for the central element). This mechanical characterization leads to a softening branch in the stress-strain curve, which means a discontinuity in the response. As long as the tensile stress in each element is smaller

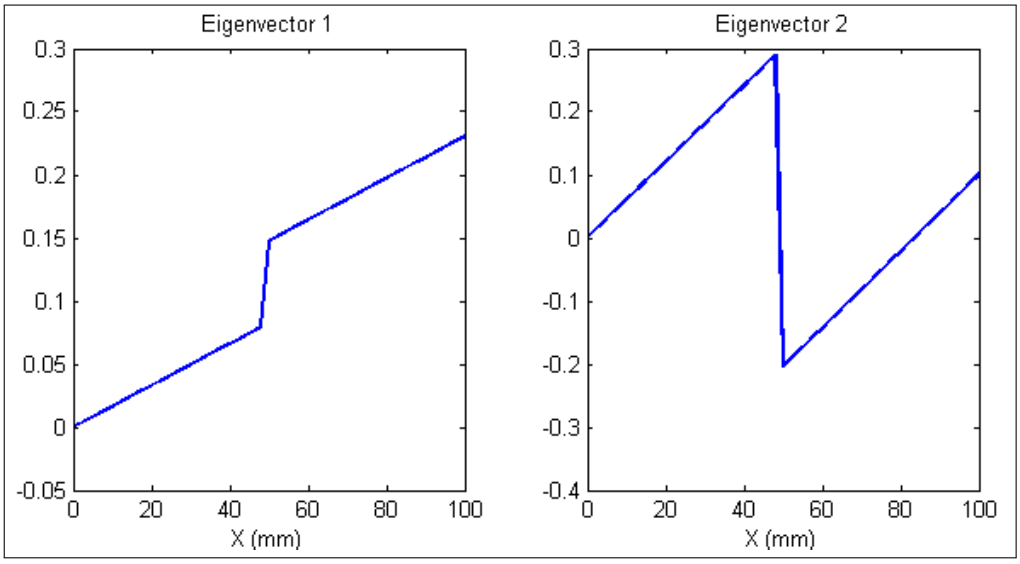

Figure 4.7: Response with snapshots update

than the tensile strength, the behavior of the system is linear elastic and what has been observed for the elastic material, in the previous section, identically holds: the First Proper Orthogonal Mode can describe the average response of the system. When the tensile strength of the weaker element is reached, though, the softening

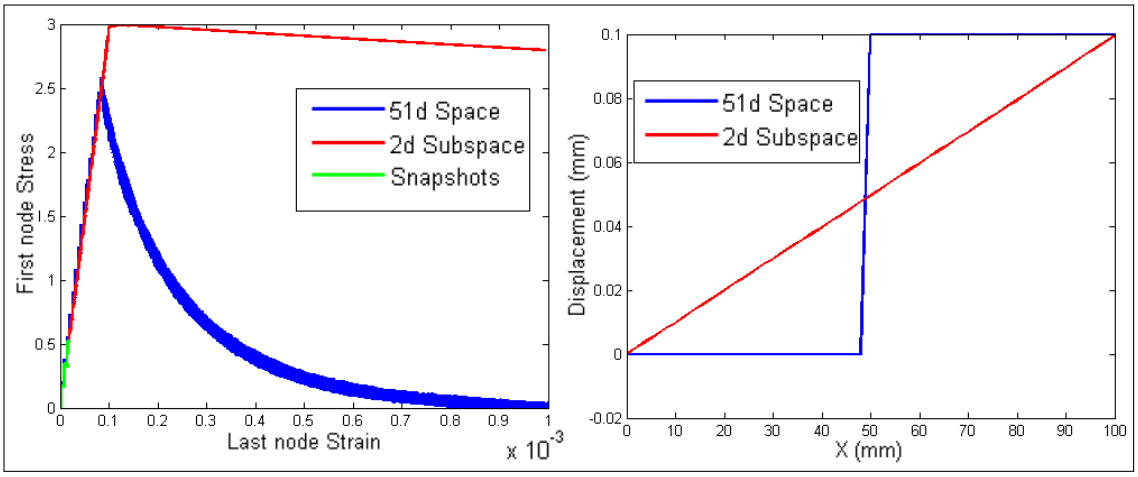

Figure 4.8: Response without snapshots update (50 elements)

mechanisms are activated and the fracture process starts. The old subspace, originated from the snapshots collected at the beginning of the linear elastic analysis, can not represent the real solution any more, as figure (4.8) illustrates: a new adequate subspace should be sought in order for the POD algorithm to continue.

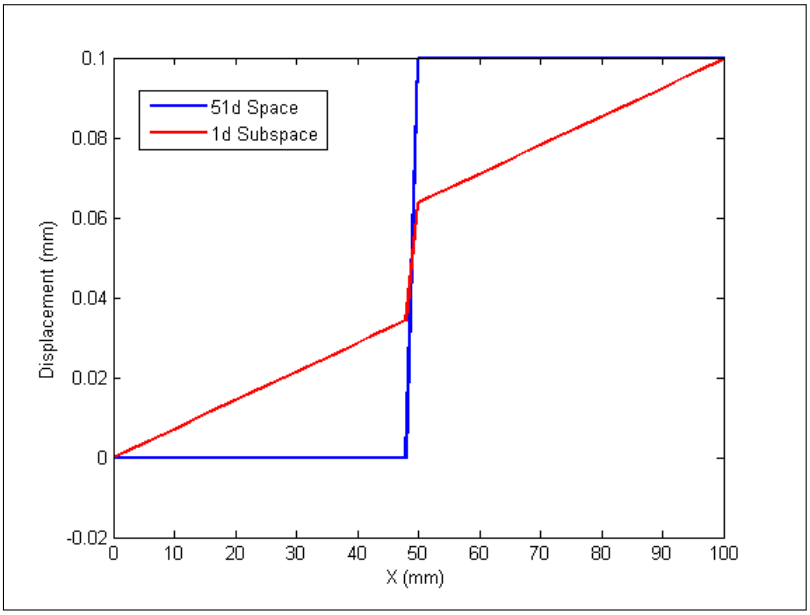

Figure 4.9: Displacements distributions along the truss using only the 1st Mode (50 elements)

The POD algorithm, therefore, has to switch again to the fully explicit integration just before the maximum tensile stress is reached, to calculate the new snapshots

and, from them, the new proper orthogonal subspace.

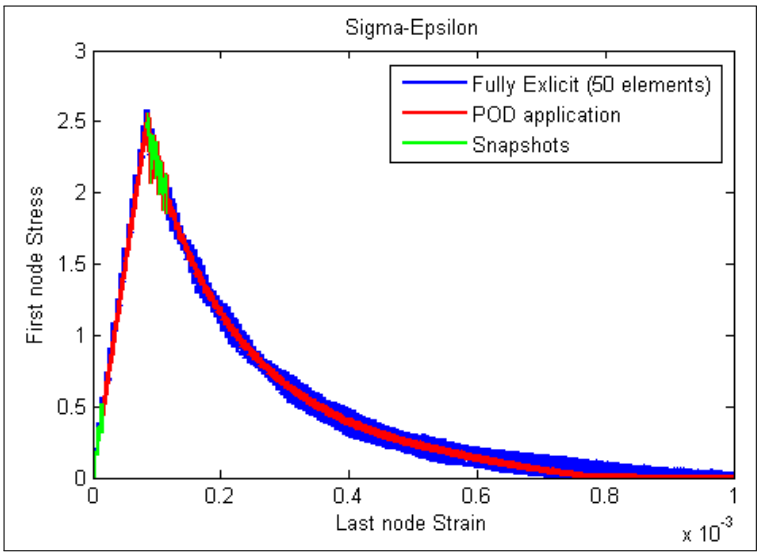

Figure 4.10: Stress-Strain Curve using two Proper Orthogonal Modes (50 elements)

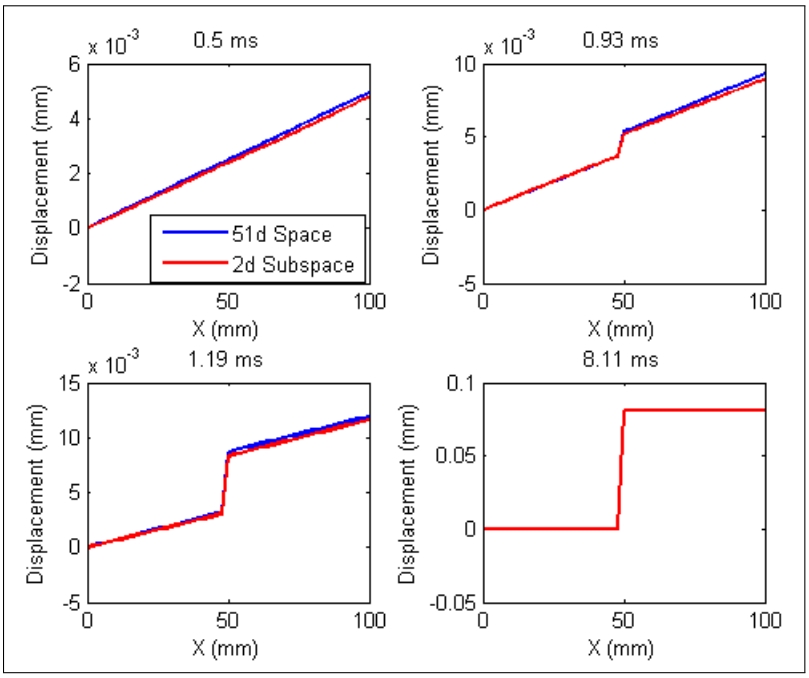

Figure 4.11: Displacements distributions along the truss, in selected time snapshots (50 elements)

At least 2 Modes (figure 4.10) are required to reproduce the softening branch in the reduced integration. For the 50 elements system, with a penalty stiffness

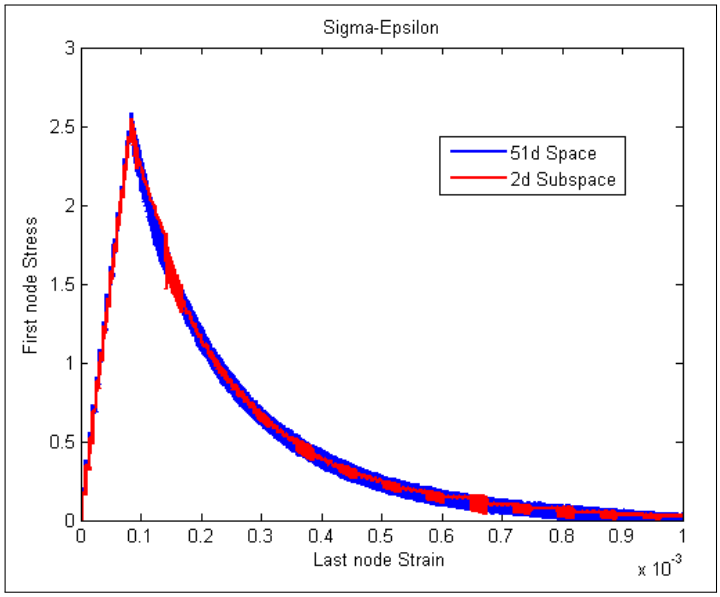

Figure 4.12: First Elements Stress- Last Element Strain Curves in case of automatic update (50 elements)

set $Kp = 10^3$, the stable time step after the re-computation results to be equal to $dtR = 3.9dt$ and the index of performance is $PIF = 7.7$. For the 100 elements system the stable time step after the re-computation results to be equal to $dtR = 5.6\,dt$ and the index of performance is $PIF = 11.5$ (the efficiency of the algorithm is still increasing with the number of degrees of freedom.)

The shape of the first and second Proper Orthogonal modes are directly correlated with the displacements trend along the truss length and a combination of the them is necessary and sufficient to reproduce the real pattern (figure 4.11). The single 1st Mode is not sufficient as figure (4.11) allows to understand. The aforementioned method can not obviously be applied if the material behavior is a priori unknown. In this case, it is possible to automatically update the snapshots switching to the fully explicit algorithm after a predetermined time interval. The more often the snapshots are updated, the more accurate could be the approximate solution, but the less the computational gain. In case of the 50 elements system, setting the time interval for the fully explict algorithm to run and the snapshots to be collected equal to $\Delta T = 0.25ms$ and the time interval for the reduced integration in a 2d subspace equal to $\Delta T_{\mathrm{R}} = 0.58ms$ ($dtR = 5dt$), an error in energy less than 3% can be achieved in the softening branch (figure 4.12) with a performance index factor equal to $PIF = 2.5$.

4.2.5 Unloading Reloading

The Proper Orthogonal Modes computed when the softening response starts and capable of representing the softening branch can represent the whole curve as well. Using the same subspace, any unloading reloading behavior can be reproduced, with no need of switching to the complete system in order to update the snapshots. The case of 50 elements is reported in figure 4.13 where the estimated computational gain in terms of Cpu performance is $PIF = 5$.

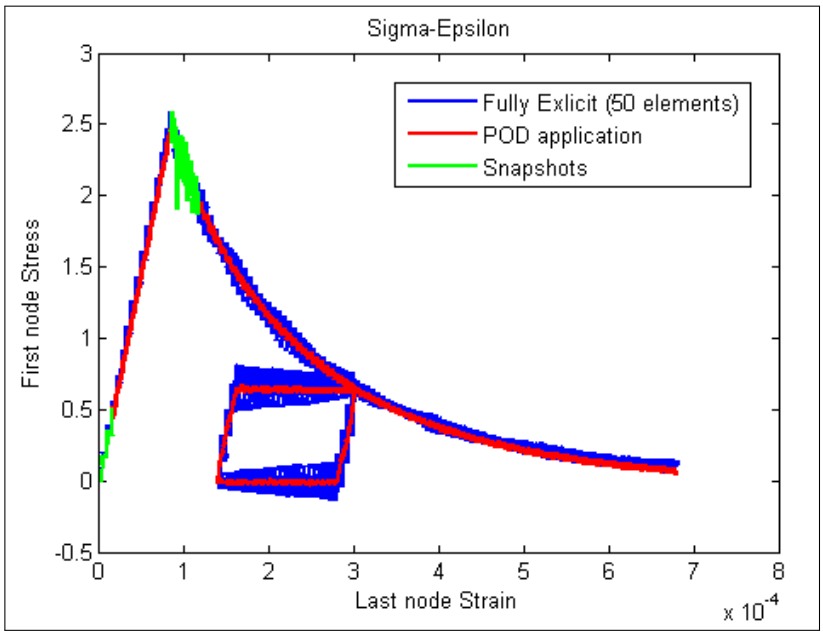

Figure 4.13: First Elements Stress- Last Element Strain Curves in case of unloading-reloading (50 elements)

4.2.6 Mass Scaling within POD

A further improvement of the reduced system efficiency in terms of computational gain would be the use of a Mass Scaling Technique together with the Proper Orthogonal Decomposition. Applying the Mass Scaling only during the reduced integration, the Snapshot computation remains unchanged and so the Proper Orthogonal Modes, while the critical time step dtR in the corresponding subspace is allowed to increase arbitrarily large. Obviously accuracy considerations are required in order to obtain satisfactory results.
The mass scaling is applied to the original full scale mass matrix just before it is projected to the low dimensional subspace. The modified mass matrix $\widetilde{\mathbf{M}}$ is computed according to the method proposed by Heinstein et al. (1996) and described by DeFrias et al.(2014):

$$\widetilde{\mathbf{M}} = \alpha \mathbf{M} \tag{4.21}$$

$$\alpha_i = \frac{dtR^2}{4} \frac{\overline{K}_i}{M_i} \tag{4.22}$$

where M_i is the element lumped mass at node i, $\overline{K}_i$ the element nodal stiffness and dtR a user-defined time step.

The modified mass matrix is then projected through the proper orthogonal Modes $\mathbf{B}^{\mathrm{T}}\widetilde{\mathbf{M}}\mathbf{B}$ and used for the reduced integration in the POD algorithm.
A considerable improvement can be observed in terms of efficiency combining proper orthogonal decomposition and mass scaling. In fact, the combination of both methods allows a optimum compromise between accuracy and increased time step. As far as the elastic material is concerned, in figures 4.14 and 4.15, it is highlighted the improved efficiency of the mass scaling technique when coupled with the proper orthogonal decomposition: the mass scaling technique alone is not accurate enough when the increased time step dt_{R} is much bigger than the standard time step, because the increased mass causes the development of high inertial forces . When the mass scaling is combined with POD, though, this effect is much smoother being only the first mode considered.
It has been observed that, in this case, the stress-strain curve remains overlapped to the original full scale response independently from the time step dimension, which means that a single step in the reduced system would lead immediately to the end of the analysis. In terms of displacements in time, there are some fluctuations of the response due to the additional mass, which is a function of dt_{R} and so increases with it, but the distorsions can be considered acceptable in terms of accuracy until considerably large time steps (as shown in figure 4.16).

Mass Scaling can improve the results for the Softening Material as well: the critical time step increases and the accuracy of the results rather than the stability controls the choice of dt_{R}.

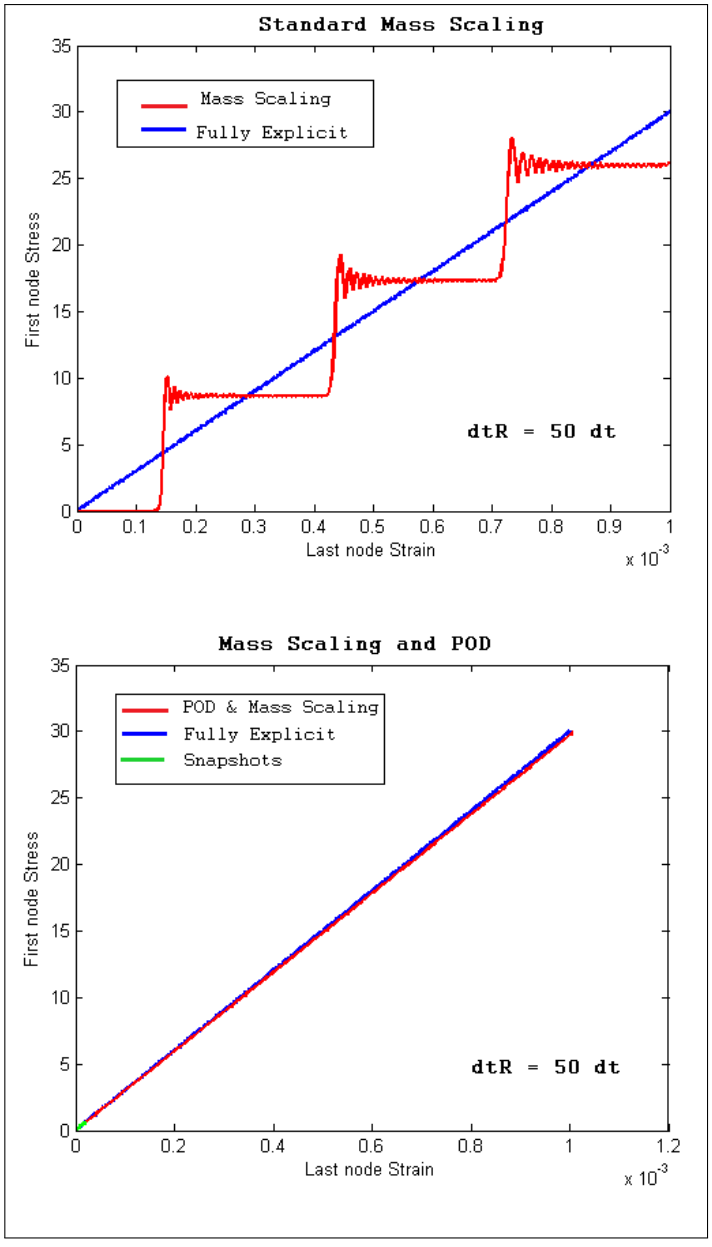

Figure 4.14: First Node Stress-Last Node Strain for 50 elements, linear elastic material: comparison 1

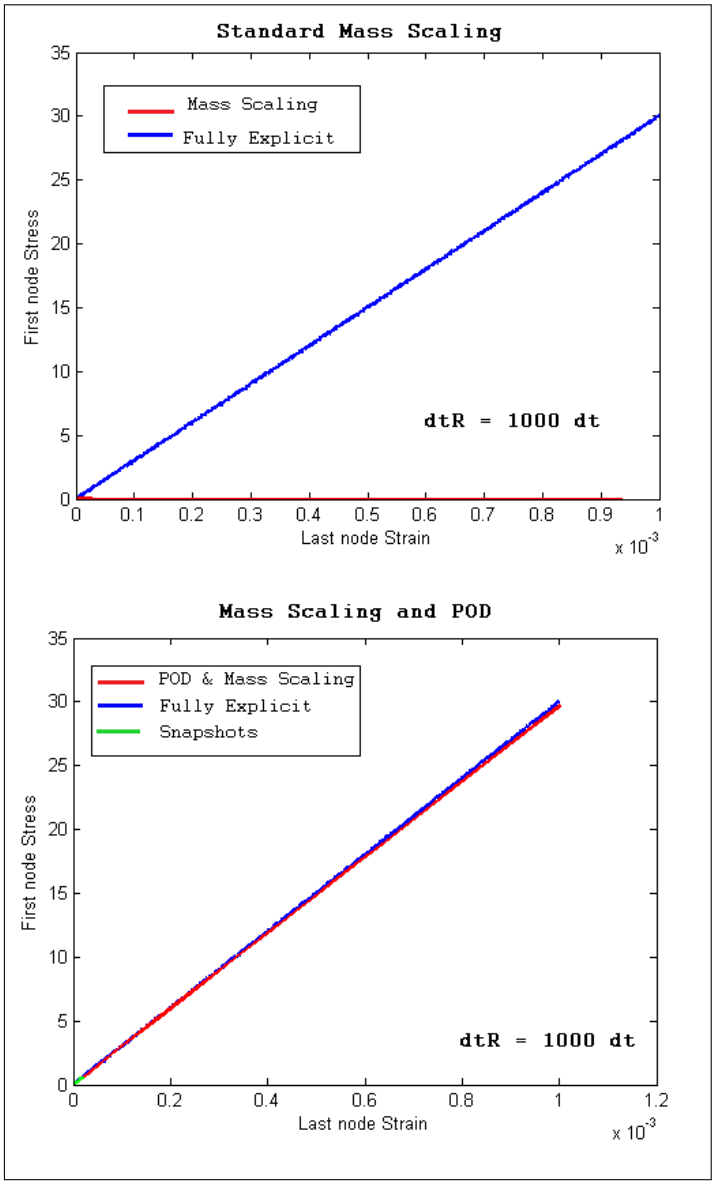

Figure 4.15: First Node Stress-Last Node Strain for 50 elements, linear elastic material: comparison 2

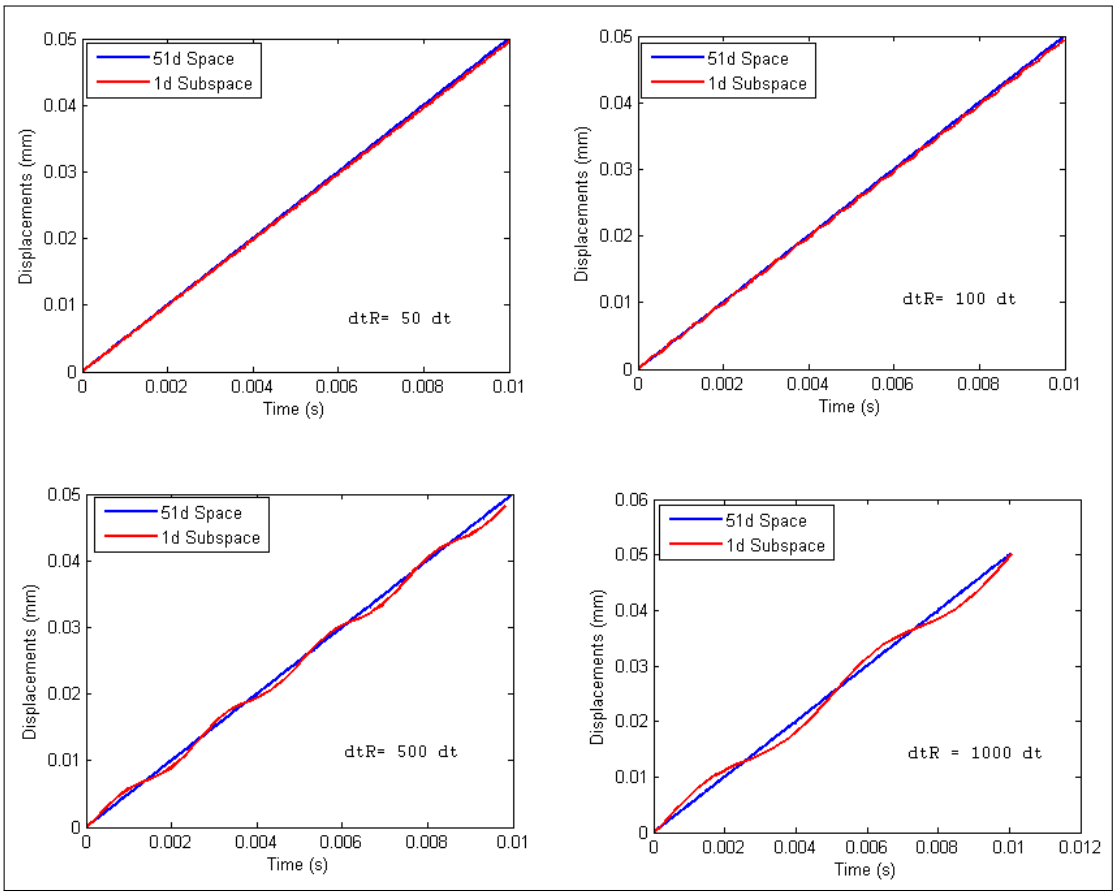

Figure 4.16: Displacements in time for the central node (50 elements system) with different time steps dt_{R}

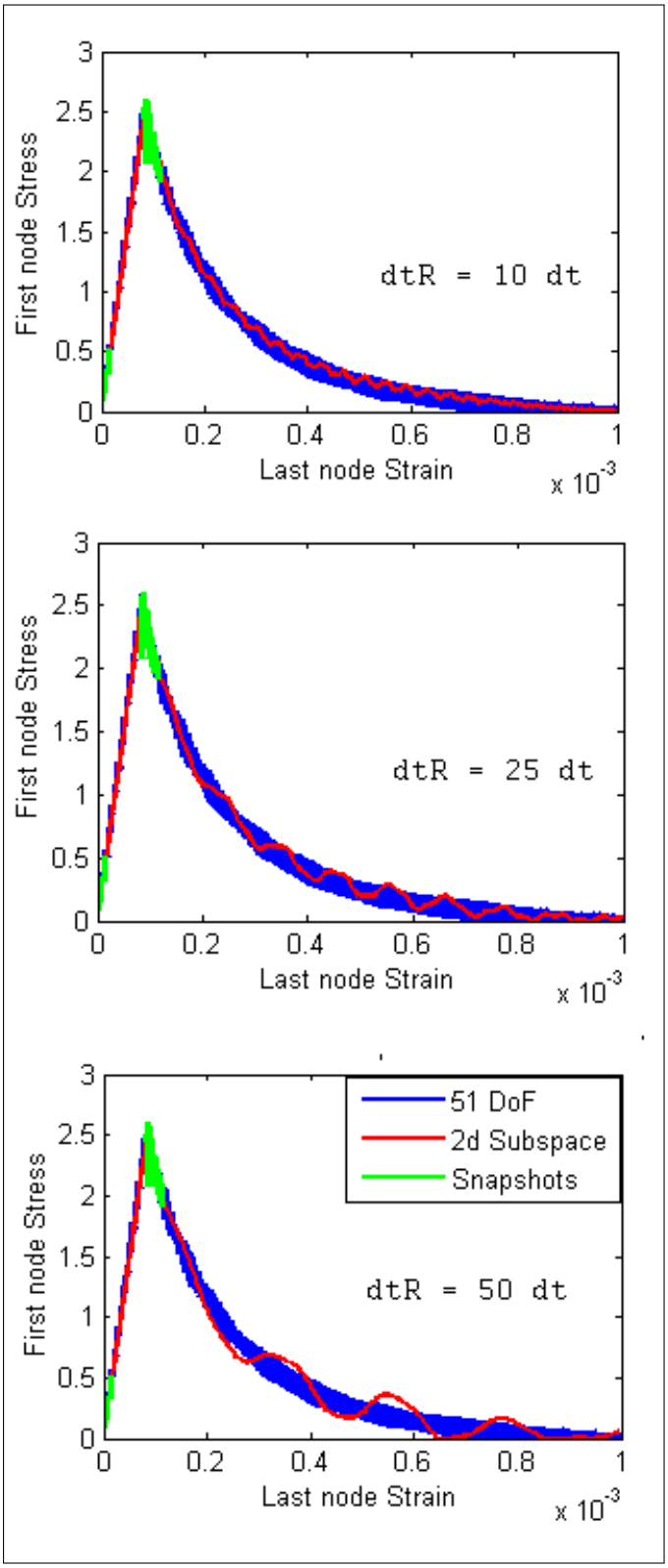

Figure 4.17: First Node Stress-Last Node Strain for 50 elements, softening material

4.3 2D Application: Cantilever Beam

In order to be able to apply the Proper Orthogonal Decomposition to the solution of any dynamic discrete system, the method validated for 1D trusses has then been tested for a 2-dimensional cantilever beam with a superimposed vertical displacement to the last node. Each node has 3 degrees of freedom, including a rotational one. The application of the POD technique does not change: the snapshots are collected during the initial fully explicit integration for each degree of freedom, including the rotational one. Then, they are used for the computation of the appropriate subspace where the reduced integration will takes place. (problema rotazioni)
A cantilever beam as shown in figure 4.18 has been simulated. The lenght of the

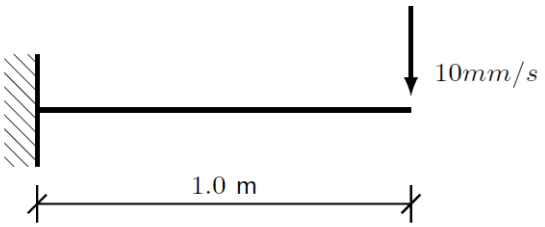

Figure 4.18: Cantilever beam tested

beam is set to $l = 1$ m, the radius of the cross section $R = 10$ cm and a velocity of $v = 10$ mm/s has been applied to the last node, in vertical direction. One case study with 10 elements and another one with 50 elements have been performed.

4.3.1 Results

The POD technique allows to achieve accurate and efficient results for both the linear elastic material and the plastic material. The trend observed for the 1D case study is reproduced for the 2D case. In particular, only the first POD mode is sufficient to approximate the linear elastic behavior, while also the second one is necessary to approximate the plastic behavior after yielding.

The stable time step in the reduced system increases with the number of elements: the 10 elements beam allows a time step $dt_R = 10 \cdot dt$ while the 50 elements beam allows a time step of $dt_R = 400 \cdot dt$

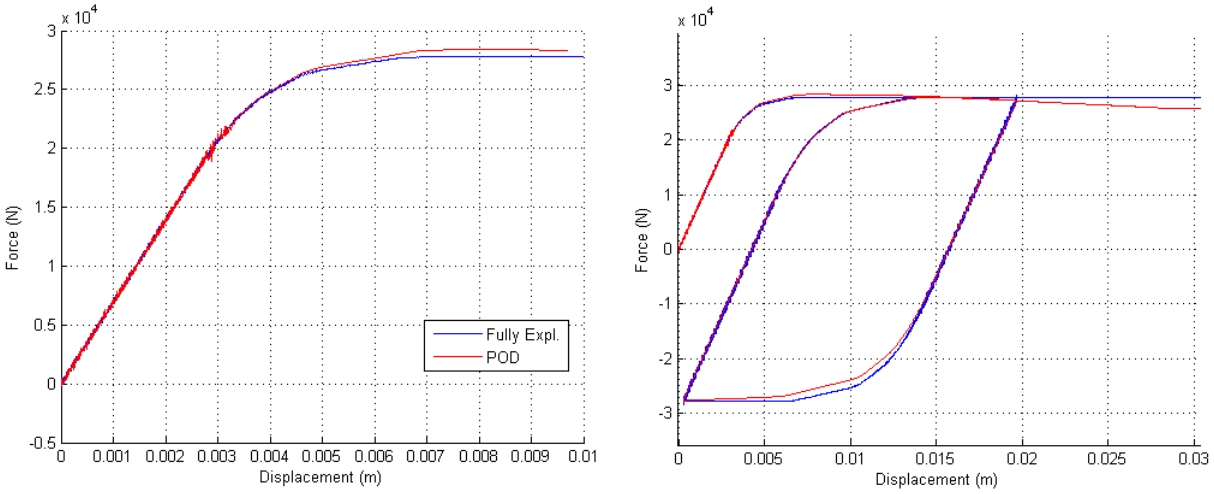

Figure 4.19: Force-Displacement curves (10 elements)

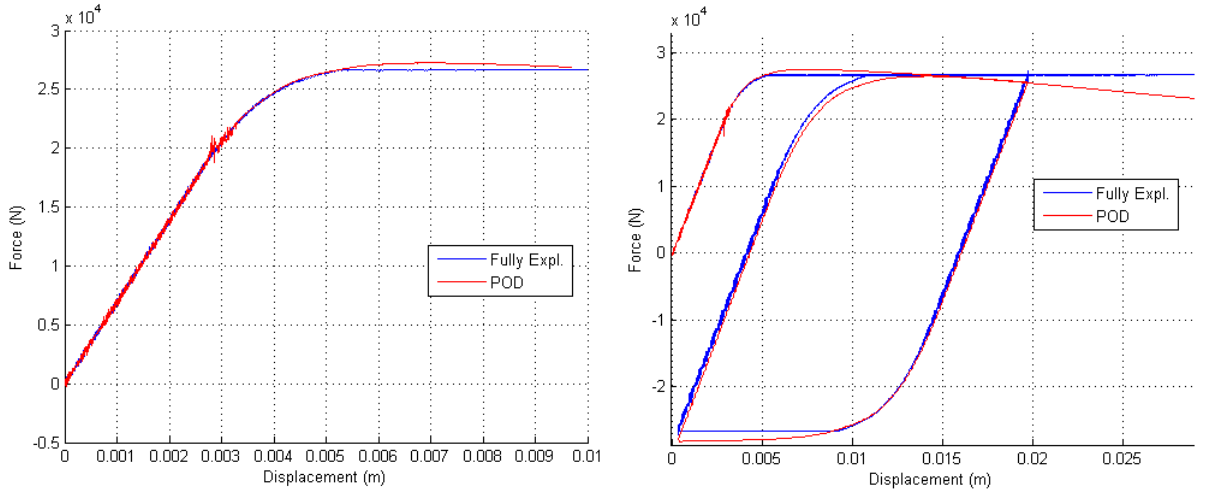

Figure 4.20: Force-Displacement curves (50 elements)

4.4 3D Application in LDPM: the Dog-Bone Test

Finally, the Proper Orthogonal Decomposition Technique is tested for simple 3D concrete specimens modeled with LDPM, where every node has 6 degrees of freedom, in order to investigate the method's applicability and understand its limitations in more complex numerical simulations.
First, a direct tension test has been performed on a dog-bone shaped specimen, as shown in figure 4.21, with dimensions H=30 cm, B=30 cm, D=20 cm. A constant velocity of 10 mm/s is applied uniformly to the nodes belonging to the top surface, while the bottom surface is fixed. With the only purpose of comparing the results obtained from the fully explicit analysis with the ones from the POD analysis, a coarse (2148 nodes) and a fine mesh (17441 nodes) have been considered and compared.

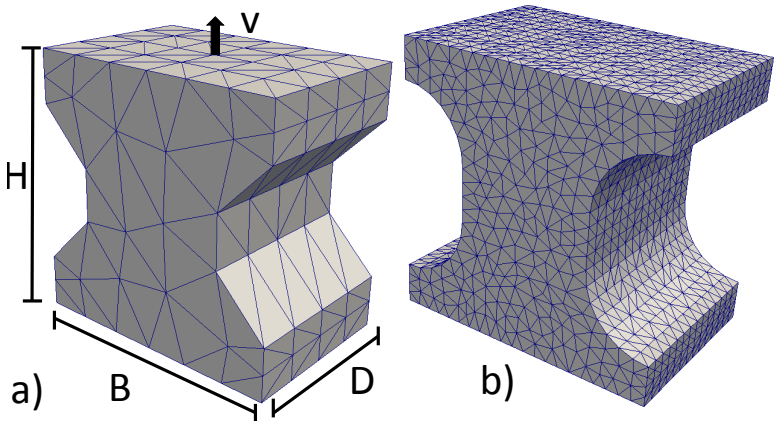

Figure 4.21: Geometry and set up for the Dogbone Test: a)coarse mesh; b) fine mesh

The force-displacement response of the coarse-meshed specimen is plotted in figure 4.22, where a comparison between the fully explicit method and the POD method is been shown. In particular, for the POD application, the basis for the reduced system have been updated 3 times (3 ms, 6 ms, 9 ms) to take account of the progressive fracturing. In terms of efficiency, the stable time step in the reduced system is $dt_R = 6 \cdot dt$, leading to a global index of performance $PIF = 3.4$.
The force-displacement response of the fine-meshed specimen is shown in figure 4.23. In this case, the POD application allows a performance 5 times faster than the one achieved with the fully explicit analysis ($PIF = 5.0$). In this case, the stable time step in the reduced system is $dt_R = 15 \cdot dt$ and the basis is updated twice (3 ms and 5 ms).
In both the examples, just 2 modes are enough to capture a good approximation of the response.

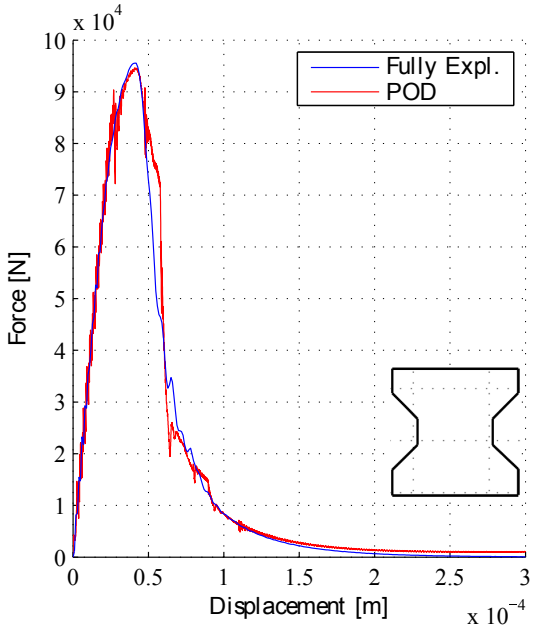

Figure 4.22: Force-Displacement responses from the Dogbone test (coarse mesh)

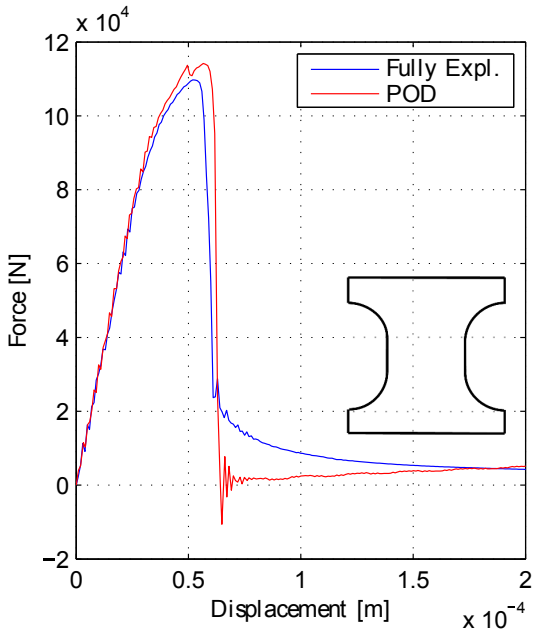

Figure 4.23: Force-Displacement responses from the Dogbone Test (fine mesh)

4.5 3D Application in LDPM: Compression test

To pursue the final aim of this research, the POD has been tested also for columns subjected to compressive loadings. Initially a plain concrete column has been studied and then the problem of the FRP confined concrete column has been addressed.

4.5.1 Plain Concrete Column

The algorithm has been initially tested for a cylindrical concrete column with the same dimensions of the specimens considered for the study of FRP confinement ($H = 300$ mm, $D = 150$ mm) as shown in figure 4.24. Also the same parameters for LDPM have been taken. In order to increase the speed of this phase, a coarse mesh have been considered (1635 nodes), with the only purpose of checking the potential efficiency of the algorithm, especially in relation to the softening response. Again,

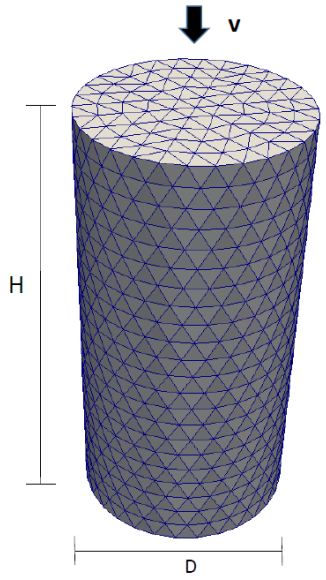

Figure 4.24: Geometry of the plain concrete column

the force-displacements curves are plotted comparing the response of the fully explicit algorithm with the response of the reduced system. It has been noticed that, during the softening in compression, frequent updates of the modes are required in order to capture the decreasing branch. The current explanation for this behavior is related to progressive and diffused fracturing process of the material, which makes the POD modes almost immediately no longer representative of the ongoing response. An automatic update of the modes has been set during the softening, which are updated every regular intervals of time, and different moments for the

updates have been compared (Figure 4.25). As previously, only 2 modes are used he stable time step in the reduced system is $dt_R = 20$ ms with a global index of performance $PIF = 2.5$.

Figure 4.26 shows the same simulation which has run for a longer time: after the

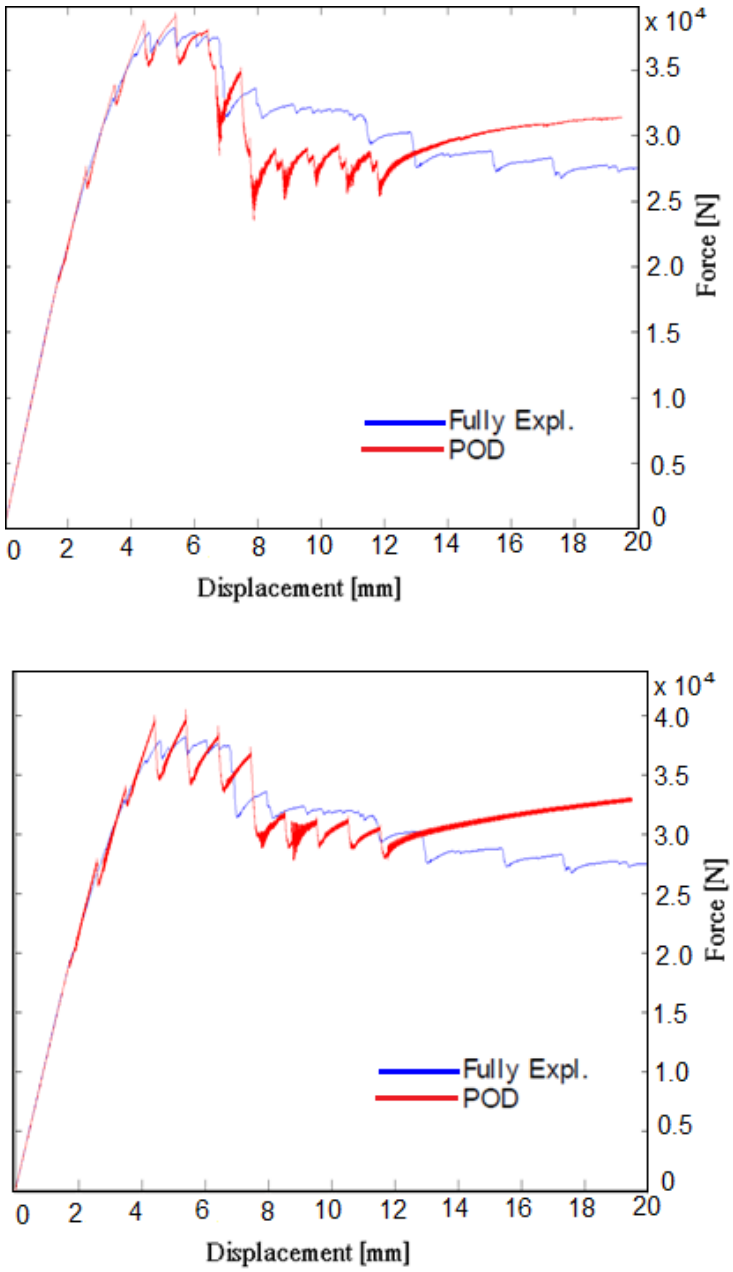

Figure 4.25: Force-Displacement responses from the Compression Test of plain concrete column (different update combinations)

material collapse, the simulation in the reduced space can approximate the fully explicit response without need of further updates.
It should be noted that the column has a coarse mesh so the output curves might not be representative of the real behavior, but the purpose of the simulations has been only numerical, related to the comparison between the fully explicit and the reduced algorithm.

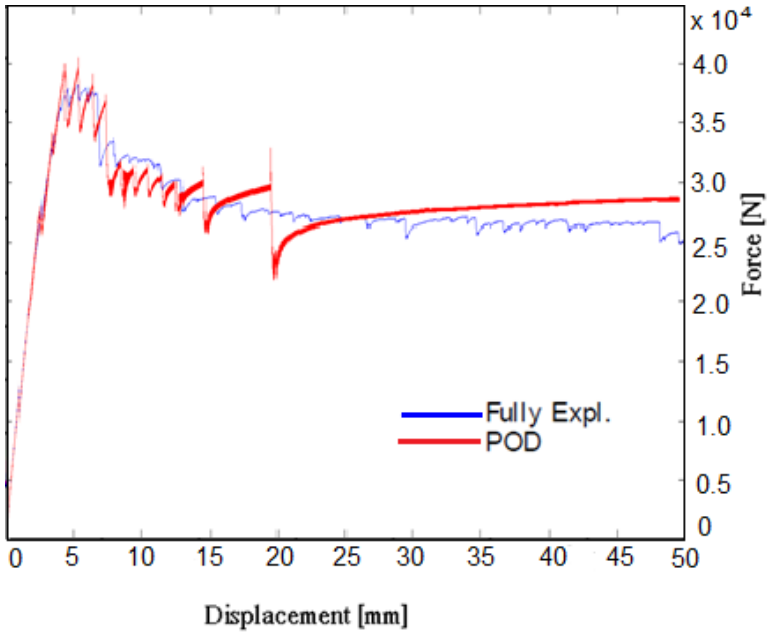

Figure 4.26: Force-Displacement responses from the Compression Test of plain concrete column (longer simulation)

4.5.2 FRP Confined Concrete Column

Finally, the POD algorithm has been applied to the case of the cylindrical column wrapped by FRP jacket. The geometrical and material parameters are the ones used for simulations described in Chapter 3. The original mesh is shown in figure 4.27 (9470 nodes). In order to apply the POD more easily, the contact between FRP

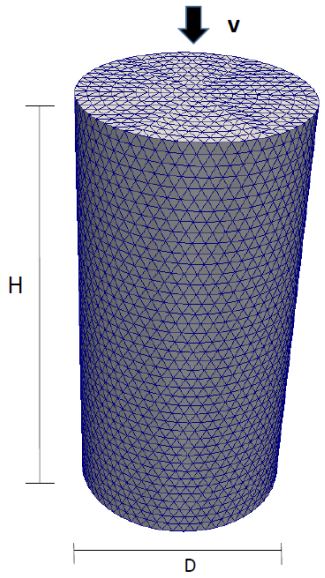

Figure 4.27: Geometry of the plain concrete column

and the external concrete surface is not longer given by a master-slave formulation, but simply the surfaces are sharing the same nodes. Also, in these simulations, the FRP material has been considered elastic.
In figure 4.28, the curve from the Fully Explicit algorithm and the one from the POD are compared. Also in this case, in the post-peak phase more frequent updates are required, as explained in the case of the plain concrete column. In this specific case, the time step in the reduced algorithm is $dt_R = 60 \cdot dt$ but the index of performance is limited to $PIF = 3$. In fact the advantage in terms of time step is partially lost because of the frequent update.
The algorithm has still room for improvement and the objective would be to achieve a global gain of 10 times so that LDPM can be used also for practical applications. Anyway, the algorithm as it is can still be considered useful in the calibration process, to check the trend of the response in a shorter time.

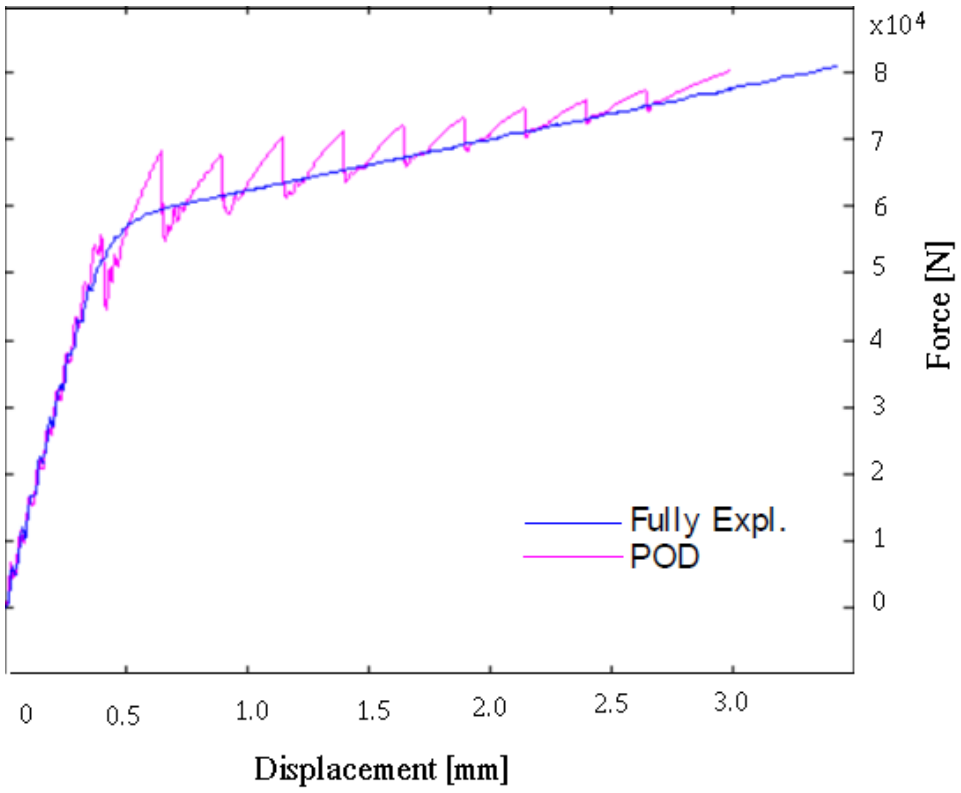

Figure 4.28: Force-Displacement responses from the Compression Test of FRP confined column.

A: Why the Penalty Method

The Penalty Method has proven to be the most effective way to apply the BCs in the reduced system.

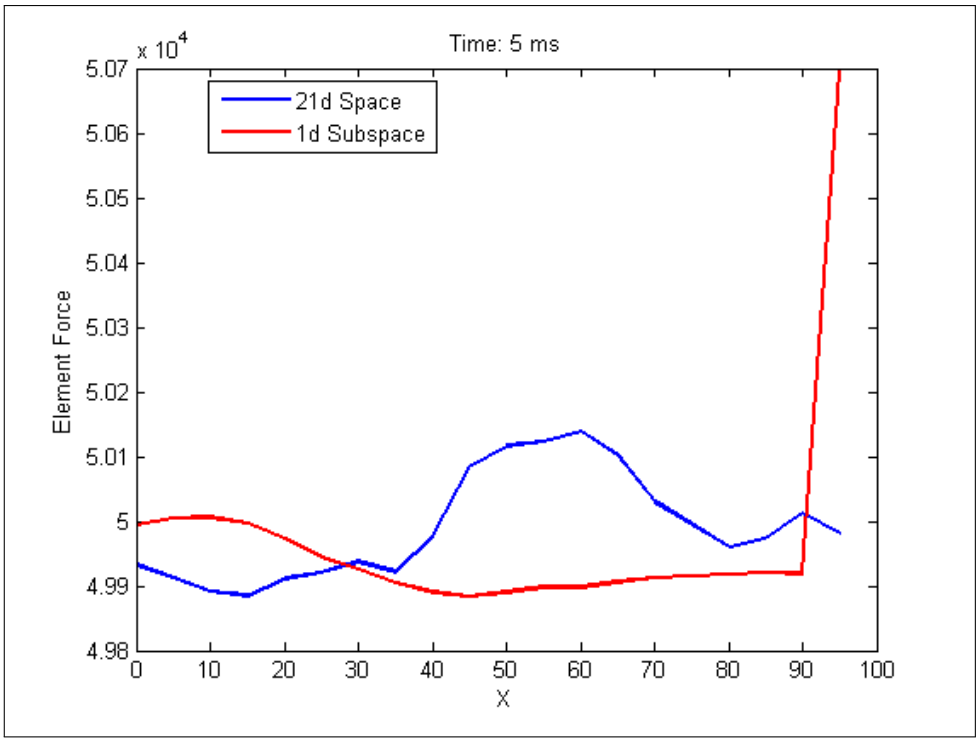

Figure 4.29: Last Element instability

Another method has been explored, based on the integration of the reduced system without taking account of the BCs, superimposing then the velocities and the displacements in the complete system just before the forces calculations. When the residual forces are evaluated, the nodes where the boundary conditions have been superimposed must be rewritten in order to satisfy the equation of motion. The algorithm for the 1D case study with the imposed velocity to the last node is

written as following:

$$\mathbf{f_{int}}^m = \mathbf{f_{int}}\left(\mathbf{u}^m\right) \tag{4.23a}$$

$$\mathbf{r}^m = \mathbf{f_{ext}}^m - \mathbf{f_{int}}^m; \qquad r_n^m = M_{nn}\left(\dot{u_n}^{m+1/2} - \dot{u_n}^{m-1/2}\right)/\Delta t_r \tag{4.23b}$$

$$\ddot{\mathbf{d}}^m = \left(\mathbf{B}^T\mathbf{M}\mathbf{B}\right)^{-1}\mathbf{r}_m \tag{4.23c}$$

$$\dot{\mathbf{d}}^{m+1/2} = \dot{\mathbf{d}}^{m-1/2} + \ddot{\mathbf{d}}^m \Delta t_r \tag{4.23d}$$

$$\mathbf{d}^{m+1} = \mathbf{d}^m + \dot{\mathbf{d}}^{m+1/2}\Delta t_r \tag{4.23e}$$

$$\mathbf{u}^{m+1} = \mathbf{B}\mathbf{d}^{m+1}; \qquad \left(u_n{}^{m+1} = f\left(\dot{u_n}\right)\right) \tag{4.23f}$$

$$\tag{4.23g}$$

The described method, even if leading to good results, is characterized by an effective stable time step smaller than the calculated one and this behavior, due to an increased instability of the last element where the BC is superimposed. Figure 4.29 shows that the algorithm for the reduced system causes an increased internal force in the last element, leading to a premature instability.

Chapter 5

Conclusions and Future Research Goals

5.1 Summary of the present research

5.1.1 Modeling of FRP confined concrete

A three-dimensional meso-scale model based on the Lattice Discrete Particle Model (LDPM) has been developed for the simulation of FRP-confined concrete columns subjected to compressive loading and different shapes of cross sections have been considered. Being the meso-scale approach based on the interaction amongst concrete aggregates and particles, it can provide a global solution for the constitutive relationship of concrete and, consequently, overcome many of the limitations of continuum mechanics dealing with the complex response of FRP confined concrete.
LDPM, in particular, has proved to be very effective in predicting the stress-strain behavior and the failure modes of concrete under compression. This is because of its unique capability of simulating compressive failure not postulating the existence of softening in compression, as typical continuum-based models do, but through tensile and shearing softening at the meso-scale, consistently with the experimental evidence [25].
Experimental data have been gathered from literature, regarding FRP confined columns with different shapes loaded in compression, in order to verify the capability of LDPM to deal with the FRP confinement problems.
Firstly, an improvement in the LDPM constitutive laws in compression became necessary, in order to correctly describe the behavior of concrete under low confinement. In fact, before the present research, LDPM had been validated only for high confinement stress (50-200 MPa) , while concrete is subjected to pressure up to 10-20 MPa when the confinement is provided by the composite wrapping; the related equations have been consequently rewritten in order to make them suitable for the most gen-

eral case .
After that, LDPM parameters have been calibrated for the specific case study: a first set of parameters is required for the creation of the internal geometry and the values come directly from the concrete mix-design data, a second set is necessary for the constitutive equations and those values are calibrated by fitting the experimental curves available for plain concrete.
The FRP sheets have been modeled using quadrilateral shell elements and the Spectral Stiffness Micropane Model as constitutive law, in order to simulate the orthotropic behavior of the composites and their brittle failure; in addiction, a stochastic model has been assigned for its strength, to take into account the scatters in the coupon tests in terms of ultimate strength. The contact between FRP and concrete has been defined through a master-slave formulation where both the normal and the tangential forces are transmitted at the interface level (full contact).
The results achieved by means of the present model are very satisfactory for columns with larger corner radius: by calibrating LDPM parameters for the plain concrete response, the typical bilinear stress-strain loading curves of FRP confined concrete are captured when the wrapping is added. The match with the experimental curves is good for different level of confinement (1 or 2 layers) and for different cross section shapes (from $r = 30$ mm to $r = 75$ mm). The model, in fact, has not problems in dealing with non uniform confinement.
In addiction, the ultimate condition of those specimens is also well predicted; the ultimate stress and strain are captured with very good approximation and this is not common amongst the models available in literature. In addition, also the failure mechanisms of the columns can be realistically reproduced: the FRP, and therefore the whole column, usually starts failing where the rounded corner joints the flat side, as it happens in the numerical simulations.
On the other hand, the present model is not suitable for describing the response of specimens with a corner radius equal or close to zero ($r = 0$ or $r = 15$ mm) . Columns with right angled shapes, in fact, require a more sophisticated modeling of the FRP jacket and, in particular, of the contact between FRP and concrete in order to capture the complex phenomena related to the local stress concentrations and delamination processes; in fact, with a full-contact master slave formulation, the debonding process of the FRP cannot be simulated. If the tangential interaction between the surfaces in contact is neglected (normal contact), the confinement effect decreases significantly for these type of columns: in particular, in the case of the square shaped specimen wrapped by 1 FRP ply, the experimental response is almost captured. On the contrary, if the specimen is cylindrical, the stress vs strain response is not affected by the type of contact, so one can assume that the importance of modeling the debonding effect is likely to increase with the decreasing of the corner radius up to becoming fundamental for square columns. In addition, another limitation of the current numerical approach is related to the incapability

of modeling directly the flexural behavior in the FRP, because an equivalent thickness has been used. The flexural behavior, though, becomes more important in case of small corner radius, increasing the triaxial stress state in the material and the stochastic approach for the FRP strengths might be not enough to take into account all these variegated characteristics.

5.1.2 Computational aspects

This research has been also developed along another, parallel path: to cope with the high computational costs of the numerical simulations of LDPM problems, the Proper Orthogonal decomposition (POD) has been explored as a model reduction technique, in order to speed up the analysis.
The software MARS, where the LDPM computational framework is implemented, performs structural analysis by an explicit dynamic algorithm based on a central difference scheme, which on one hand is convenient in terms of convergence, especially if dealing with softening behaviors, but on the other hand, being the algorithm stable under conditions, the time step required might be excessively small, in particular if low-dynamics is concerned. In this context, the POD method has been considered an attractive possibility: it seeks only the dominant components of the response by projecting dynamic systems onto subspaces containing the solution or at least good approximation of it, so that a low-order problem can be solved instead of the original one. The subspaces are generated by the so called Proper Orthogonal Modes, which can be computed from the full-order system solution.
The Full-Order Integration Algorithm for the motion governing equation, based on the middle-point rule, is projected according to the POD theory and a corresponding Reduced-Order algorithm is defined, with a smaller number of unknowns and a higher stable time step. In particular, the dimension of the subspace depends on the number of modes used for the projection and the accuracy of the solution in the subspace depends on the capability of those modes to represent the dominant components of the global solution. Moreover, if the trend of the global solution changes during the simulation, the modes have to be updated so that a different subspace can be defined.
A new algorithm based on the POD method has been tested for 1D truss elements and 2D beam elements, finding out that the efficiency of the method, based mainly on the gain in terms of stable time step, increases with the number of degrees of freedom of the original problem. Also, just a very limited number of modes are enough to achieve high levels of accuracy of the solution. If yielding or fracture occurs at the material level, the subspace must be redefined, since the old one cannot contain the new solution.
The application of POD to 3D case studies has been successful for direct traction tests: the modes do not need frequent updates during the softening phase because

the fracture in the specimens is localized, so the modes change suddenly and quickly. This is no longer true for the compression tests, where the fracturing process is progressive and diffuse and, consequently, updating the modes is required more often because the modes change gradually. Of course, the more the modes need to be updated, the less convenient the POD method becomes. Finally, the method has been applied to the case study of interest in the present research - the FRP confined concrete columns. In particular, the response of the circular column has been evaluated. The proper orthogonal modes need to be updated frequently during the post-peak phase and for this reason, even if the gain in terms of time step is pretty high, up to 60 times higher than the original one, the global gain in terms of cpu time is limited to 3 times. However, the approximated solution can still be considered a good approximation of the correct one and might be used in the calibration process.

5.2 Steps Further...

As far as the future research related to the modeling of FRP confinement is concerned, one of the main issues is related to the square columns response. As it has been highlighted, the development of a more realistic contact algorithm will be the next step in order to simulate the debonding and the detaching of the FRP jacket from the concrete column surface; in fact the preliminary analysis reported in the discussion of the related results, in Chapter 3, showed the importance of the correct simulation of the interface between the two materials for the sharp corner shaped sections, so a deeper study of this aspect will be the next goal.
Furthermore, another future development is related to the study of the behavior of FRP-confined reinforced concrete columns. The model so far has proved to be predictive for FRP confined plain concrete columns. It will be interesting to study the numerical response of reinforced concrete columns, when internal steel rebars and stirrups are included and interacting with the external jacket: the mutual confining action of the composite wrapping and steel stirrups originates complex stress states along the section and the height of the columns. Moreover, the longitudinal bars may suffer from buckling phenomena leading to peak stress in the FRP at rebar positions, causing premature failure. The understanding of these aspects can lead to the development of a practical numerical tool able to face applicative engineering problems.
Regarding the computational aspects of the present study, the improving of the POD application for LDPM in case of softening behaviors will be the next step, in order to be able to achieve a global cpu time gain of 10 times. Also, it would be interesting to develop an adaptive algorithm, able to predict when automatically update the modes.

Bibliography

[1] J. Chen, S. Li, L. Bisby, Factors affecting the ultimate condition of frp-wrapped concrete columns, Journal of Composites for Construction 17 (1) (2013) 67–78. doi:10.1061/(ASCE)CC.1943-5614.0000314.

[2] J. Teng, L. Lam, Behavior and modeling of fiber reinforced polymer-confined concrete, Journal of structural engineering 130 (11) (2004) 1713–1723. doi:http://dx.doi.org/10.1061/(ASCE)0733-9445(2004)130:11(1713).

[3] Theoretical stressstrain model for confined concrete, Journal of Structural Engineering 114 (8) (1988) 1804–1826. doi:10.1061/(ASCE)0733-9445(1988)114:8(1804).

[4] L. Lam, J. Teng, Design-oriented stressstrain model for frp-confined concrete, Construction and Building Materials 17 (67) (2003) 471 – 489, fibre-reinforced polymer composites in construction. doi:http://dx.doi.org/10.1016/S0950-0618(03)00045-X.

[5] T. C. Rousakis, T. D. Rakitzis, A. I. Karabinis, Design-oriented strength model for frp-confined concrete members, Journal of Composites for Construction 16 (6) (2012) 615–625. doi:http://dx.doi.org/10.1061/(ASCE)CC.1943-5614.0000295.

[6] T. Ozbakkaloglu, J. C. Lim, Axial compressive behavior of frp-confined concrete: Experimental test database and a new design-oriented model, Composites Part B: Engineering 55 (2013) 607 – 634. doi:http://dx.doi.org/10.1016/j.compositesb.2013.07.025.

[7] T. Jiang, J. Teng, Analysis-oriented stressstrain models for frpconfined concrete, Engineering Structures 29 (11) (2007) 2968 – 2986. doi:http://dx.doi.org/10.1016/j.engstruct.2007.01.010.

[8] B. Binici, An analytical model for stressstrain behavior of confined concrete, Engineering Structures 27 (7) (2005) 1040 – 1051. doi:http://dx.doi.org/10.1016/j.engstruct.2005.03.002.

[9] J. Teng, Y. Huang, L. Lam, L. Ye, Theoretical model for fiber-reinforced polymer-confined concrete, Journal of composites for construction 11 (2) (2007) 201–210. doi:10.1061/(ASCE)1090-0268(2007)11:2(201).

[10] C. Pellegrino, C. Modena, Analytical model for frp confinement of concrete columns with and without internal steel reinforcement, Journal of Composites for Construction 14 (6) (2010) 693–705. doi:http://dx.doi.org/10.1061/(ASCE)CC.1943-5614.0000127.

[11] M. H. Harajli, Axial stressstrain relationship for {FRP} confined circular and rectangular concrete columns, Cement and Concrete Composites 28 (10) (2006) 938 – 948, durability and Ductility of {FRP} Strengthened Beams, Slabs and Columns. doi:http://dx.doi.org/10.1016/j.cemconcomp.2006.07.005.

[12] M. Maalej, S. Tanwongsval, P. Paramasivam, Modelling of rectangular {RC} columns strengthened with {FRP}, Cement and Concrete Composites 25 (2) (2003) 263 – 276. doi:http://dx.doi.org/10.1016/S0958-9465(02)00017-3.

[13] T. Yu, J. Teng, Y. Wong, S. Dong, Finite element modeling of confined concrete-i: Drucker-prager type plasticity model, Engineering Structures 32 (3) (2010) 665–679. doi:10.1016/j.engstruct.2009.11.014.

[14] T. Rousakis, A. Karabinis, P. Kiousis, Frp-confined concrete members: Axial compression experiments and plasticity modelling, Engineering Structures 29 (7) (2007) 1343–1353. doi:10.1016/j.engstruct.2006.08.006.

[15] A. Karabinis, T. Rousakis, Concrete confined by frp material: A plasticity approach, Engineering Structures 24 (7) (2002) 923–932. doi:10.1016/S0141-0296(02)00011-1.

[16] A. Fam, S. Rizkalla, Confinement model for axially loaded concrete confined by circular fiber-reinforced polymer tubes, ACI Structural Journal 98 (4) (2001) 451–461.

[17] A. Mirmiran, K. Zagers, W. Yuan, Nonlinear finite element modeling of concrete confined by fiber composites, Finite elements in analysis and design 35 (1) (2000) 79–96. doi:10.1016/S0168-874X(99)00056-6.

[18] T. Yu, J. Teng, Y. Wong, S. Dong, Finite element modeling of confined concrete-ii: Plastic-damage model, Engineering Structures 32 (3) (2010) 680–691. doi:10.1016/j.engstruct.2009.11.013.

[19] S. Gambarelli, N. Nistic, J. Obolt, Numerical analysis of compressed concrete columns confined with cfrp: Microplane-based approach, Composites Part

B: Engineering 67 (2014) 303 – 312. doi:http://dx.doi.org/10.1016/j.compositesb.2014.06.026.

[20] C. Desprez, J. Mazars, P. Kotronis, P. Paultre, Damage model for frp-confined concrete columns under cyclic loading, Engineering Structures 48 (2013) 519 – 531. doi:http://dx.doi.org/10.1016/j.engstruct.2012.09.019.

[21] J. Teng, L. Lam, G. Lin, J. Lu, Q. Xiao, Numerical simulation of frp-jacketed rc columns subjected to cyclic and seismic loading, Journal of Composites for Construction (2015) 04015021doi:http://dx.doi.org/10.1061/(ASCE)CC.1943-5614.0000584.

[22] Three-dimensional finite element analysis of reinforced concrete columns with {FRP} and/or steel confinement, Engineering Structures 97 (2015) 15 – 28. doi:http://dx.doi.org/10.1016/j.engstruct.2015.03.030.

[23] J. F. C. J.G. Teng, J. J. Zeng, Measurement of axial stress distributions in frp-confined concrete columns using tekscan pressure sensors, Vol. 1, 2015, pp. 8–10.

[24] Y.-F. Wu, Development of constitutive models for {FRP} confined concrete structures, Vol. 1, 2015, p. 90.

[25] G. Cusatis, D. Pelessone, A. Mencarelli, Lattice discrete particle model (LDPM) for failure behavior of concrete. I: Theory, Cement and Concrete Composites 33 (9) (2011) 881 – 890. doi:http://dx.doi.org/10.1016/j.cemconcomp.2011.02.011.

[26] G. Cusatis, A. Mencarelli, D. Pelessone, J. T. Baylot, Lattice discrete particle model (LDPM) for failure behavior of concrete. II: Calibration and validation, Cement and Concrete Composite 33 (9) (2011) 891 – 905. doi:http://dx.doi.org/10.1016/j.cemconcomp.2011.02.010.

[27] E. A. Schauffert, G. Cusatis, Lattice discrete particle model for fiber-reinforced concrete. i: Theory, Journal of Engineering Mechanics 138 (7) (2011) 826–833. doi:http://dx.doi.org/10.1061/(ASCE)EM.1943-7889.0000387.

[28] E. A. Schauffert, G. Cusatis, D. Pelessone, J. L. ODaniel, J. T. Baylot, Lattice discrete particle model for fiber-reinforced concrete. ii: Tensile fracture and multiaxial loading behavior, Journal of Engineering Mechanics 138 (7) (2012) 834–841. doi:http://dx.doi.org/10.1061/(ASCE)EM.1943-7889.0000392.

[29] M. Alnaggar, G. Cusatis, G. Di Luzio, Lattice discrete particle modeling (ldpm) of alkali silica reaction (asr) deterioration of concrete structures, Cement and

Concrete Composites 41 (2013) 45–59. doi:http://dx.doi.org/10.1016/j.cemconcomp.2013.04.015.

[30] R. El-Helou, C. Moen, E. Lale, G. Cusatis, Lattice discrete particle modeling of buckling deformation in thin ultra-high-performance fiber-reinforced concrete plates, Vol. 1, 2014, pp. 365–371.

[31] D. Pelessone, MARS, modeling and analysis of the response of structures. User's manual, ES3 Inc., 2015.

[32] G. J. de Frias, W. Aquino, K. H. Pierson, M. W. Heinstein, B. W. Spencer, A multiscale mass scaling approach for explicit time integration using proper orthogonal decomposition, International Journal for Numerical Methods in Engineering 97 (11) (2014) 799–818. doi:http://dx.doi.org/0.1002/nme.4608.

[33] G. Cocchetti, M. Pagani, U. Perego, Selective mass scaling and critical time-step estimate for explicit dynamics analyses with solid-shell elements, Computers and Structures 127 (0) (2013) 39 – 52. doi:http://dx.doi.org/10.1016/j.compstruc.2012.10.021.

[34] L. Gao, V. M. Calo, Fast isogeometric solvers for explicit dynamics, Computer Methods in Applied Mechanics and Engineering 274 (0) (2014) 19 – 41. doi:http://dx.doi.org/10.1016/j.cma.2014.01.023.

[35] S.-Y. Chang, A new family of explicit methods for linear structural dynamics, Computers and Structures 88 (1112) (2010) 755 – 772. doi:http://dx.doi.org/10.1016/j.compstruc.2010.03.002.

[36] M. Xiao, P. Breitkopf, R. F. Coelho, P. Villon, W. Zhang, Proper orthogonal decomposition with high number of linear constraints for aerodynamical shape optimization, Applied Mathematics and Computation 247 (0) (2014) 1096 – 1112. doi:http://dx.doi.org/10.1016/j.amc.2014.09.068.

[37] F. Behzad, B. T. Helenbrook, G. Ahmadi, On the sensitivity and accuracy of proper-orthogonal-decomposition-based reduced order models for burgers equation, Computers and Fluids 106 (0) (2015) 19 – 32. doi:http://dx.doi.org/10.1016/j.compfluid.2014.09.041.

[38] H. Chen, M. Xu, D. L. Hung, H. Zhuang, Cycle-to-cycle variation analysis of early flame propagation in engine cylinder using proper orthogonal decomposition, Experimental Thermal and Fluid Science 58 (0) (2014) 48 – 55. doi:http://dx.doi.org/10.1016/j.expthermflusci.2014.06.017.

[39] X. Li, X. Chen, B. X. Hu, I. M. Navon, Model reduction of a coupled numerical model using proper orthogonal decomposition, Journal of Hydrology 507 (0)

(2013) 227 – 240. doi:http://dx.doi.org/10.1016/j.jhydrol.2013.09.011.

[40] R. Mariani, D. Dessi, Analysis of the global bending modes of a floating structure using the proper orthogonal decomposition, Journal of Fluids and Structures 28 (0) (2012) 115 – 134. doi:http://dx.doi.org/10.1016/j.jfluidstructs.2011.11.009.

[41] P. Kerfriden, O. Goury, T. Rabczuk, S. Bordas, A partitioned model order reduction approach to rationalise computational expenses in nonlinear fracture mechanics, Computer Methods in Applied Mechanics and Engineering 256 (0) (2013) 169 – 188. doi:http://dx.doi.org/10.1016/j.cma.2012.12.004.

[42] L.-M. Wang, Y.-F. Wu, Effect of corner radius on the performance of cfrp-confined square concrete columns: Test, Engineering Structures 30 (2) (2008) 493 – 505. doi:http://dx.doi.org/10.1016/j.engstruct.2007.04.016.

[43] Z. P. Bažant, B. H. Oh, Microplane model for progressive fracture of concrete and rock, Journal of Engineering Mechanics 111 (4) (1985) 559– 582. doi:http://dx.doi.org/10.1061/(ASCE)0733-9399(1985)111:4(559).

[44] F. C. Caner, Z. P. Bažant, Microplane model m7 for plain concrete. i: Formulation, Journal of Engineering Mechanics 139 (12) (2012) 1714– 1723. doi:http://dx.doi.org/10.1061/(ASCE)EM.1943-7889.0000570.

[45] G. Cusatis, A. Beghini, Z. P. Baant, Spectral stiffness microplane model for quasi-brittle composite laminates: I. theory., Journal of Applied Mechanics 75 (2) (2005) 021009. doi:http://dx.doi.org/10.1115/1.2744036.

[46] Z. P. Bažant, P. C. Prat, Microplane model for brittle plastic material: I. theory, Journal of Engineering Mechanics 114 (10) (1988) 1672– 1688. doi:http://dx.doi.org/10.1061/(ASCE)0733-9399(1988)114:10(1672).

[47] I. Carol, Z. P. Bažant, Damage and plasticity in microplane theory, International Journal of Solids and Structures 34 (29) (1997) 3807 – 3835. doi:http://dx.doi.org/10.1016/S0020-7683(96)00238-7.

[48] G. Cusatis, A. Beghini, Z. Bažant, Spectral stiffness microplane model for quasibrittle composite laminates-part i: Theory, Journal of Applied Mechanics 75 (2) (2008) 021009. doi:http://dx.doi.org/10.1115/1.2744036.

[49] J. Rychlewski, Unconventional approach to linear elasticity, Archives of Mechanics 47 (1995) 149–171.

[50] P. S. Theocaris, D. P. Sokolis, Spectral decomposition of the compliance tensor for anisotropic plates, Journal of elasticity 51 (2) (1998) 89–103.

[51] P. S. Theocaris, D. P. Sokolis, Spectral decomposition of the linear elastic tensor for monoclinic symmetry, Acta Crystallographica Section A 55 (4) (1999) 635–647. doi:10.1107/S0108767398016766.

[52] P. S. Theocaris, D. P. Sokolis, Spectral decomposition of the compliance fourth-rank tensor for orthotropic materials, Archive of Applied Mechanics 70 (4) (2000) 289–306. doi:http://dx.doi.org/10.1007/s004199900066.

[53] G. Cusatis, Z. Bažant, L. Cedolin, Confinement-shear lattice model for concrete damage in tension and compression: I. theory, Journal of Engineering Mechanics 129 (12) (2003) 881–889.

[54] J. G. Teng, J. F. Chen, S. T. Smith, L. Lam, FRP: Strengthened RC Structures, Addison-Wesley, 2001.

[55] L. Lam, J. Teng, Ultimate condition of fiber reinforced polymer-confined concrete, Journal of Composites for Construction 8 (6) (2004) 539–548. doi:10.1061/(ASCE)1090-0268(2004)8:6(539).

[56] S. T. Smith, S. J. Kim, H. Zhang, Behavior and effectiveness of frp wrap in the confinement of large concrete cylinders, Journal of Composites for Construction 14 (5) 573–582. doi:10.1061/(ASCE)CC.1943-5614.0000119.

[57] Y. Xiao, H. Wu, Compressive behavior of concrete confined by carbon fiber composite jackets, Journal of Materials in Civil Engineering 12 (2) (2000) 139–146. doi:10.1061/(ASCE)0899-1561(2000)12:2(139).

[58] S. Pessiki, K. A. Harries, J. T. Kestner, R. Sause, J. M. Ricles, Axial behavior of reinforced concrete columns confined with frp jackets, Journal of Composites for Construction 5 (4) (2001) 237–245. doi:10.1061/(ASCE)1090-0268(2001)5:4(237).

[59] M. Shahawy, A. Mirmiran, T. Beitelman, Tests and modeling of carbon-wrapped concrete columns, Composites Part B: Engineering 31 (67) (2000) 471 – 480. doi:http://dx.doi.org/10.1016/S1359-8368(00)00021-4.

[60] Z. P. Baant, S.-D. Pang, Activation energy based extreme value statistics and size effect in brittle and quasibrittle fracture, Journal of the Mechanics and Physics of Solids 55 (1) (2007) 91 – 131. doi:http://dx.doi.org/10.1016/j.jmps.2006.05.007.

[61] J.-L. Le, Z. Z. P. Bažant, M. Z. Bazant, Unified nano-mechanics based probabilistic theory of quasibrittle and brittle structures: I. strength, static crack growth, lifetime and scaling, Journal of the Mechanics and Physics of Solids

59 (7) (2011) 1291 – 1321. doi:http://dx.doi.org/10.1016/j.jmps.2011.03.002.

[62] M. Salviato, K. Kirane, Z. P. Bažant, Statistical distribution and size effect of residual strength of quasibrittle materials after a period of constant load, Journal of the Mechanics and Physics of Solids 64 (2014) 440 – 454. doi:http://dx.doi.org/10.1016/j.jmps.2013.12.005.

[63] M. Salviato, Z. P. Bažant, The asymptotic stochastic strength of bundles of elements exhibiting general stressstrain laws, Probabilistic Engineering Mechanics 36 (2014) 1 – 7. doi:http://dx.doi.org/10.1016/j.probengmech.2014.01.001.

[64] M. Vořechovskỳ, D. Novák, Correlation control in small-sample monte carlo type simulations i: A simulated annealing approach, Probabilistic Engineering Mechanics 24 (3) (2009) 452 – 462. doi:http://dx.doi.org/10.1016/j.probengmech.2009.01.004.

[65] O. Buyukozturk, O. Gunes, E. Karaca, Progress on understanding debonding problems in reinforced concrete and steel members strengthened using frp composites, Construction and Building Materials (18) (2004) 9–19. doi:doi:10.1016/S0950-0618(03)00094-1.

[66] R. Courant, K. Friedrichs, H. Lewy, On the partial difference equations of mathematical physics, IBM Journal 11 (0) (1976) 215234, translation of 1928 German original.

[67] T. Belytschko, W. K. Liu, B. Moran, Nonlinear finite elements for continua and structures, J. Wiley & sons, Chichester, New York, Weinheim, 2000.

[68] Y. Linang, H. Lee, S. Lim, W. Lin, K. Lee, C. Wu, Proper orthogonal decomposition and its applications - part i: Theory, Journal of Sound and Vibration 252 (3) (2002) 527 – 544. doi:http://dx.doi.org/10.1006/jsvi.2001.4041.

[69] A. Chatterjee, An introduction to the proper orthogonal decomposition, Current Science 78 (7) (2000) 808–817.

[70] A. C. Antoulas, Approximation of large-scale dynamical systems, Vol. 6, Siam, 2005.

[71] I. Kalashnikova, M. F. Barone, Efficient non-linear proper orthogonal decomposition/galerkin reduced order models with stable penalty enforcement of boundary conditions, International Journal for Numerical Methods in Engineering 90 (11) (2012) 1337–1362. doi:10.1002/nme.3366.